

Anomalous transport in the crowded world of biological cells

REVIEW ARTICLE

Felix Höfling¹ and Thomas Franosch²

¹ Max-Planck-Institut für Intelligente Systeme, Heisenbergstraße 3, 70569 Stuttgart, and Institut für Theoretische Physik IV, Universität Stuttgart, Pfaffenwaldring 57, 70569 Stuttgart, Germany

² Institut für Theoretische Physik, Friedrich-Alexander-Universität Erlangen–Nürnberg, Staudtstraße 7, 91058 Erlangen, Germany

Submitted to: *Rep. Prog. Phys.*; Received 25 June 2012; Revised 7 December 2012; Accepted 19 December 2012

Abstract

A ubiquitous observation in cell biology is that the diffusive motion of macromolecules and organelles is anomalous, and a description simply based on the conventional diffusion equation with diffusion constants measured in dilute solution fails. This is commonly attributed to macromolecular crowding in the interior of cells and in cellular membranes, summarising their densely packed and heterogeneous structures. The most familiar phenomenon is a sublinear, power-law increase of the mean-square displacement as function of the lag time, but there are other manifestations like strongly reduced and time-dependent diffusion coefficients, persistent correlations in time, non-gaussian distributions of spatial displacements, heterogeneous diffusion, and a fraction of immobile particles. After a general introduction to the statistical description of slow, anomalous transport, we summarise some widely used theoretical models: gaussian models like fractional Brownian motion and Langevin equations for visco-elastic media, the continuous-time random walk (CTRW) model, and the Lorentz model describing obstructed transport in a heterogeneous environment. Particular emphasis is put on the spatio-temporal properties of the transport in terms of two-point correlation functions, dynamic scaling behaviour, and how the models are distinguished by their propagators even if the mean-square displacements are identical. Then, we review the theory underlying commonly applied experimental techniques in the presence of anomalous transport like single-particle tracking, fluorescence correlation spectroscopy (FCS), and fluorescence recovery after photobleaching (FRAP). We report on the large body of recent experimental evidence for anomalous transport in crowded biological media: in cyto- and nucleoplasm as well as in cellular membranes, complemented by *in vitro* experiments where a variety of model systems mimic physiological crowding conditions. Finally, computer simulations are discussed which play an important role in testing the theoretical models and corroborating the experimental findings. The review is completed by a synthesis of the theoretical and experimental progress identifying open questions for future investigation.

PACS numbers: 05.40.-a 87.16.-b

Contents

1. Preface	2	4.2. Fluorescence correlation spectroscopy (FCS)	19
2. Basics of Brownian motion	3	4.3. Fluorescence recovery after photobleaching (FRAP)	22
2.1. Simple diffusion	4	5. Anomalous transport in crowded biological media	24
2.2. Anomalous and complex transport	5	5.1. Crowded cellular fluids	24
3. Theoretical models	8	5.2. Crowded membranes	33
3.1. Gaussian models	8	5.3. Reaction kinetics	42
3.2. Continuous-time random walks (CTRW)	10	6. Conclusion	43
3.3. Obstructed motion: Lorentz models	14	Acknowledgments	46
3.4. Other sources of subdiffusion	18	References	46
4. Experimental techniques	18		
4.1. Single-particle tracking	18		

1. Preface

Transport of mesoscopic particles suspended in simple solvents is governed by Brownian motion and is one of the pillars of biological and soft condensed matter physics. The pioneering works of Einstein and von Smoluchowski identified the random displacements as the essence of single-particle motion and—employing ideas of the central-limit theorem—suggest a gaussian probability distribution with a mean-square displacement that increases linearly in time. This paradigm constitutes the basis of numerous applications ranging from colloidal suspensions, emulsions, and simple polymeric solutions to many biological systems.

From this perspective, the emergence of *anomalous transport* in more complex materials, typically characterised by a sublinear increase of the mean-square displacement, appears as exotic. Yet experiments from many different areas reveal that anomalous transport is ubiquitous in nature, signalling that slow transport may be generic for complex heterogeneous materials; examples are crowded biological media, polymeric networks, porous materials, or size-disparate mixtures. One prominent ingredient common to many of these systems is that they are densely packed, known as *macromolecular crowding* in the biophysics community. The presence of differently sized proteins, lipids, and sugars in the cell cytoplasm, as well as the filamentous networks permeating the cell, is believed to be at the origin of the observed slowing down of transport, rendering diffusion constants meaningless that were measured in dilute solution. Similarly in heterogeneous materials displaying pores of various sizes, the agents interact strongly with surfaces of complex shape giving rise to an entire hierarchy of time scales, which implies a power-law increase of the mean-square displacement.

The goal of this review is to provide a pedagogical overview of the existing theoretical framework on anomalous transport and to discuss distinguished experiments from the different fields, thus establishing a common language for the observations coming from various experimental techniques. The focus here is on crowded biological systems *in vivo* and *in vitro* both in the bulk systems such as the cytoplasm or biological model solutions as well as in planar systems, for example, crowded cellular membranes. We also want to emphasise the similarities with complex heterogeneous materials as they naturally occur, e.g., porous rock, to technologically relevant materials such as molecular sieves and catalysts.

In Section 2, we provide some elementary background to quantify the stochastic motion of a single particle in a complex disordered environment. We recall the standard arguments that underlie the theory of Brownian motion both on the level of an ensemble average (Fickian diffusion) as well as in terms of single-particle trajectories. In particular, we rederive the

widely used mean-square displacement of a tracer and more generally the entire two-time conditional probability density. Thereby, we introduce some notation that will be employed throughout the review and exemplify the important concept of scaling. Then we contrast complex transport from normal transport by requiring that deviations from normal transport are persistent way beyond the natural time scales of the system. The most celebrated indicator is the subdiffusive increase of the mean-square displacement. A second example which has drawn significant interest in the statistical physics community, although almost entirely ignored by biophysicists, is given by the velocity autocorrelation function. We recall that even the case of a single particle in a simple solvent encodes non-trivial correlations and long-time anomalies due to the slow diffusion of transverse momentum. Further, we emphasise that anomalous transport can no longer be described by a single diffusion *constant*, rather the transport properties depend on the considered length and time scales. Thus, it is essential to make testable predictions for the spatio-temporal behaviour, which we elucidate in terms of the nongaussian parameter and, more generally, the shape of the distribution of displacements.

The theoretical description of the phenomenon of anomalous transport is reviewed in Section 3. We focus on the three most widely used concepts each of which has been corroborated from some experiments and excluded from others. The first one consists of relaxing the white-noise assumption in a Langevin approach. Then to induce a sublinear increase of the mean-square displacement a power-law time correlation has to be imposed on the increments while the probability distribution is still assumed to be gaussian. In this simple model, one easily derives two-time correlation functions such as the van Hove correlation function or its spatial Fourier transform, the intermediate scattering function. Simple generalisations to models where the correlation functions encode only a power-law tail at long times then lead to the gaussian model. A second, complementary approach is given in terms of a distribution of waiting times characteristic of the complex medium. The class of these models is known as the continuous-time random walk model and allows for a simple solution after a Fourier–Laplace transform to the complex frequency domain. While these two descriptions are phenomenological in nature, the third concept is a microscopic approach that also provides insight into the mechanism how subdiffusion can emerge from simple dynamic rules in a complex environment. In this class, which we refer to as Lorentz models, the origin of slow transport is found in an underlying geometric percolation transition of the void space to which the tracer is confined. We recall how self-similar, fractal structures emerge and why transport in these systems is naturally subdiffusive. We compare different microscopic dynamics and discuss the crossover to heterogeneous diffusion at long time scales, scaling behaviour, and

the appearance of an immobile fraction of particles.

The section is concluded by delimiting the scope of the review to subdiffusion that is related to molecular crowding or the excluded volume effect. Polymer physics and single-file diffusion, where subdiffusive motion is well known too, will not be covered here. In addition, while many experimental data are interpreted in terms of subdiffusion, some of them actually display only deviations from normal transport that are not persistent over large time windows. Hence one has to be careful whether one speaks of subdiffusion or simple crossover scenarios. Typical examples where such apparent subdiffusion is observed comprise diffusion of more than one species each moving with its own diffusion coefficient. In the same spirit a particle could change its conformation thus exhibiting several internal states again characterised by several diffusive regimes. Sometimes, the data only suggest power laws which could be interpreted as subdiffusion, yet the correlations are due to the measurement technique and have no relation to the underlying physical processes.

Sections 4 and 5 review anomalous diffusion in crowded biological systems from an experimental point of view. We first introduce the experimental techniques that have proved themselves as useful tools in biophysics to measure transport properties in mesoscopic samples and on microscopic scales. An important technique that is both intuitive and powerful is provided by single-particle tracking. Here the trajectory of some agent in a complex environment is recorded over sufficiently long time, allowing for the evaluation of, in principle, all correlation functions. The most widely used quantity is of course the mean-square displacement, since it is rather robust with respect to statistical fluctuations and appears easy to interpret. A second powerful method that has been widely applied in the biophysical context is fluorescence correlation spectroscopy. Here the basic idea is to label few molecules by a fluorescent dye and record the fluctuating fluorescent light upon illuminating a small part of the sample with a laser. We briefly introduce the theory underlying the measurement and discuss how anomalous transport manifests itself in the corresponding correlation function. Complementary to these two single-particle methods is fluorescence recovery after photobleaching, which detects the diffusion front of fluorophores after depleting a small spot by an intense laser pulse. The technique is apt to measure very slow transport and immobile particles, and we outline how anomalous transport becomes manifest in the recovery curve as function of time.

Section 5 is devoted to the plethora of experiments on anomalous transport in the cell interior and related model systems and their interpretation in terms of the three theoretical frameworks introduced before. We have compiled and discuss the most significant experiments in the field, focusing on the past decade. Almost all experiments agree that transport is hindered and slowed down by molecular crowding, manifested in a suppression of the diffusion constant. A large subset of

experiments provides clear evidence for subdiffusive motion, but there are notable experiments which report normal diffusion, and some findings appear to be specific to certain biological conditions. Important progress in the understanding of anomalous transport was made by biologically motivated model systems, where in contrast to living cells key parameters are adjustable. The discussion is completed by addressing computer simulations of simple and complex model systems, which provide essential support for the interpretation of experiments. The presentation is divided into three-dimensional transport in cellular fluids, e.g., in the cytoplasm of living cells, and transport in cellular membranes, which may be approximated as a (curved) two-dimensional manifold. Finally, the consequences of anomalous transport on reaction kinetics are briefly sketched and some recent progress on this emerging topic is reported.

In Section 6, we first summarise what the state of the art in the field of anomalous transport currently is and provide some general conclusions on what has been achieved so far both theoretically and experimentally. We point out which questions are still under debate and give suggestions where future research may go and what crucial issues still need to be addressed.

2. Basics of Brownian motion

The naming of the observation of *anomalous transport* frequently found in complex systems already suggests that the phenomena are fundamentally different from the standard case that therefore qualifies as normal transport. Before reviewing how anomalous transport can be addressed theoretically and measured experimentally, we discuss the framework for normal transport connecting macroscopic diffusion with fluctuations at small scales.

The erratic movement of a mesosized particle suspended in a simple solvent is referred to as *Brownian motion*, after the Scottish botanist Robert Brown, who observed the continuously agitated motion of minute particles ejected from certain pollen grains under a light microscope. The first theoretical description has been achieved independently by Einstein [1] and Smoluchowski [2] in terms of a probabilistic approach. These ideas have been rephrased shortly after by Langevin [3, 4] in terms of stochastic differential equations by separating the force balance into a deterministic and a random part. The characterisation of the random forces is largely due to Ornstein [5] thereby laying the foundations of the modern calculus of Langevin equations.

The experimental demonstration of the probabilistic route to a macroscopic law has been achieved by Perrin [6] and his students around the same time by meticulously analysing single trajectories of colloidal particles observed under a microscope. His contribution was awarded with the Nobel prize in 1926 as a breakthrough in proving the physical reality of

molecules.

The impact of Einstein's theory on Brownian motion, i.e., the normal case, can hardly be underestimated and constitutes one of the milestones in physics. Recently, on the occasion of 100th anniversary of Einstein's *annus mirabilis* 1905, a series of reviews have been published highlighting the new concepts and future directions in the field of Brownian motion [7–10].

2.1. Simple diffusion

In the molecular kinetic approach advocated by Einstein and Smoluchowski the suspended particle experiences rapid collisions with the solvent molecules. These events occur at the time scale of the liquid dynamics, typically in the picosecond regime, and at each encounter a tiny amount of momentum is exchanged. Simultaneously, the collisions are responsible for the macroscopic friction force counteracting the random kicks. At the time scales where the suspended particle moves significantly, the increments $\Delta \mathbf{R}(t) = \mathbf{R}(t+t') - \mathbf{R}(t')$ after an elapsed time t are considered as random variables that are identically and independently distributed. By the central-limit theorem, the total displacement, being the sum of many independent tiny increments, then is governed by a gaussian distribution

$$P(\mathbf{r}, t) = [2\pi\delta r^2(t)/d]^{-d/2} \exp(-\mathbf{r}^2/2\delta r^2(t)), \quad (1)$$

where d is the dimension of the embedding space. The probability distribution $P(\mathbf{r}, t)$ is known in general as the *propagator* or the *van Hove self-correlation function* [11, 12]. For independent increments the variance $\delta r^2(t) := \langle [\mathbf{R}(t) - \mathbf{R}(0)]^2 \rangle$ grows linearly with the number of steps, implying a linear increase of the mean-square displacement, $\delta r^2(t) = 2dDt$. The only transport coefficient characterising the Brownian motion is then the diffusion constant D , completely specifying the propagator,

$$P(\mathbf{r}, t) = \frac{1}{(4\pi Dt)^{d/2}} \exp\left(-\frac{\mathbf{r}^2}{4Dt}\right). \quad (2)$$

The self-similarity of free Brownian motion becomes evident by writing the propagator in a scale-free form,

$$P(\mathbf{r}, t) = r^{-d} \mathcal{P}_{\text{gauss}}(\hat{r}), \quad \hat{r} \propto rt^{-1/2}, \quad (3)$$

introducing a dimensionless scaling variable, $\hat{r} := (2Dt)^{-1/2}r$, $r = |\mathbf{r}|$, and a scaling function,

$$\mathcal{P}_{\text{gauss}}(\hat{r}) = (2\pi)^{-d/2} \hat{r}^d \exp(-\hat{r}^2/2). \quad (4)$$

Other scaling forms will be encountered in the course of this review.

The connection to the macroscopic description arises when considering many particles performing Brownian motion such that the probability cloud $P(\mathbf{r}, t)$ displays the same space-time dynamics as the macroscopic concentration. In particular, one

verifies that the gaussian propagator fulfils the diffusion equation

$$\partial_t P(\mathbf{r}, t) = D\nabla^2 P(\mathbf{r}, t), \quad (5)$$

and satisfies the initial condition of a spatially localised distribution, $P(\mathbf{r}, t) = \delta(\mathbf{r})$.

For applications, a representation in terms of spatial Fourier modes is advantageous, $P(\mathbf{k}, t) = \int d^d r e^{-i\mathbf{k}\cdot\mathbf{r}} P(\mathbf{r}, t)$, and $P(\mathbf{k}, t)$ is known as the (self-)intermediate scattering function [11, 12]. It can be measured directly by neutron scattering employing the spin-echo technique [13] or, on larger length scales, by photon correlation spectroscopy [14]. The momentum transferred from the sample to the photon or neutron is then simply $\hbar\mathbf{k}$. For the diffusion propagator, one readily calculates

$$P(\mathbf{k}, t) = \exp(-Dk^2 t), \quad (6)$$

implying that density modulations decay with a rate $1/\tau_k = Dk^2$. Then, long-wavelength perturbations are long-lived since by particle conservation the relaxation involves transport of particles over large distances.

For future reference, we also provide the van Hove correlation function in the complex frequency domain,

$$P(\mathbf{r}, \omega) = \int_0^\infty e^{i\omega t} P(\mathbf{r}, t) dt, \quad \text{Im}[\omega] \geq 0. \quad (7)$$

The one-sided Fourier transform reduces to the standard Laplace transform, provided one identifies $s = -i\omega$; the advantage of introducing complex frequencies as above is that the transform can be readily inverted numerically by evaluating the integral

$$P(\mathbf{r}, t) = \frac{2}{\pi} \int_0^\infty \text{Re}[P(\mathbf{r}, \omega)] \cos(\omega t) d\omega. \quad (8)$$

For the diffusive propagator one finds

$$P(\mathbf{r}, \omega) = \frac{1}{(2\pi D)^{d/2}} \left(\frac{\sqrt{-i\omega D}}{r} \right)^{d/2-1} K_{d/2-1} \left(r \sqrt{\frac{-i\omega}{D}} \right), \quad (9)$$

where $K_\nu(\cdot)$ denotes the modified Bessel function of the second kind. The expression simplifies for the dimensions of interest,

$$P(\mathbf{r}, \omega) = \frac{1}{2\sqrt{-i\omega D}} \exp\left(-r\sqrt{\frac{-i\omega}{D}}\right) \quad (d=1), \quad (10a)$$

$$P(\mathbf{r}, \omega) = \frac{1}{2\pi D} K_0\left(r\sqrt{\frac{-i\omega}{D}}\right) \quad (d=2), \quad (10b)$$

$$P(\mathbf{r}, \omega) = \frac{1}{4\pi D r} \exp\left(-r\sqrt{\frac{-i\omega}{D}}\right) \quad (d=3). \quad (10c)$$

In scattering techniques, where the energy transfer to the sample is also recorded, the central quantity is the frequency- and wavenumber-dependent scattering function $P(\mathbf{k}, \omega) =$

$\int_0^\infty e^{i\omega t} P(\mathbf{k}, t) dt$. The scattering cross section corresponding to an energy transfer $\hbar\omega$ and a momentum transfer $\hbar\mathbf{k}$ is then essentially given by $\text{Re}[P(\mathbf{k}, \omega)]$, known as the (incoherent) dynamic structure factor [11]. In the case of simple diffusion, the dynamics is represented by a simple pole on the negative imaginary axis,

$$P(\mathbf{k}, \omega) = \frac{1}{-i\omega + Dk^2}. \quad (11)$$

An equivalent way to characterise the dynamics of a tracer is to give a prescription on how individual trajectories are generated as a result of the stochastic fluctuations in the medium [15, 16]. The propagator $P(\mathbf{r}, t)$ is then the result of a suitable average over the possible individual realisations of the jittery motion for the tracer. The equations of motion naturally become stochastic differential equations referred to as *Langevin equations*, which incorporate the randomness of the kicks by the medium as “noise”. The modern formulation in terms of a Langevin equation is mostly due to Ornstein, who shaped the notion of what is now known as random gaussian white noise. A mathematical rigorous introduction to the stochastic differential equations and Brownian motion can be found in the excellent textbook by Øksendal [17].

For overdamped motion, the displacements $\mathbf{R}(t)$ are assumed to obey the stochastic differential equation

$$\partial_t \mathbf{R}(t) = \boldsymbol{\eta}(t), \quad (12)$$

with noise terms $\boldsymbol{\eta}(t) = (\eta_1(t), \dots, \eta_d(t))$ that are considered as independent, random quantities on sufficiently coarse-grained time scales. In fact, these $\eta_i(t)$, $i = 1, \dots, d$, represent already averages over many independent processes occurring on even shorter time scales such that the central-limit theorem applies. The probability distribution then corresponds to a multivariate gaussian, symbolically written as $P[\boldsymbol{\eta}(t)] \propto \mathcal{D}[\boldsymbol{\eta}(t)] \exp(-\int dt \boldsymbol{\eta}(t)^2 / 4D)$, which is characterised completely by the only non-vanishing cumulant [15],

$$\langle \eta_i(t) \eta_j(t') \rangle = 2D\delta_{ij}\delta(t - t'), \quad i, j = 1, \dots, d. \quad (13)$$

Such a noise displays only short-time correlations and corresponds to a power spectral density that is flat at the frequencies of interest, commonly referred to as *white* noise. We have imposed that different Cartesian directions $\eta_i(t)$ are uncorrelated and, invoking isotropy, the strength of the noise, $2D$, is identical for all directions. The idea of coarse-graining and the seemingly innocent assumption of independence then necessarily leads to gaussian white noise as the universal law for the statistics of the displacements at small times. Any deviation from this law indicates the existence of non-trivial persistent correlations in the system.

The displacement after a finite lag time follows from formally integrating the Langevin equation, $\Delta \mathbf{R}(t) = \mathbf{R}(t) - \mathbf{R}(0) = \int_0^t dt' \boldsymbol{\eta}(t')$, and being a sum of gaussian variables, it

obeys again a gaussian distribution. Thus it suffices to calculate the first two cumulants. Since the mean of the noise vanishes, one infers $\langle \Delta \mathbf{R}(t) \rangle = 0$, and the correlation function of the displacements follows from the delta-correlated noise as

$$\langle \Delta R_i(t) \Delta R_j(t) \rangle = 2Dt\delta_{ij}. \quad (14)$$

In particular, one recovers $\delta r^2(t) = \langle \Delta \mathbf{R}(t)^2 \rangle = 2dDt$, and the probability distribution is determined by the diffusion propagator, Eq. (2).

2.2. Anomalous and complex transport

The probabilistic reasoning presented in the previous subsection suggests that normal diffusion emerges as a statistical law essentially by the central-limit theorem. In particular, the mean-square displacement is expected to increase linearly in time for time scales much larger than microscopic ones. In simple systems such as normal liquids [11, 12] one observes diffusion already at time scales exceeding the picosecond scale. The phenomena of anomalous or complex transport deal with dynamics where this diffusive regime is not visible even on time scales that are by many orders of magnitude larger than picoseconds. Conventionally, a non-linear growth of the mean-square displacement $\delta r^2(t)$ is taken as indicator of such unusual behaviour. Typically, the mean-square displacement is proportional to a power law, $\delta r^2(t) \propto t^\alpha$, with an exponent $0 < \alpha < 1$. Hence the mean-square displacement increases slower than for normal diffusion, formally the diffusion coefficient becomes zero, nevertheless the tracer is not localised. This kind of behaviour is referred to as *subdiffusion* or *anomalous transport*¹. Theoretically, the phenomenon then calls for reasons why the central-limit theorem does not apply at the time scales of interest. Rephrasing the argument in terms of increments reveals that persistent correlations are hidden in the dynamics on meso- or macroscopic time scales.

We would like to make a distinction between a simple violation of the central-limit theorem in some intermediate time window and mechanisms leading to subdiffusive behaviour that can in principle persist forever. In the first case some dynamic processes are unusually slow that spoil the central-limit theorem on these scales, yet ultimately normal transport sets in. This scenario of complex transport occurs generically by having constituents of the medium of different sizes or soft interactions, e.g., polymers. Then the mean-square displacement displays only a crossover from some short-time motion to long-time diffusion. Since the crossover can extend over several decades (due to a series of slow processes occurring in the medium), fits by power laws are often a satisfactory description. In the second case, the correlations in the increments decay slowly and upon tuning suitable control parameters the window of subdiffusion can become arbitrarily long.

¹ In different contexts one finds also superdiffusive transport corresponding to $\alpha > 1$, which is beyond the scope of this review.

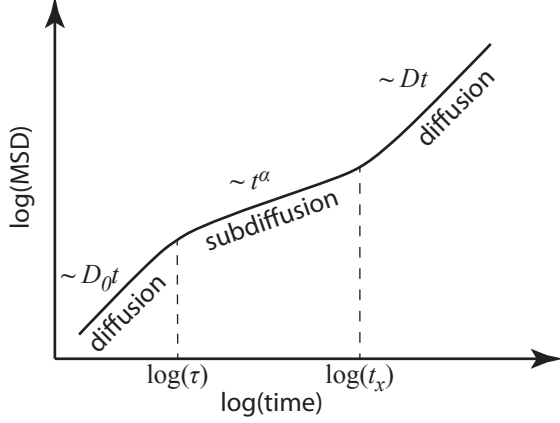


Figure 1. Schematic mean-square displacement (MSD) for intermediate subdiffusive transport. Free diffusion at microscopic scales is followed by subdiffusive transport at intermediate time scales. In a physical system, the subdiffusive growth ends typically at a second crossover, where the MSD grows linearly again with reduced diffusion constant, $D \ll D_0$, or where it saturates, e.g., due to boundaries like the cell membrane.

Hence in a well-defined limit the subdiffusion persists forever and the central-limit theorem never applies. We reserve the term *anomalous transport* for the latter scenario. Typically, the mean-square displacement is expected to display two crossover time scales, see Fig. 1 and Ref. 18, which is also found in experiments [19]. The long-time diffusion coefficient is then strongly suppressed compared to the microscopic motion at short times, for example, subdiffusion with $\alpha = 0.6$ over 4 decades in time yields a reduction of D over D_0 by a factor of $(t_x/\tau)^{1-\alpha} = 10^{4 \times 0.4} \approx 40$. We postpone the discussion what physical mechanisms can lead to such drastic changes and focus here on the measurable quantities suited to reveal complex and anomalous transport.

2.2.1. Van Hove self-correlation function

The basic observable is the fluctuating single-particle density, $\rho(\mathbf{r}, t) = \delta(\mathbf{r} - \mathbf{R}(t))$, and the corresponding correlation function, $P(\mathbf{r} - \mathbf{r}', t - t') = V \langle \rho(\mathbf{r}, t) \rho(\mathbf{r}', t') \rangle$, is referred to as van Hove (self-)correlation function [11]. Here V is the volume of the container and the thermodynamic limit $V \rightarrow \infty$ is anticipated. Furthermore by translational invariance and for a stationary stochastic process, P depends only on the elapsed time $t - t'$ and the accumulated displacement $\mathbf{r} - \mathbf{r}'$. Then the van-Hove correlation function can be cast into the form $P(\mathbf{r}, t) = \langle \delta(\mathbf{r} - [\mathbf{R}(t) - \mathbf{R}(0)]) \rangle$ which is interpreted directly as probability density for an observed displacement \mathbf{r} after a lag time t . Furthermore for isotropic systems, to which we restrict the discussion, only the magnitude $r = |\mathbf{r}|$ enters the van Hove function.

The first generalisation of simple diffusion consists of assuming that the increments $\Delta \mathbf{R}(t)$ follow a gaussian probability distribution with zero mean,

$$P_{\text{gauss}}(\mathbf{r}, t) = \frac{1}{[2\pi\delta r^2(t)/d]^{d/2}} \exp\left(\frac{-r^2}{2\delta r^2(t)/d}\right). \quad (15)$$

Here the mean-square displacement $\delta r^2(t)$ characterises the width of the distribution; for ordinary diffusion, it holds $\delta r^2(t) = 2dDt$, of course. The higher moments,

$$\delta r^n(t) := \langle |\Delta \mathbf{R}(t)|^n \rangle = \int d^d r |\mathbf{r}|^n P(\mathbf{r}, t), \quad (16)$$

are obtained by performing gaussian integrals, for example, one finds for the mean-quartic displacement, $\delta r^4(t) = [(d+2)/d][\delta r^2(t)]^2$.

Equivalently to the van Hove function, one can study the single-particle dynamics by monitoring the decay of density fluctuations in the wavenumber representation $\rho(\mathbf{k}, t) = \exp(i\mathbf{k} \cdot \mathbf{R}(t))$. The corresponding correlation function, $P(k, t) = \langle \rho(\mathbf{k}, t) \rho(\mathbf{k}, 0) \rangle$, is the (self-)intermediate scattering function and merely the spatial Fourier transform of the van Hove function. Again by isotropy, $P(k, t)$ depends only on the magnitude $k = |\mathbf{k}|$ of the wavenumber. The explicit representation $P(k, t) = \langle \exp[-i\mathbf{k} \cdot \Delta \mathbf{R}(t)] \rangle$ permits an interpretation of $P(k, t)$ as the characteristic function of the random variable $\Delta \mathbf{R}(t)$, such that the lowest order moments can be obtained from a series expansion for small wavenumbers, $k \rightarrow 0$,

$$P(k, t) = 1 - \frac{k^2}{2d} \delta r^2(t) + \frac{k^4}{8d(d+2)} \delta r^4(t) + O(k^6). \quad (17)$$

Here we used that the orientational average over a d -dimensional sphere yields² $\overline{\cos^2 \vartheta} = 1/d$, $\overline{\cos^4 \vartheta} = 3/d(d+2)$.

The logarithm of the characteristic function generates the cumulants,

$$\ln P(k, t) = -\frac{k^2}{2d} \delta r^2(t) + \frac{k^4}{8d^2} \left[\frac{d}{d+2} \frac{\delta r^4(t)}{[\delta r^2(t)]^2} - 1 \right] + O(k^6), \quad k \rightarrow 0. \quad (18)$$

In the case of gaussian transport, the Fourier transform of Eq. (15) yields $P_{\text{gauss}}(k, t) = \exp(-k^2 \delta r^2(t)/2d)$, and all cumulants apart from the second one, $\delta r^2(t)$, vanish identically. Thus a simple, dimensionless indicator for transport be-

² Let n_i be the Cartesian components of a unit vector. Then by symmetry one argues that

$$\overline{n_i n_j} = A \delta_{ij} \\ \overline{n_i n_j n_k n_l} = B(\delta_{ij} \delta_{kl} + \delta_{ik} \delta_{jl} + \delta_{il} \delta_{jk}),$$

where $\overline{\dots}$ indicates a spherical average. Contracting the indices i and j in the first relation reveals $A = 1/d$, contracting in the second shows $B = 1/d(d+2)$. Thus $\overline{n_z^4} = 3/d(d+2)$.

yond the gaussian approximation is the non-gaussian parameter [11, 12],

$$\alpha_2(t) := \frac{d}{d+2} \frac{\delta r^4(t)}{[\delta r^2(t)]^2} - 1. \quad (19)$$

The subscript indicates that there is an entire series of similarly defined quantities involving higher moments of the displacements. The inequality $\langle X^2 \rangle \geq \langle X \rangle^2$ for the random variable $X = |\Delta \mathbf{R}(t)|^2$ implies a lower bound on the non-gaussian parameter, $\alpha_2(t) \geq -2/(d+2)$.

The fact that probability theory imposes certain constraints on $P(k, t)$ as a function of wavenumber k naturally poses the question if additional conditions apply if $P(k, t)$ is considered as a function of time t . More generally, what class of functions are permissible for correlation functions? Decompose the fluctuation density into Fourier modes $\rho_T(\mathbf{k}, \omega) = \int_{-T/2}^{T/2} dt e^{-i\omega t} \rho(\mathbf{k}, t)$ for real frequencies ω and a long but finite observation time $T > 0$. Then the corresponding *power spectral density* is obtained via the Wiener–Khinchin theorem [15, 16],

$$\lim_{T \rightarrow \infty} \frac{1}{T} \left\langle |\rho_T(\mathbf{k}, \omega)|^2 \right\rangle = 2 \operatorname{Re}[P(k, \omega)]. \quad (20)$$

Thus $\operatorname{Re}[P(k, \omega)] \geq 0$ and inversion of the one-sided Fourier transform yields

$$P(k, t) = \frac{2}{\pi} \int_0^\infty \operatorname{Re}[P(\mathbf{k}, \omega)] \cos(\omega t) d\omega, \quad (21)$$

i.e., the propagator is the cosine transform of a non-negative function. Transforming again to complex frequencies by one-sided Fourier transform one derives relations of the Kramers–Kronig type [20, 21]; in particular, one observes that $\operatorname{Re}[P(k, \omega)] \geq 0$ not only for real but for all complex frequencies in the upper half-plane, $\operatorname{Im}[\omega] > 0$.

Since the particle is to be found somewhere a particle conservation law holds, and the intermediate scattering function approaches unity in the long-wavelength limit, $\lim_{\mathbf{k} \rightarrow 0} P(\mathbf{k}, t) = 1$. For the one-sided Fourier transform, the particle conservation law suggests the representation $P(k, \omega) = 1/[-i\omega + k^2 D(k, \omega)]$, where $D(k, \omega)$ is known as the frequency- and wavenumber-dependent diffusion kernel [11, 12]. From $\operatorname{Re}[P(k, \omega)] \geq 0$ for $\operatorname{Im}[\omega] > 0$ the same property is inherited for the diffusion kernel, $\operatorname{Re}[D(k, \omega)] \geq 0$.

Of particular interest is the long-wavelength limit $Z(\omega) = D(k \rightarrow 0, \omega)$, which encodes the spatial second moment of the tracer motion. Note again $\operatorname{Re}[Z(\omega)] \geq 0$ for $\operatorname{Im}[\omega] > 0$. Expanding for small wavenumber,

$$P(k, \omega) = \frac{1}{-i\omega + k^2 D(k, \omega)} = \frac{1}{-i\omega} - \frac{k^2 Z(\omega)}{(-i\omega)^2} + \mathcal{O}(k^4), \quad (22)$$

and comparing to Eq. (17), one finds $Z(\omega) = -(\omega^2/2d) \int_0^\infty dt e^{i\omega t} \delta r^2(t)$. Integration by parts reveals

that $Z(\omega)$ is the one-sided Fourier transform of the velocity autocorrelation function (VACF),

$$Z(\omega) = \frac{1}{d} \langle \mathbf{v}(t) \cdot \mathbf{v}(0) \rangle = \frac{1}{2d} \frac{d^2}{dt^2} \delta r^2(t). \quad (23)$$

Reversely, the mean-square displacement is obtained by integration,

$$\delta r^2(t) = 2d \int_0^t dt' (t-t') Z(t'). \quad (24)$$

For stochastic processes where the derivative of the increments $\Delta \mathbf{R}(t)$ does not exist, e.g., for a Brownian particle, the VACF may be defined via the mean-square displacement and can be shown to be a negative and completely monotone function [22].

In the case of ordinary diffusion, $\delta r^2(t) = 2dDt$, the diffusion kernel simply assumes a constant, $D(k, \omega) \mapsto Z(\omega) = D$, and the velocity decorrelates instantaneously, $Z(t) \mapsto D \delta(t-0)$. Furthermore, the non-gaussian parameter vanishes identically, $\alpha_2(t) \equiv 0$, as do all higher cumulants.

2.2.2. Distribution of squared displacements

The measurements of the squared displacements $\Delta \mathbf{R}(t)^2$ for a single particle along its trajectory often does not represent well the *mean*-square displacement $\delta r^2(t)$, rather a significant scattering of the data is observed. This observation suggests to introduce the distribution function for the squared displacements u ,

$$p(u, t) := \left\langle \delta \left(u - \Delta \mathbf{R}(t)^2 \right) \right\rangle. \quad (25)$$

The probability distribution is obviously properly normalised, $\int_0^\infty p(u, t) du = 1$, its mean reproduces the mean-square displacement, and higher moments yield the even displacement moments,

$$\delta r^{2k}(t) = \left\langle |\Delta \mathbf{R}(t)|^{2k} \right\rangle = \int_0^\infty u^k p(u, t) du. \quad (26)$$

The fluctuations in the squared displacements are given by the second cumulant and are via Eq. (19) already encoded in the non-gaussian parameter,

$$\begin{aligned} \operatorname{Var} [\Delta \mathbf{R}^2(t)] &= \left\langle |\Delta \mathbf{R}(t)|^4 \right\rangle - \left\langle \Delta \mathbf{R}(t)^2 \right\rangle^2 \\ &= \left[\frac{d+2}{d} \alpha_2(t) + \frac{2}{d} \right] [\delta r^2(t)]^2. \end{aligned} \quad (27)$$

Rather than dealing with the probability distribution it is often favourable to work with a moment-generating function, which is the Laplace transform of the probability distribution,

$$M(w, t) := \int_0^\infty du e^{-u/w^2} p(u, t) = \left\langle \exp \left(-\Delta \mathbf{R}(t)^2 / w^2 \right) \right\rangle, \quad (29)$$

where the second representation follows from Eq. (25). The convention is chosen such that $1/w^2$ is the variable conjugate

to $\Delta\mathbf{R}(t)^2$, and w carries the dimension of a length. Since the exponential is approximated by unity for small displacements, $\Delta\mathbf{R}(t)^2 \ll w^2$, and rapidly approaches zero for large ones, $\Delta\mathbf{R}(t)^2 \gg w^2$, $M(w, t)$ essentially constitutes the probability for the particle to be still or again within a distance w of its initial position. In Section 4.2, it will be shown how this quantity can be directly measured by fluorescence correlation spectroscopy (FCS), where w corresponds to the beam waist of the illuminating laser [23].

The van Hove correlation $P(\mathbf{r}, t)$ is the probability distribution of all vector displacements \mathbf{r} , and the probability distribution of the squared displacements $p(u, t)$ follows by marginalising,

$$p(u, t) = \int d^d r \delta(u - \mathbf{r}^2) P(\mathbf{r}, t). \quad (30)$$

For the important case of statistically isotropic samples, $P(\mathbf{r}, t)$ depends only on the magnitude of the displacement $r = |\mathbf{r}|$ and the integral can be evaluated. In spherical coordinates, the angular integration yields the surface area of the d -dimensional unit sphere, Ω_d , as a factor. The radial integral collapses due to the Dirac delta function, $\delta(u - r^2) = \delta(\sqrt{u} - r)/2u$, and one obtains

$$p(u, t) = \frac{\Omega_d}{2} u^{(d-2)/2} P(r = \sqrt{u}, t). \quad (31)$$

For gaussian transport, solely characterised by the time-dependent mean-square displacement, $\delta r^2(t)$, Eq. (15) yields

$$p(u, t) = \frac{1}{\Gamma(d/2)} \frac{u^{d/2-1}}{[2\delta r^2(t)/d]^{d/2}} \exp\left(\frac{-u}{2\delta r^2(t)/d}\right); \quad (32)$$

the gamma function evaluates to $\Gamma(d/2) = \sqrt{\pi}, 1, \sqrt{\pi}/2$ for $d = 1, 2, 3$. From these expressions one readily calculates also the cumulative distribution functions, $\int_0^U p(u, t) du$.

The van Hove function $P(\mathbf{r}, t)$ and its spatial Fourier transform, the intermediate scattering function, $P(\mathbf{k}, t)$, the distribution of the squared displacements $p(u, t)$, and the corresponding moment generating function $M(w, t)$ all encode spatio-temporal information on the motion of the tracer. For isotropic systems they are all equivalent in principle, in practice they are sensitive to different aspects of transport occurring on different length scales. Correlation functions that involve more than two times provide even more information on the dynamics, and may hold the key to distinguish different theoretical models that yield the same two-time correlation functions.

3. Theoretical models

The paradigm of anomalous transport is tantamount with a violation of the central-limit theorem on arbitrarily long time scales. Modelling such processes requires including persistent correlations that manifest themselves as self-similar dynamics in the mean-square displacements. Different models and theoretical approaches have been pursued that generically

lead to subdiffusion. Here we focus on the three most widely used frameworks. The perhaps simplest approach is based on stochastic differential equations where the noise term displays persistent correlations which then transfer to the increments. Since usually the statistics of the noise is still assumed to be gaussian, they differ essentially only in the form of the temporal correlations they incorporate and we summarise them as gaussian models. The second category, the continuous-time random walk (CTRW), consists of jump models where particles undergo a series of displacements according to a distribution with large tails. Here the central-limit theorem does not apply since the mean waiting time for the next jump event to occur becomes infinite. The last class of Lorentz models relies on spatially disordered environments where the tracer explores fractal-like structures that induce anomalous dynamics.

3.1. Gaussian models

Here we collect properties of a class of models that give a phenomenological description of complex and anomalous dynamics which all result in gaussian propagators.

3.1.1. Fractional Brownian motion

A simple model for subdiffusion is fractional Brownian motion, introduced rigorously by Mandelbrot and van Ness [24] as superposition of Brownian processes with power-law memory. Here we follow a heuristic approach [25–27] that summarises the essence of fractional Brownian motion. Assuming the stochastic differential equation (12), $\partial_t \mathbf{R}(t) = \boldsymbol{\eta}(t)$, we have already seen that if the noise $\eta_i(t)$ is delta-correlated in time, the mean-square displacements increase linearly. If additionally the noise obeys a gaussian statistics, this property is inherited also for the displacements $\Delta\mathbf{R}(t)$ and transport is completely characterised by the diffusion propagator $P(\mathbf{r}, t)$, Eq. (2). The idea is now to incorporate persistent correlations in the noise such that transport is drastically slowed down with respect to normal diffusion. Since the noise plays the role of a fluctuating velocity, we use the same notation as in Section 2.2, to express the noise correlator in terms of the velocity autocorrelation function,

$$\langle \eta_i(t) \eta_j(t') \rangle = d Z(|t - t'|) \delta_{ij}, \quad i, j = 1, \dots, d. \quad (33)$$

Here the different Cartesian components are taken as uncorrelated, which certainly holds for an isotropic system. In the Fourier domain, this implies

$$\langle \eta_i(\omega)^* \eta_j(\omega') \rangle = 4\pi d \delta_{ij} \delta(\omega - \omega') \text{Re}[Z(\omega)], \quad (34)$$

where $Z(\omega) = \int_0^\infty e^{i\omega t} Z(t) dt$ is again the one-sided Fourier transform of the velocity autocorrelation function. For ordinary diffusion, $Z(\omega) = D$ is constant and the noise corresponds to white noise.

The case of subdiffusion, $\delta r^2(t) = 2dK_\alpha t^\alpha$ with an exponent $0 < \alpha < 1$ and a generalised diffusion coefficient $K_\alpha > 0$, then yields a spectral density $Z(\omega) = (-i\omega)^{1-\alpha} K_\alpha \Gamma(1+\alpha)$ [24]. Hence the strength of the noise approaches zero as the frequencies become smaller, which explains that transport slows down with increasing correlation time. In the temporal domain, $Z(t)$ is represented by a pseudofunction³,

$$Z(t) = \alpha(\alpha - 1)K_\alpha \text{Pf} |t|^{\alpha-2}. \quad (35)$$

Up to here only the mathematical frame has been set and no assumptions on the nature of the stochastic process has been made.

In fractional Brownian motion, the statistics of the noise correlator is assumed to be characterised by the only non-vanishing cumulant $Z(t)$, Eqs. (33) and (35), i.e., a stationary gaussian process although not white noise. Then the statistics of the increments $\Delta \mathbf{R}(t)$ is again gaussian, and the propagator reduces to $P_{\text{gauss}}(\mathbf{r}, t)$, Eq. (15). Its scaling form corresponds to that of simple diffusion, Eq. (3),

$$P_{\text{FBM}}(r, t) = r^{-d} \mathcal{P}_{\text{gauss}}(\hat{r}), \quad \hat{r} \propto r t^{-\alpha/2}, \quad (36)$$

sharing the gaussian scaling function, Eq. (4), but not the scaling variable, \hat{r} . In particular, the non-gaussian parameter $\alpha_2(t) \equiv 0$ vanishes by the construction of fractional Brownian motion.

In contrast to simple diffusion, fractional Brownian motion is not a Markov process; in particular, the van Hove correlation function is not sufficient to characterise the statistical properties completely. Multiple-time correlation functions encode non-Markovian behaviour, for which fractional Brownian motion makes detailed predictions. As an example,

$$\begin{aligned} & \langle [\mathbf{R}(t) - \mathbf{R}(0)]^2 [\mathbf{R}(t+T) - \mathbf{R}(T)]^2 \rangle \\ &= 4d^2 K_\alpha^2 t^{2\alpha} + 2dK_\alpha^2 (|t+T|^\alpha + |t-T|^\alpha - 2T^\alpha)^2, \end{aligned} \quad (37)$$

which has been derived recently to study the ergodic properties of fractional Brownian motion [29]. For $T = 0$, this expression reproduces the quartic moment, $\delta r^4(t)$, and is compatible with a vanishing non-gaussian parameter, Eq. (19).

3.1.2. Langevin equations for visco-elastic media

The erratic motion of a spherical particle immersed in a complex medium can be described quite generally by a Langevin equation. Rather than directly addressing the displacements one may base the description on the velocity $\mathbf{v}(t) = \dot{\mathbf{R}}(t)$ and formulate a force balance equation. The paradigm has been given by Langevin [3] himself,

$$m\dot{\mathbf{v}}(t) = -\zeta \mathbf{v}(t) + \mathbf{f}(t), \quad (38)$$

³ The noise correlator corresponds to a distribution, and pseudofunction means that integrals with test functions $\varphi(t)$ extract only Hadamard's finite part [28], $\int \varphi(t) \text{Pf} |t|^{\alpha-2} dt := \int [\varphi(t) - \varphi(0)] |t|^{\alpha-2} dt$. In particular, one easily verifies that the one-sided Fourier transform of $Z(t)$ yields $Z(\omega)$.

where m denotes the mass of the particle, the deterministic friction force $-\zeta \mathbf{v}(t)$ is merely the Stokes drag, and $\mathbf{f}(t)$ is a fluctuating force with zero mean, $\langle f_i(t) \rangle = 0$. The friction constant constant, $\zeta = 6\pi\eta a$, is directly connected to the solvent viscosity η and the particle radius a . The statistics of the random forces $\mathbf{f}(t)$ is characterised completely by the only non-vanishing cumulant [5],

$$\langle f_i(t) f_j(t') \rangle = 2k_B \mathcal{T} \zeta \delta_{ij} \delta(t - t'), \quad (39)$$

where \mathcal{T} is the temperature of the environment and k_B denotes Boltzmann's constant. Thus the Cartesian components $f_i(t)$ of the forces are gaussian distributed and independent for different times. The variance at equal times is again dictated by the fluctuation–dissipation theorem, see, e.g., Ref. 15 for details. The delta-correlation in the temporal domain for the forces translates to white noise for the corresponding power spectral density. The velocity autocorrelation then decays exponentially [3],

$$\langle v_i(t) v_j(t') \rangle = (k_B \mathcal{T} / m) \delta_{ij} \exp(-|t - t'| / \tau_p), \quad (40)$$

where $\tau_p = m / \zeta = m / 6\pi\eta a$ is the momentum relaxation time. Similarly, the mean-square displacement of the d -dimensional motion is calculated to

$$\delta r^2(t) = 2dD \left[t + \tau_p \left(e^{-t/\tau_p} - 1 \right) \right], \quad (41)$$

where $D = k_B \mathcal{T} / \zeta$ is the diffusion constant according to the Stokes–Einstein relation.

The description can be easily generalised for the case of visco-elastic media [30]. Here the response of the complex solvent to shear is encoded in the complex frequency-dependent viscosity, $\eta(\omega)$. In the conventions employed in this review, $\text{Re}[\eta(\omega)] \geq 0$ corresponds to the dissipative part and $\text{Im}[\eta(\omega)]$ encodes the reactive part. Equivalently, one may employ the complex shear modulus $G(\omega) := -i\omega\eta(\omega)$. For example, in the Maxwell model, $G(\omega) = -i\omega\tau_M G_\infty / (1 - i\omega\tau_M)$, the modulus is characterised by a high-frequency elastic response G_∞ and a crossover time scale τ_M . The Stokes drag in a visco-elastic medium then depends on the frequency and the Langevin equation is discussed conveniently in the Fourier domain [31],

$$-i\omega m \mathbf{v}(\omega) = -\zeta(\omega) \mathbf{v}(\omega) + \mathbf{f}(\omega), \quad (42)$$

where $\zeta(\omega) = 6\pi\eta(\omega)a$ replaces the Stokes friction coefficient. By the fluctuation–dissipation theorem, the force correlator has to be modified accordingly,

$$\langle f_i(\omega)^* f_j(\omega') \rangle = 4\pi k_B \mathcal{T} \text{Re}[\zeta(\omega)] \delta_{ij} \delta(\omega - \omega'). \quad (43)$$

Since the fluctuations arise in the surrounding solvent as a sum over uncorrelated regions, the forces are again assumed to be gaussian. Then it is clear that the van Hove correlation

function for the particle corresponds to a gaussian propagator and the dynamics is specified entirely by the mean-square displacement, $\delta r^2(t)$. Rather than solving for $\delta r^2(t)$, we solve for the one-sided Fourier transform of the velocity autocorrelation function [30, 31],

$$Z(\omega) = \frac{k_B \mathcal{T}}{-i m \omega + \zeta(\omega)}. \quad (44)$$

Relying on the relation $\zeta(\omega) = 6\pi\eta(\omega)a$, the local visco-elastic response of a complex medium is inferred from the motion of tracer particles in microrheology experiments [30].

Subdiffusion at long times is obtained if $Z(\omega) = (-i\omega)^{1-\alpha} K_\alpha \Gamma(1+\alpha)$ for $\omega \rightarrow 0$ [25], i.e., the elastic modulus displays power-law behaviour, $G(\omega) \sim (-i\omega)^\alpha$, which appears to be generic in many biological materials and soft matter systems for intermediate frequencies. This empirical observation is formulated in the *soft glassy rheology model* [32]. The microscopic mechanism remains in general unspecified, yet for the case of a solution of semiflexible polymer networks, the bending rigidity of a single filament suggests an elastic power-law response, $G(\omega) \sim (-i\omega)^{3/4}$ [33–36]. Similarly, by coupling to the elastic degrees of freedom of a membrane, effective fractional friction kernels can be generated in the same way with various exponents depending on the level of description of the membrane [37, 38]

3.1.3. Long-time anomalies

The assumption of an instantaneous friction term in the Langevin equation (38) is in fact incorrect even at long times, as has been pointed out already by Hendrik Antoon Lorentz. The reason is that the Stokes formula applies for steady motion of the particle only and the friction is accompanied by a long-ranged vortex pattern in the velocity field of the entrained fluid. For unsteady motion, the particle excites incessantly new vortices diffusing slowly through the fluid. As a consequence the friction force depends on the entire history of the particle's trajectory, an effect known as *hydrodynamic memory*. The theoretical description is achieved most conveniently in the frequency domain. The drag force for a sphere performing small-amplitude oscillations of angular frequency ω has already been calculated by Stokes [39] and leads to a frequency-dependent friction coefficient [15],

$$\zeta(\omega) = 6\pi\eta a \left(1 + \sqrt{-i\omega\tau_f}\right) - i\omega m_f/2. \quad (45)$$

For steady motion, $\omega = 0$, the formula reduces to the Stokes drag. The last term appears as an acceleration force for half of the displaced fluid mass, $m_f = 4\pi\rho_f a^3/3$, and it is natural to absorb this contribution by introducing an effective mass for the particle, $m_{\text{eff}} = m + m_f/2$. The second modification is a non-analytic contribution due to the slow vortex diffusion in the liquid as the particle performs unsteady motion. The characteristic time scale, $\tau_f = \rho_f a^2/\eta$, is the time needed for a

vortex to diffuse over the distance of the radius of the particle. By the fluctuation–dissipation theorem, Eq. (43), the spectrum of the random forces is no longer white but displays a coloured component that increases as a square root with frequency. Recently, the power spectral density of the thermal noise has been measured experimentally for a single bead by ultra-sensitive high-bandwidth optical trapping [40] in excellent agreement with theoretical predictions.

The velocity autocorrelation function in the frequency domain, Eq. (44), acts as an admittance or frequency-dependent mobility and displays a non-analytic low-frequency expansion, $Z(\omega) = D \left[1 - \sqrt{-i\omega\tau_f} + O(\omega)\right]$. An explicit expression in the temporal domain is achieved in terms of error functions [41], here we focus on the long-time anomaly,

$$Z(t) \simeq \frac{D}{2} \sqrt{\frac{\tau_f}{\pi}} t^{-3/2}, \quad t \rightarrow \infty, \quad (46)$$

which is a direct consequence of the non-analytic terms in $\zeta(\omega)$. The most striking feature is that $Z(t)$ encodes persistent correlations manifested by a self-similar tail in strong contrast to the exponential decay of Langevin's original theory. These long-time tails have been discovered first in computer simulations for fluids [42, 43] and, only recently, have directly been observed for colloidal particles in suspension [44–47]. The mean-square displacement follows directly by integration,

$$\delta r^2(t) = 6Dt \left[1 - 2\sqrt{\tau_f/\pi t} + O(t^{-1})\right]. \quad (47)$$

The algebraic tail in the velocity autocorrelation manifests itself in a slow approach to normal diffusive transport.

The persistent correlations in the mean-square displacement, buried under the leading linear increase, show that the assumption of independent increments is not satisfied and that the regime of truly overdamped motion is never reached due to the hydrodynamic memory, even at long time scales. Nevertheless the central-limit theorem remains valid, although the convergence is slow due to the persistent power-law correlations induced by vortex diffusion.

3.2. Continuous-time random walks (CTRW)

A different class of models that is widely discussed is the continuous-time random walk (CTRW) [48–51], originally introduced by Montroll and Weiss [52] for hopping transport on a disordered lattice. The particles spend most of the time bound to a trap with an escape time that depends sensitively on the depth of the trap. Rather than dealing explicitly with the quenched disorder on the lattice, the medium is treated as homogeneous with the new ingredient of a waiting-time distribution for the next hopping event to occur. Anomalous transport can be generated within this framework by assuming waiting time distributions such that the mean waiting time becomes infinite. The central-limit theorem does not apply since longer and longer waiting times are sampled. It turns

out that the CTRW as mean-field approximation to hopping in the quenched trap model gives the same result in dimensions 2 and higher [49]. The trapping in biology seems rather natural, due to chemical attachments of molecules in the cell, such that binding on broadly distributed time scales may lead to CTRW dynamics. First we provide the general description of the CTRW model, then we show how subdiffusion can emerge and discuss scaling properties of the propagator.

3.2.1. Model definition

In the CTRW model, the particle is assumed to traverse the d -dimensional space by a series of jumps such that the displacement, ℓ , and the waiting time to perform the next jump, t , are drawn from a given distribution, $\psi(\ell, t)$. For simplicity, we assume that the observation starts when the process is initialised. Hence, a CTRW belongs to the broad class of renewal–reward processes. In particular, the propagator $P(\mathbf{r}, t)$ fulfils a renewal equation [53], which follows by conditioning on the event that the particle has accumulated a displacement \mathbf{r} at time t within the first step. If the first step occurs later than at time t the propagator is simply $\delta(\mathbf{r})$, otherwise the process is renewed [48, 52, 54, 55],

$$P(\mathbf{r}, t) = \delta(\mathbf{r}) \int_t^\infty dt' \int d^d \ell \psi(\ell, t') + \int_0^t dt' \int d^d \ell P(\mathbf{r} - \ell, t - t') \psi(\ell, t'). \quad (48)$$

The first term corresponds to the propagator provided that no jump occurred and can be rewritten as

$$P_0(\mathbf{r}, t) = \delta(\mathbf{r}) \left[1 - \int_0^t dt' \psi(t') \right], \quad (49)$$

where $\psi(t) = \int \psi(\ell, t) d^d \ell$ is the jump probability density irrespective of the size of the jump. The solution of the renewal equation is most easily achieved after a spatial Fourier transform, $P(\mathbf{k}, t) = \int d^d r e^{-i\mathbf{k}\cdot\mathbf{r}} P(\mathbf{r}, t)$, and a subsequent temporal one-sided Fourier transform, $P(\mathbf{k}, \omega) = \int_0^\infty dt e^{i\omega t} P(\mathbf{k}, t)$ for $\text{Im}[\omega] \geq 0$. By the convolution theorem the renewal equation simplifies to $P(\mathbf{k}, \omega) = P_0(\mathbf{k}, \omega) + \psi(\mathbf{k}, \omega)P(\mathbf{k}, \omega)$. The spatio-temporal Fourier–Laplace transform of Eq. (49) can be performed directly, $P_0(\mathbf{k}, \omega) = [1 - \psi(\omega)]/(-i\omega)$. Combining both results yields the Montroll–Weiss relation [48, 54, 56–58] for the propagator in terms of the jump probability distribution,

$$P(\mathbf{k}, \omega) = \frac{1}{-i\omega} \frac{1 - \psi(\omega)}{1 - \psi(\mathbf{k}, \omega)}. \quad (50)$$

In many applications the jump distribution is not known, and additional assumptions are necessary to define the model. First, we assume that the jumps exhibit no preferred direction such that $\psi(\ell, t)$ depends only on the magnitude $|\ell|$. Hence, the dynamics becomes isotropic and $P(\mathbf{k}, \omega)$ is a function of the

wavenumber, $k = |\mathbf{k}|$, only. Second, the waiting-time distribution is often taken to be independent of the jump size, and the corresponding jump distribution factorises, $\psi(\ell, t) = \lambda(\ell) \psi(t)$ such that $\int \lambda(\ell) d^d \ell = 1$. Then the propagator assumes the simple form

$$P(k, \omega) = \frac{1}{-i\omega} \frac{1 - \psi(\omega)}{1 - \lambda(k) \psi(\omega)}, \quad (51)$$

which will be the starting point for the discussion.

We shall assume that the jump size distribution $\lambda(\ell)$ is well-behaved, in particular it decays rapidly for large distances. Then the characteristic function of the jump sizes, $\lambda(k)$, encodes all moments,

$$\lambda(k) = 1 - \frac{k^2}{2d} \langle \ell^2 \rangle + \frac{k^4}{8d(d+2)} \langle \ell^4 \rangle + O(k^6). \quad (52)$$

For the mean-square displacement, only the second moment of the spatial distribution is relevant, $\langle \ell^2 \rangle/d = d^2 \lambda(k)/dk^2|_{k=0}$, and, by Eq. (22), the velocity autocorrelation function is computed to

$$Z(\omega) = \frac{-i\omega \psi(\omega) \langle \ell^2 \rangle}{1 - \psi(\omega) \frac{\langle \ell^2 \rangle}{2d}}. \quad (53)$$

By normalisation of the waiting-time distribution, it holds $\psi(\omega \rightarrow 0) = 1$, and for a well-behaved distribution the low-frequency expansion provides the moments of the waiting time, $\langle \tau \rangle := \int_0^\infty t \psi(t) dt$,

$$\psi(\omega) = 1 + i\omega \langle \tau \rangle + O(\omega^2). \quad (54)$$

In this case, the diffusion coefficient $D = Z(\omega \rightarrow 0)$ is finite with value $D = \langle \ell^2 \rangle / 2d \langle \tau \rangle$.

3.2.2. Anomalous transport

Anomalous transport is obtained if the jump rate distribution is non-analytic at zero frequency, e.g.,

$$\psi(\omega) = 1 - (-i\omega\tau)^\alpha + h.o.t., \quad \omega \rightarrow 0, \quad (55)$$

with non-integer exponent, $0 < \alpha < 1$, some time scale $\tau > 0$, and neglecting higher order terms. Then the diffusion coefficient vanishes, $D = Z(\omega \rightarrow 0) = 0$, and the VACF inherits a leading non-analytic contribution for $\omega \rightarrow 0$,

$$Z(\omega) \simeq (-i\omega)^{1-\alpha} K_\alpha \Gamma(1 + \alpha), \quad (56)$$

with $K_\alpha \Gamma(1 + \alpha) = \langle \ell^2 \rangle \tau^{-\alpha} / 2d$. By means of a Tauber theorem [53, 59], the non-analyticity at zero frequency corresponds to a negative long-time tail in the VACF,

$$Z(t) \simeq -\alpha(1 - \alpha) K_\alpha t^{\alpha-2}, \quad t \rightarrow \infty. \quad (57)$$

Thus, persistent anticorrelations become manifest in the VACF. Integration over time shows that the time-dependent

diffusion coefficient, $D(t)$, approaches zero at long times only algebraically, $D(t) \simeq \alpha K_\alpha t^{\alpha-1}$ for $t \rightarrow \infty$. Eventually, one finds for the mean-square displacement,

$$\delta r^2(t) \simeq 2dK_\alpha t^\alpha, \quad t \rightarrow \infty, \quad (58)$$

i.e., a subdiffusive increase that persists for arbitrarily long lag times. Reversely, the low-frequency singularity in $\psi(\omega)$ is connected to a power-law tail in the waiting-time distribution,

$$\psi(t) \simeq \frac{\alpha \tau^\alpha}{\Gamma(1-\alpha)} t^{-1-\alpha}, \quad t \rightarrow \infty, \quad (59)$$

such that even the mean waiting time is infinite.

Let us briefly discuss the next higher moment, the mean-quartic displacement. The expansion of the incoherent dynamic structure factor, Eq. (51), in powers of the wavenumber yields the one-sided Fourier transform of the mean-quartic displacement, cf. Eqs. (17) and (52),

$$\int_0^\infty dt e^{i\omega t} \delta r^4(t) = 8d(d+2) \frac{Z(\omega)^2}{(-i\omega)^3} + 2d \frac{\langle \ell^4 \rangle}{\langle \ell^2 \rangle} \frac{Z(\omega)}{(-i\omega)^2}. \quad (60)$$

In particular, the leading low-frequency singularity is again completely governed by the tail of the waiting-time distribution,

$$\int_0^\infty dt e^{i\omega t} \delta r^4(t) \simeq 8d(d+2) K_\alpha^2 \Gamma(1+\alpha)^2 (-i\omega)^{-1-2\alpha}; \quad (61)$$

in particular, the 4th moment of the jump size, $\langle \ell^4 \rangle$, does not enter the leading order. Application of a Tauber theorem [53, 59] yields the asymptotic long-time behaviour,

$$\delta r^4(t) \simeq 8d(d+2) \frac{\Gamma(1+\alpha)^2}{\Gamma(1+2\alpha)} K_\alpha^2 t^{2\alpha}, \quad t \rightarrow \infty. \quad (62)$$

One concludes that for a CTRW with power-law distributed waiting times, the non-gaussian parameter approaches a constant value,

$$\alpha_2(t \rightarrow \infty) = \frac{2\Gamma(1+\alpha)^2}{\Gamma(1+2\alpha)} - 1, \quad (63)$$

irrespective of the jump size distribution $\lambda(\ell)$. The method can be easily extended to higher moments, and one can show that *all* non-gaussian parameters assume non-vanishing long-time limits, with values that depend only on the exponent of subdiffusion, α .

Equations (51) to (53) imply a small-wavenumber approximation of the propagator,

$$P(k, \omega) \simeq \frac{1}{-i\omega + k^2 Z(\omega)}, \quad k \rightarrow 0. \quad (64)$$

Propagators of this form will be referred to as *generalised hydrodynamics approximation*. It allows for an explicit solution

of the spatial inverse Fourier transform; actually, all that needs to be done is to replace the diffusion coefficient D in Eqs. (10) by its frequency-dependent generalisation, $Z(\omega)$. For example in three dimensions, one finds

$$P(\mathbf{r}, \omega) = \frac{1}{4\pi Z(\omega) r} \exp\left(-r \sqrt{\frac{-i\omega}{Z(\omega)}}\right) \quad (d=3). \quad (65)$$

3.2.3. Scaling limit and the fractional Fokker–Planck equation

Let us discuss a simple, possibly the simplest distribution for the waiting time that displays a tail, the Cole–Cole distribution,⁴

$$\psi(\omega) = \frac{1}{1 + (-i\omega\tau)^\alpha}. \quad (66)$$

In the temporal domain, this corresponds to the waiting-time distribution [55, 60]

$$\psi(t) = -\frac{d}{dt} E_\alpha(-(t/\tau)^\alpha), \quad (67)$$

where $E_\alpha(\cdot)$ denotes the Mittag–Leffler function. Inserting in Eq. (53), the velocity autocorrelation function assumes a power law for all frequencies,

$$Z(\omega) = \frac{\langle \ell^2 \rangle}{2d\tau} (-i\omega\tau)^{1-\alpha}, \quad (68)$$

and the corresponding mean-square displacement is subdiffusive for all times, $\delta r^2(t) = 2dK_\alpha t^\alpha$. The non-gaussian parameter can be evaluated exactly,

$$\alpha_2(t) = \frac{2\Gamma(1+\alpha)^2}{\Gamma(1+2\alpha)} - 1 + \frac{d}{d+2} \frac{\langle \ell^4 \rangle}{\langle \ell^2 \rangle^2} \Gamma(1+\alpha) \left(\frac{t}{\tau}\right)^{-\alpha}. \quad (69)$$

Within the generalised hydrodynamics approximation, the Fourier–Laplace transform of the propagator, $P(k, \omega)$, is given by Eq. (64) for long wavelengths, $k \rightarrow 0$. Together with $Z(\omega)$ given by Eq. (68), this form corresponds to the scaling limit [55] after coarse-graining on large length scales and long times. The corresponding propagator in real space and time then is the solution of the so-called fractional Fokker–Planck equation [48], which is the scale-free limit of CTRW [55, 60]. The approach presented here devoids the introduction of fractional derivatives which naturally emerge if the equations of motion are introduced in the temporal domain. We refer the mathematically inclined reader to the excellent review by Metzler and Klafter [48].

⁴ Such a frequency-dependence was introduced empirically and has since been widely used to describe the stretched dielectric response of polymeric liquids and glassforming materials, see Kenneth S. Cole and Robert H. Cole, J. Chem. Phys. **9**, 341 (1941).

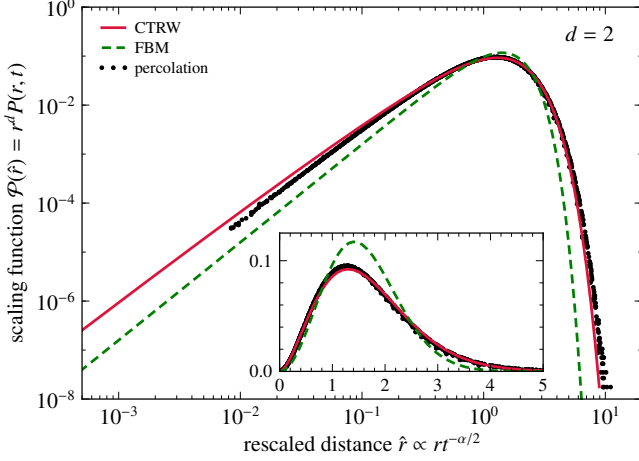


Figure 2. Scaling functions of the propagators for CTRW, fractional Brownian motion (FBM), and lattice percolation on the incipient infinite cluster in $d = 2$ dimensions for subdiffusive motion with $\alpha = 0.695$ on double-logarithmic (main panel) and linear (inset) scales. Scaling functions and scaling variables are normalised such that $\Omega_d \int_0^\infty dx \mathcal{P}(x)/x = 1$ and $\Omega_d \int_0^\infty dx x \mathcal{P}(x) = d$.

The spatial backtransform is obtained from Eq. (9) upon replacing D by the above result for $Z(\omega)$. It is convenient to introduce a dimensionless, rescaled frequency, $\hat{\omega} := (\langle \ell^2 \rangle / 2d)^{-1/\alpha} \tau^{2/\alpha} \omega$. Then,

$$P(\mathbf{r}, \omega) = \frac{(2\pi)^{-d/2}}{-i\omega r^d} (-i\hat{\omega})^{\alpha(d+2)/4} K_{d/2-1}((-i\hat{\omega})^{\alpha/2}). \quad (70)$$

The evaluation of the complex modified Bessel function of the second kind, $K_\nu(\cdot)$, as well as the temporal inverse Fourier transform, Eq. (8), can be achieved numerically, e.g., with MATHEMATICA. In the fractional Fokker–Planck limit, the time- and space-dependent propagator exhibits a scaling property that holds for all times and distances,

$$P(r, t) = r^{-d} \mathcal{P}_\alpha(\hat{r}), \quad \hat{r} \propto r t^{-\alpha/2}; \quad (71)$$

the omitted prefactor, $\langle \ell^2 \rangle^{-1/2} \tau^{\alpha/2}$, renders \hat{r} a dimensionless scaling variable. Although the scaling property is of the same form as for fractional Brownian motion, Eq. (36), the scaling functions are different. Here, \mathcal{P}_α depends on the space dimension d and on the exponent α . The scaling functions are displayed in Figs. 2 and 3 for $d = 2, 3$ and are compared to the scaling functions of fractional Brownian motion and obstructed transport on the percolating cluster for the same subdiffusion exponent. Note that Eq. (70) was derived previously on a lattice [61, Eq. (20)], the subsequent inverse Laplace transform to the time domain, however, relied on asymptotic approximations of the Bessel function, yielding a scaling function, $\mathcal{P}_\alpha(x) = x^d \exp(-x^{2/(2-\alpha)}/2)$ [50, 61], which strongly disagrees with our numerical findings at small arguments.

Since CTRW is not a Markov process, the propagator $P(\mathbf{r}, t)$ does not characterise the dynamics completely. Higher

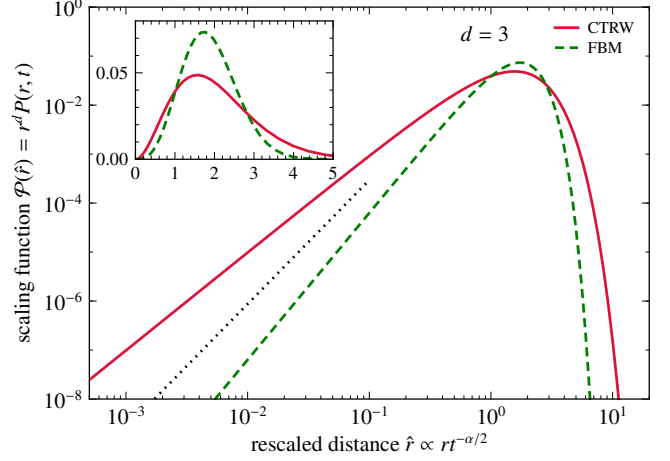


Figure 3. Scaling functions of the propagators for CTRW and fractional Brownian motion in $d = 3$ dimensions for subdiffusive motion with $\alpha = 0.515$ on double logarithmic (main panel) and linear (inset) scales. The dotted, black line indicates the anticipated asymptote for transport on the percolating cluster, $\mathcal{P}_\infty(\hat{r}) \sim \hat{r}^{d_t}$.

correlation functions involving multiple times have been calculated [62] and the procedure has been generalised to arbitrary order [63]. In the fractional Fokker–Planck limit, the dynamics can be written as a subordinated Brownian motion, i.e., the individual trajectories have the very same shape as for Brownian motion, yet the time the particle needs to follow these trajectories is provided by a different clock [64]. Hence to distinguish the CTRW model, respectively the fractional Fokker–Planck description, from fractional Brownian motion, one can use the statistical properties of the individual trajectories and derive suitable measures highlighting the difference, see e.g. Refs. 65–67.

The propagator describes the probability for a tracer to have moved a distance \mathbf{r} after a lag time t . If the stochastic process is in equilibrium this ensemble average can be obtained also as a moving-time average, i.e., by following a single trajectory of a tracer. For CTRW such that the mean waiting is strictly infinite, the process never reaches equilibrium, no matter how remote the process has been initiated in the past [53, 68–70]. Then, time correlation functions exhibit *ageing*, i.e., they explicitly depend on the points in time of the measurements and not just the time lag inbetween. A closely related phenomenon is referred to as weak ergodicity breaking and was introduced by Bouchaud [71] in the context of spin glasses. The reason is at the very heart of the concept of CTRW with power-law distributed waiting times, since as time proceeds, longer and longer waiting times are drawn from the distribution before the particle actually moves. In consequence, individual trajectories can differ strongly from the average, or in other words, the average is not dominated by the *typical* realisations of the trajectories. Hence, one has to be

careful when comparing predictions for individual trajectories to ensemble averages and one should calculate probabilities for the time averages of observable quantities [72–76].

3.3. Obstructed motion: Lorentz models

The models discussed so far implicitly assume that the particle motion occurs in a homogeneous medium; for example, the waiting time in a CTRW does not depend on the position. In contrast, the Lorentz model paradigmatically describes transport in a spatially heterogeneous medium and displays many facets of anomalous transport like subdiffusion, crossover phenomena, immobilised particles, and long-time tails. In the original version, H. A. Lorentz [77] discussed the motion of a ballistic particle which is elastically scattered off randomly placed, hard spherical obstacles to lay a microscopic basis for Drude’s electric conductivity of metals. The medium is reminiscent of a Swiss cheese: it consists of a homogeneous phase supporting free particle transport, punched by the possibly overlapping obstacles. Thus at high obstacle density, a tracer faces a heterogeneous environment characterised by a significant excluded volume and a highly ramified remaining space. Variants of the model include Brownian tracer particles [22, 78–80] or correlated obstacles, e.g., by simply forbidding obstacle overlaps [78, 81–86]. Saxton [87] and later Sung and Yethiraj [83, 84] recognised the biophysical relevance of such obstacle models for protein transport in cellular membranes.

The model is described by a number of parameters. The obstacle radius σ fixes the unit of length, and the unit of time τ is specified in terms of the velocity v of a ballistic tracer or the microscopic diffusion constant D_0 in case of a Brownian tracer. Then, the dimensionless obstacle density, $n^* = n\sigma^3$, remains as the only interesting control parameter; n is the number of obstacles per volume. Alternatively, one may use the porosity or fraction of unoccupied, void volume, e.g., $\varphi = \exp(-nv)$ for independently inserted obstacles of volume v .

3.3.1. Microscopic theories

The ballistic motion of the tracer is randomised by the scattering and becomes diffusive at long times. Assuming uncorrelated collisions, Lorentz [77] computed the diffusion coefficient about a century ago to $D_0 = v\sigma/3\pi n^*$ for $d = 3$; for $d = 2$, Lorentz–Boltzmann theory yields $D_0 = 3v\sigma/16n^*$ [88]. These results are valid only in the dilute limit, $n^* \rightarrow 0$. Actually, subsequent collisions with the obstacles are persistently correlated due to the frozen disorder, and a proper treatment involves the resummation of so-called ring collisions. A systematic low-density expansion of $1/D$ within kinetic theory [88, 89] revealed non-analytic terms at the leading ($d = 2$) or next-to-leading ($d = 3$) order, supported by pioneering computer simulations [90, 91]. For a Brownian tracer, the short-

time motion is diffusive already by construction and the long-time tail of the VACF is obtained at leading order in a low-density expansion [80], employing a scattering formalism for the Smoluchowski operator.

The microscopic theoretical treatment beyond the regime of low densities could be extended using self-consistent approximations. Götze *et al.* [92, 93, 94] closed the Zwanzig–Mori equations for the incoherent dynamic structure factor by introducing a set of approximations for the frequency-dependent memory kernel; an approach that formed the basis of the successful microscopic mode-coupling theory for the description of the glass transition [21]. For the Lorentz model, the theory predicts a localisation transition, i.e., a critical obstacle density n_c^* , where long-range transport ceases, $D(n^*) = 0$ for $n^* \geq n_c^*$. As the critical density is approached, a temporal window emerges with a subdiffusive increase of the mean-square displacement; concomitantly, the long-time diffusion constant is predicted to vanish according to a power law, $D(n^*) \sim |n^* - n_c^*|^\mu$ for $n^* \uparrow n_c^*$. A similar picture was obtained within a self-consistent repeated-ring kinetic theory [95], although both theories have deficiencies and differ in their detailed predictions.

Recently, transport of a dense fluid in a porous host structure has attracted new interest. Significant progress in this direction has been achieved by Krakoviack [96, 97, 98] by generalising the mode-coupling theory of the glass transition. There, a series of non-equilibrium phase transitions was predicted, which roughly speaking correspond to glass-glass transitions in size-disparate mixtures [99]. Some of the predicted phenomena have already been observed in computer simulations [100–103]. In the limit of small fluid density, the model degenerates to the Lorentz model and the physics should be dominated by long-wavelength phenomena [104]; however, these features appear not to be correctly reproduced by the current theories. A theoretical framework combining all aspects of glassy dynamics and localisation is yet to be developed.

3.3.2. Percolation and random-resistor networks

A phenomenological approach to the transport properties of the Lorentz model relies on a mapping to random-resistor networks. The medium is thought of as a set of voids connected by channels, and transport occurs via hopping from void to void. The geometry of the channels, formed by close by obstacles, imposes a distribution of transition probabilities between the voids. For many voids, although being neighbours in space, a direct connection is blocked by obstacles and the transition probability is zero. The anticipated link to random-resistor networks is provided by representing the voids as the nodes of a regular lattice and interpreting the transition probabilities as electric conductances between lattice nodes. The macroscopic diffusion constant is then identified as the total conductance of the network. For a given obstacle configuration, the network may be constructed rigorously from

a Voronoi tessellation [83, 84, 105, 106]. Increasing the obstacle densities corresponds to diluting the conductive bonds of the network, precisely as in the bond percolation problem [50, 107]. If the bonds are sufficiently diluted, the network falls apart into differently sized clusters, and above a critical threshold and in the thermodynamic limit, no spanning cluster exists that supports macroscopic transport.

Let us briefly summarise the essence of percolation theory; we refer the reader to the excellent textbooks by ben Avraham and Havlin [50] and Stauffer and Aharony [107] for a profound introduction. Directly at the percolation transition, the incipient infinite cluster is a fractal in a statistical sense. It is of inextensive weight and occupies a volume $s_\infty(L) \sim L^{d_f}$ within a ball of radius L , defining the fractal dimension, $d_f < d$. A self-similar hierarchy of finite clusters coexists with the infinite cluster, whereby the distribution of cluster sizes s follows a power law, s^{-1-d/d_f} . Away from the transition, the medium is no longer scale-free and self-similarity holds only on length scales below the correlation length, ξ . In particular, the probability to encounter finite clusters of linear extent larger than ξ is at least exponentially suppressed. On the percolating side of the transition, the infinite cluster looks homogeneous at scales larger than ξ . The correlation length exhibits a non-analytic singularity at the transition in form of a power-law divergence, $\xi \sim |n^* - n_c^*|^{-\nu}$, which introduces a second critical exponent, ν . The macroscopic conductivity Σ of a percolating random-resistor network vanishes at the percolation threshold with a power-law singularity as well, $\Sigma \sim |n^* - n_c^*|^\mu$. The conductivity exponent μ constitutes a third critical exponent, which describes transport and dynamic phenomena and genuinely extends the set of geometric exponents (d_f, ν); in general, it does not follow by means of a scaling relation from the other two.

The percolation transition shares many aspects of a continuous thermodynamic phase transition and is tractable by renormalisation group methods [107, 108]. An important lesson is that the critical exponents d_f , ν , and μ are determined by a non-trivial fixed point of the renormalisation group flow, i.e., a systematic and consistent coarse-graining of the medium. As a consequence, the microscopic details of a specific model become irrelevant for the leading singular behaviour near the transition, and in this sense, the critical exponents are universal numbers. The percolation transitions of many different lattice types belong to a single universality class and are characterised by the same set of exponents, which depends only on the dimension of space. A compilation of recent values for the critical exponents of random percolation is given in Table I.

For transport on continuum percolation clusters, a peculiarity arises: the dynamic universality class may be different from that of lattice models. In the context of random-resistor networks it was shown that a sufficiently singular power-law distribution of weak bond conductances, $\Pi_\sigma(\sigma_{\text{bond}}) \sim \sigma_{\text{bond}}^{-a}$ for $\sigma_{\text{bond}} \rightarrow 0$, can dominate the renormalisation flow such

d	2	3	
d_f	91/48 ^a	2.530(4) ^c	
ν	4/3 ^a	0.875(1) ^d	
Ω	72/91 ^b	0.64(2) ^d	
		lattice	continuum
d_w	2.878(1) ^a	3.88(3) ^a	4.81(2) ^e
z	3.036(1)	5.07(6)	6.30(3)
y	0.5212(2)	0.42(2)	0.34(2)

Table I. Static and dynamic percolation exponents for the leading and sub-leading critical behaviour. Numbers in parentheses indicate the uncertainty in the last digit. Sources: (a) Ref. 109, (b) Refs. 110 and 111, (c) from exponent $\tau = 1 + d/d_f = 2.186(2)$ [112], (d) Ref. 113, (e) continuum percolation theory yields $d_w = d_f + 2/\nu$ for a ballistic tracer [79, 114, 115]. The values for y and z were calculated from exponent relations, $yd_w = \Omega d_f$ [116] and $z = 2d_w/(2+d_f-d)$ [50]. The dynamic universality class does not split for $d = 2$ [114, 117, 118].

that the conductivity exponent μ deviates from its universal value on lattices, $\mu = \max\{\mu^{\text{lat}}, \nu(d-2) + 1/(1-a)\}$ [119–121]. In continuum percolation, the weak conductances arise from narrow gaps or channels connecting the voids. For uncorrelated spheres or discs, indeed a power-law distribution was derived, which is singular enough in three dimensions to modify the exponent; the chain of arguments has been summarised in Ref. 79. Halperin *et al.* [117] predicted $\mu = \nu + 3/2$ for the conductivity problem, and Machta *et al.* [120] found $\mu = \nu + 2$ for the diffusion constant of ballistic tracers.

The structural aspects of the Lorentz model with overlapping obstacles have been studied extensively in the context of continuum percolation. It shares the phenomenology of lattice percolation, and simulation results are consistently described by the same universality class [79, 106], even for obstacle mixtures with two different radii [122, 123]. In the light of renormalisation group theory, this is no surprise and corroborates the mapping to random-resistor networks. Percolation thresholds were obtained with high precision yielding a critical void porosity $\varphi_c = 0.0301(3)$ for spheres [106, 122, 123] and $\varphi_c = 0.323\,652\,5(6)$ for discs [124, 125]; numbers in parentheses indicate the uncertainty in the last digit. Simulations for the Lorentz model [22, 79, 115, 118, 126, 127] confirm the picture that the localisation transition is indeed driven by the percolation transition of the medium. For point tracers, the critical density of the localisation transition is defined by the percolation threshold. The critical porosity for localisation of a tracer with finite radius σ_t follows trivially in the case of hard obstacles as $\varphi_c(\sigma_t) = \exp(-n_c^*(\sigma_t + \sigma)^{-d\nu})$, e.g., the localisation transition occurs at a void porosity of $\varphi_c(\sigma_t = \sigma) = \varphi_c^{1/8} \approx 65\%$ for tracer and obstacles being spheres of the same size. A similarly high sensitivity of the percolation threshold to the tracer radius was found numerically for obstacles modelled by soft repulsive discs [128].

3.3.3. The ant in the labyrinth

Consider a random walker (“the ant”) on percolation clusters that has to explore the ramified and self-similar structure of the clusters (“the labyrinth”). The problem was posed by de Gennes [129] and is amenable to scaling arguments [129–132] corroborated by Monte-Carlo simulations [133]. If the walker is restricted to the incipient infinite cluster at criticality, one expects subdiffusive motion, $\delta r_\infty^2(t) \sim t^{2/d_w}$, at all time scales beyond the microscopic regime, $t \gg \tau := \sigma^2/D_0$. The exponent d_w is known as walk dimension and one may prefer to consider it the fundamental critical exponent for the dynamics rather than the conductivity exponent, μ . Off criticality, where the infinite cluster becomes homogeneous on distances much larger than ξ , tracer transport crosses over to normal diffusion, $\delta r_\infty^2(t) \simeq 2dD_\infty t$, at long times, $t \gg t_x$. The crossover time scale may be defined via $\delta r_\infty^2(t_x) = \xi^2$ and diverges as $t_x \sim \xi^{d_w}$. Crossover matching yields $t_x^{2/d_w} \sim D_\infty t_x$, which implies that the macroscopic diffusion constant vanishes at the critical density in a singular way, $D_\infty(n^*) \sim |n^* - n_c^*|^{\mu_\infty}$, where $\mu_\infty = \nu(d_w - 2)$. Transport on a finite cluster is subdiffusive as well with the same exponent $2/d_w$ as long as the tracer has not fully explored the cluster [116, 132].

If tracers on all clusters are included, the dynamics is non-ergodic since the time average over a single trajectory differs from an ensemble average. The average over a self-similar hierarchy of differently sized clusters reduces the exponent of subdiffusion, $\delta r^2(t) \sim t^{2/z}$ for $\tau \ll t \ll t_x$, with the dynamic exponent z given by $z = d_w/[1 - (d - d_f)/2] > d_w$. In the absence of a percolating cluster, the mean-square displacement saturates for long times, $\delta r^2(t) \simeq \ell^2$ for $t \gg t_x$, and measures the mean-cluster size, $\ell \sim t_x^{1/z} \sim \xi^{1-(d-d_f)/2}$, which is distinct from the size of the largest finite clusters, ξ . At the percolating side of the transition, the mean-square displacements for an all-cluster average increase linearly for long times, $\delta r^2(t) \simeq 2dDt$ for $t \gg t_x$. We shall refer to this behaviour also as *heterogeneous diffusion* although only the motion on the infinite cluster is diffusive, the all-cluster averaged propagator being different from a gaussian even for long times. Since the finite clusters do not contribute, the diffusion constant is further suppressed by the small weight of the infinite cluster yielding $D(n^*) \sim |n^* - n_c^*|^\mu$ with $\mu = \nu(d_w - 2 + d - d_f)$ for the all-cluster-averaged motion. By virtue of an Einstein relation, $\Sigma \sim D$, the exponent μ corresponds to the conductivity exponent. The previous relation connecting μ and d_w emphasises that the leading singularities of transport-related observables can be described by a single exponent, e.g., the walk dimension, d_w .

The dynamic scaling hypothesis [134] suggests that the full time-dependence in the scaling limit is encoded in universal scaling functions, which extends the notion of universality for the critical exponents. More specifically, a scaling form of the mean-square displacement is expected to hold at sufficiently

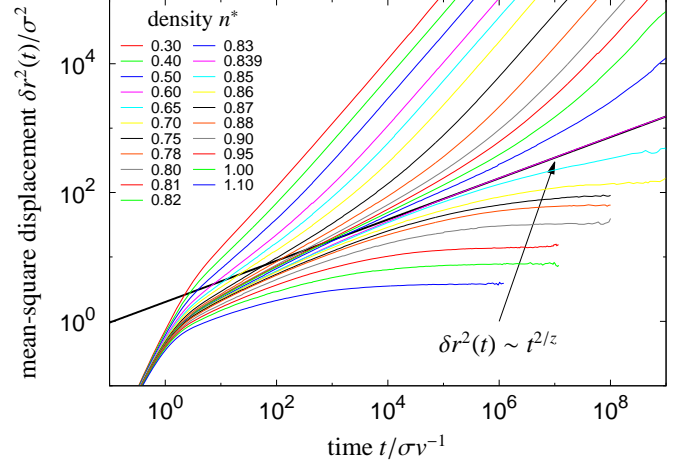


Figure 4. Ensemble-averaged mean-square displacements for different obstacle densities in the three-dimensional Lorentz model with a ballistic point tracer. Data taken from Ref. 115.

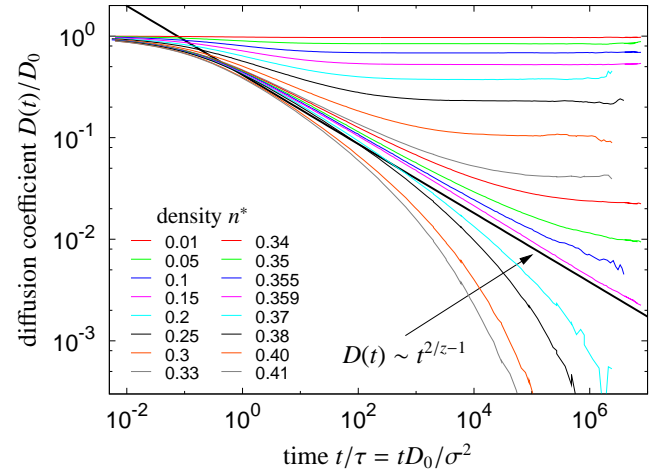


Figure 5. Time-dependent, ensemble-averaged diffusion coefficients for different obstacle densities in the two-dimensional Lorentz model with a Brownian point tracer. Data taken from Ref. 22.

long times, $t \gg \tau$,

$$\delta r^2(t; n^*) = t^{2/z} \delta \mathcal{R}_\pm^2(\hat{t}), \quad \hat{t} := t/t_x \sim t\ell^{-z}; \quad (72)$$

$\delta \mathcal{R}_-^2$ and $\delta \mathcal{R}_+^2$ denote scaling functions which describe the crossovers from subdiffusion to heterogeneous diffusion or localisation, respectively. They approach the same constant for small arguments, and the correct long-time behaviour of $\delta r^2(t)$ is reproduced by $\delta \mathcal{R}_-^2(\hat{t}) \sim \hat{t}^{1-2/z}$ and $\delta \mathcal{R}_+^2(\hat{t}) \sim \hat{t}^{-2/z}$ for $\hat{t} \rightarrow \infty$. Numerical results for these functions can be found in Refs. 22 and 116 for $d = 2$ and in Ref. 115 for the Lorentz model in $d = 3$. The crossover from intermediate subdiffusion to the long-time behaviour occurs slowly and extends over several decades in time.

3.3.4. Simulation results

The ensemble-averaged mean-square displacements of a ballistic tracer in the three-dimensional Lorentz model were determined by computer simulations over the full range of obstacle densities [115], reproduced in Fig. 4. A temporal window of subdiffusive motion emerges as the critical obstacle density is approached, and at the critical density, subdiffusion is observed over 6 decades in time. The subdiffusion exponent has been determined as $\alpha = 2/z \approx 0.32$ and is consistent with the predictions for continuum percolation, $\mu = \nu + 2 \approx 2.88$ [120]. Likewise, a tracer on the incipient infinite cluster obeys subdiffusion with $2/d_w \approx 0.42$ [127]. Away from criticality, the subdiffusive motion crosses over to either heterogeneous diffusion or localisation beyond the time scale t_x . If particles on all clusters are considered, the non-gaussian parameter slowly diverges in time, $\alpha_2(t) \sim t^{(d-d_c)/d_w}$, reflecting the distinct length scales ℓ and ξ [79, 115]; it approaches a constant for tracers only on the infinite cluster [127].

The same phenomenology was found within simulations for the two-dimensional Lorentz model with a Brownian point tracer [22] and earlier for an obstructed random walker on a percolating square lattice [87]. The time-dependent diffusion coefficient, $D(t) = \partial_t \delta r^2(t)/4$, in Fig. 5 nicely exhibits a double-crossover scenario from free diffusion at microscopic time scales to a growing subdiffusive window, $\tau \ll t \ll t_x$, and back to heterogeneous diffusion with a suppressed diffusion constant for long times,

$$D(t) \approx \begin{cases} 4D_0 t, & t \ll \tau, \\ \alpha K_\alpha t^{\alpha-1}, & \tau \ll t \ll t_x, \\ 4Dt, & t \gg t_x; \end{cases} \quad (73)$$

the data are consistent with the exponent $\alpha = 2/z \approx 0.659$ from lattice percolation in two dimensions.

In the context of ion conductors, the electric conductivity and susceptibility are relevant material parameters. Simulation data for the Lorentz model reveal an anomalous frequency-dependence inherited from the time-dependent diffusion coefficient, $D(t)$, by a Fourier–Laplace transform [126, 127, 132].

Closer inspection of Fig. 4 suggests an apparent density dependence of the subdiffusive motion, which contrasts the notion of one universal exponent governing the subdiffusive regime and which seems to violate scaling, Eq. (72). The discrepancy is resolved by noting that the scaling property only holds asymptotically and that correction terms arise if the time scales under considerations are not large enough. It was argued that the leading correction term is non-analytic and well approximated by a power law, $\delta r^2(t; n^*) = t^{2/z} \delta \mathcal{R}_\pm^2(\hat{t})(1 + Ct^{-y})$, where C is a non-universal constant [115]. The correction exponent y , on the other hand, is universal and related to the correction of the cluster-size distribution at criticality, $P(s; n_c^*) \sim s^{-1-d/d_c}(1 + \tilde{C}s^{-\Omega})$ for $s \rightarrow \infty$. The exponent relation $y d_w = \Omega d_f$ was derived within a cluster-resolved scal-

ing theory for transport on percolation clusters [116]. If corrections of this form are taken into account, the scaling property, Eq. (72), is corroborated by extensive simulation data for two- and three-dimensional Lorentz models [22, 79, 115, 127]. Both, significant corrections to scaling and slow crossovers imply that a power-law fit to experimental data over a limited time window is likely to produce apparent subdiffusion exponents that deviate from the universal value. Further, deviations from the idealisation of hard, immobile obstacles potentially wash out the sharp localisation transition.

The mean-square displacement obtained in the computer simulations are ensemble averages where the initial position of the tracers have been chosen according to their equilibrium distribution, i.e., anywhere in the void space. Furthermore, an average over different realisations of the disordered environment is performed to ensure that all sample-to-sample fluctuations are averaged out. Nevertheless, it would be interesting to investigate the convergence of the averaging procedure. If the tracer is confined to the infinite cluster only, one should measure how long single trajectories have to be in order that the time-averaged mean-square displacement reflects the ensemble-averaged counterpart.

3.3.5. Spatially resolved transport

The scaling form of the propagator is more involved than for the models discussed so far due to the presence of finite clusters and the finite correlation length. For transport restricted to the infinite cluster, one expects [116, 135]

$$P_\infty(r, t; n^*) = \xi^{-d} \mathcal{P}_\infty(r/\xi, t\xi^{-d_w}) \quad (74)$$

in the scaling limit, $r, \xi \gg \sigma$ and $t \gg \tau$; the density dependence is encoded on the r.h.s. via the divergent correlation length, $\xi \sim |n^* - n_c^*|^{-\nu}$. At the critical density, this simplifies to the one-parameter scaling form familiar from the preceding sections,

$$P_\infty(r, t; n_c^*) = r^{-d} \tilde{\mathcal{P}}_\infty(rt^{-1/d_w}). \quad (75)$$

We have determined the scaling function $\tilde{\mathcal{P}}_\infty(\cdot)$ for a random walker on the incipient infinite cluster of a square lattice (site percolation) using Monte-Carlo simulations, see Fig. 2. For small arguments, the fractal dimension enters the scaling function, $\tilde{\mathcal{P}}_\infty(x) \sim x^{d_f}$ for $x \ll 1$, with consequences for the return probability, which is effectively probed in fluorescence correlation spectroscopy [23]. The scaling of the intermediate scattering function was studied numerically [136] and it was found that certain aspects are surprisingly well predicted by a mode-coupling approach.

For transport phenomena including all clusters, a dynamic scaling ansatz for the van Hove function has been conjectured [115, 135],

$$P(r, t; n^*) = \xi^{d_f - 2d} \mathcal{P}_\pm(r/\xi, t\xi^{-d_w}); \quad (76)$$

the modified prefactor follows from averaging over the cluster size distribution [116] and the index \pm indicates either the localised phase (+) or the regime of heterogeneous diffusion (-). The scaling form has implications for the mean-square displacement, Eq. (72), and the non-gaussian parameter, both of which were corroborated by extensive simulations [22, 79, 115, 133].

A fraction of particles is generically trapped or “immobile” at long time scales by the presence of finite clusters at all obstacle densities. Immobile particles become manifest for all n^* in a finite Lamb-Möbbsauer factor or non-ergodicity parameter [135],

$$f(k; n^*) := \lim_{t \rightarrow \infty} P(k, t) > 0, \quad (77)$$

in agreement with simulations [126, 137]. The long-wavelength limit, $\lim_{k \rightarrow 0} f(k)$, quantifies the immobile fraction and displays a singularity at the percolation transition [135]; more generally, a scaling form has been suggested [126],

$$1 - f(k; n^*) = \xi^{d_i - d} \mathcal{F}_{\pm}(k\xi) \quad (78)$$

for small wavenumbers, $k \ll 2\pi/\sigma$, and close to the transition, $\xi \gg \sigma$; the asymptotics of the scaling functions are $\mathcal{F}_-(x \rightarrow 0) = \text{const}$, $\mathcal{F}_+(x \rightarrow 0) = 0$, and $\mathcal{F}_{\pm}(x) \sim x^{d-d_i}$ for $x \gg 1$.

3.3.6. Velocity autocorrelation function

The obstacles impose an excluded volume on the tracer particles, which forces the latter to reverse the direction of motion at some point. As a result, the particle displacements carry persistent anticorrelations which become manifest in an algebraic long-time tail of the VACF, $-Z(t) \sim t^{-d/2-1}$, first derived within kinetic theory for low obstacle density [89]. More generally, the power-law decay at long times emerges for diffusion in a frozen, disordered environment [138, 139], and it is already produced by repeated encounters of a Brownian tracer with a single obstacle [80], or equivalently, two colloidal particles [140]. The phenomenon is universal and occurs independently of the obstacle density with the same exponent at sufficiently long time scales; close to the localisation transition, the long-time tail competes with an intermediate, critical power law inherited from the subdiffusive motion [92]. These predictions were confirmed by simulations on a lattice [141] and in the continuum [22, 118]. Molecular dynamics simulations for supercooled mixtures of hard spheres [142, 143] and Lennard-Jones particles [144], both exhibiting slow glassy dynamics, reveal the same power-law signature in the VACF, which indicates that the underlying mechanism may also apply for glassforming materials. A related long-time tail was predicted within a mode-coupling theory for the force-force correlation function in dense colloidal suspensions [145].

In the localised regime, $n^* > n_c^*$, where diffusive transport is absent, Machta [146] argued that another long-time tail becomes dominant if there are cul-de-sacs with a broad distribution of exit rates. The singular distribution of channel

width in the overlapping Lorentz model implies a long-time tail, $-Z(t) \sim t^{-[2+1/(d-1)]}$, for a ballistic tracer [114], which has been detected in recent simulations [118].

3.4. Other sources of subdiffusion

To conclude the section, let us mention further examples of mechanisms, which are known to lead to subdiffusion. The review by Bouchaud and Georges [49] introduces a series of lattice models with quenched disorder, for example random trap and random barrier models or comb-like structures, which under certain conditions yield subdiffusive transport. Next, single-file diffusion describes the motion of strongly interacting particles aligned in a tube-like structure such that the excluded volume impedes passing. As a consequence, the mean-square displacement grows as $\delta r^2(t) \sim t^{1/2}$ [147–149].

For flexible polymers, the chain connectivity induces strongly correlated motion between the individual chain segments. Transport slows down as the polymer weight increases. For intermediate time scales, a labelled monomer displays a subdiffusive mean-square displacement until the slowest Rouse mode has relaxed [150–153]. Self-avoidance due to excluded volume and entanglement effects from topological constraints add to the complexity of the dynamics. The theoretical implications from the interplay of polymer physics and crowding (excluded volume) remain largely unexplored to this date.

Apparent subdiffusion may result from incorporating several processes that occur on different time scales, for example in multi-component mixtures, due to a polymeric depletion layer around tracers [154, 155], or due to internal states. In these cases, the processes are intrinsic to the constituents or their interactions and hence cover finite time windows only. In particular, one can usually not manipulate these processes to generate a self-similar distribution of time scales required for anomalous transport in the sense of Section 2.2.

4. Experimental techniques

Before we will review the biophysical experiments addressing anomalous transport, let us introduce some widespread experimental techniques that have been developed during the past decades and that have proved themselves as useful tools for the measurement of molecular transport in mesoscopic samples.

4.1. Single-particle tracking

An important technique that is both intuitive and powerful is provided by single-particle tracking, for reviews in the context of biophysics see Refs. 19 (giving an extensive historical account in the supplement) and 156. Here, a nanoscopic reporter particle or a fluorescent dye is introduced in the probe and followed by confocal video microscopy and digital image

processing. The trajectory is recorded over sufficiently long time, which provides direct access to the full statistics of the spatial displacements and which, in principle, allows for the evaluation of all correlation functions. The most widely used quantity is, of course, the mean-square displacement as it is rather robust with respect to experimental noise and appears easy to interpret.

The spatial resolution of the displacements is typically on the order of a few nanometres, while the temporal resolution is limited by the image capture rate to about 10 ms [156]. High-speed tracking with a resolution of 25 μ s could be implemented by using colloidal gold nanoparticles as tracers, which yielded a sufficiently high signal-to-noise ratio [19]. The length of the recorded trajectories and thus the longest accessible time scale is limited by photobleaching of the fluorophores and by residual drifts of the sample baseline. Single-particle tracking is well suited to study transport in cellular membranes and to elucidate their structural details [19, 157]. Limitations occur for tracking inside the cytoplasm since the spatial resolution transverse to the focal plane is naturally an order of magnitude lower [158]; progress was made recently using tailored computer algorithms that address the noise and image inhomogeneities specific to the cytoplasm [159]. Single-particle tracking has also become a widespread tool to probe the microrheology of the cytoplasm, see Refs. 160–162 for recent reviews and references therein.

Three-dimensional tracking at the nanoscale has seen significant advances recently. Truly three-dimensional trajectories in real-time at a resolution of 32 ms are provided by orbital tracking of a single particle, which relies on a feed-back loop coupled to the laser-scanning microscope [163]. The “blindness” of this technique to the neighbourhood is overcome by simultaneous wide-field imaging, which is particularly useful to track particles with nanometre resolution in a heterogeneous environment [164]. Off-focus imaging of trapped particles provides even subnanometre resolution in all three directions; it requires, however, information about the optical properties of the sample [165]. An alternative to strongly trapped probes is interferometric detection, where the motion can be resolved with sub-Ångström resolution at 75 MHz [166], yielding significant time-correlation functions over 4 decades in time [40, 46].

Central for the analysis of single-particle tracking experiments is the evaluation of time-correlation functions as they contain the proper statistical description of the motion, see Section 2.2. The mere inspection of individual stochastic trajectories may easily lead to misinterpretations [157, 167]. The discussion and computation of time-correlation functions and related quantities is simplified in the case of time-translational invariance, i.e., for samples in equilibrium or in a steady state. Then, the correlation functions depend on the lag time only and provide information about the motion at a certain time scale (and not at a certain point in time); they are naturally

displayed on a logarithmic time axis. For example, the mean-square displacement of a single trajectory $x(t)$ of finite length T given on an equidistant time grid is efficiently evaluated as a time average employing a fast (discrete) Fourier transformation \mathcal{F} ,

$$C_{xx}(t; T) := \langle x(t) x(0) \rangle_T = \frac{1}{T} \int_0^T x(t' + t) x(t') dt' \quad (79)$$

$$= \mathcal{F}_t^{-1} \left[\frac{1}{T} |\mathcal{F}_\omega[x(t)]|^2 \right] \quad (80)$$

$$= \frac{1}{T} \sum_{n \in \mathbb{Z}} \frac{1}{T} |x_T(\omega_n)|^2 \cos(\omega_n t), \quad (81)$$

where $\omega_n = 2\pi n/T$ and

$$x_T(\omega) := \mathcal{F}_\omega[x(t)] = \int_{-T/2}^{T/2} x(t) e^{-i\omega t} dt; \quad (82)$$

the mean-square displacement then follows as $\delta x^2(t) = 2[C_{xx}(0; T) - C_{xx}(t; T)]$ for $t \ll T$. For very long trajectories, a semi-logarithmic sampling of the trajectory data and a direct evaluation of the correlations has proved a useful alternative [168].

Automated experimental assays can measure several thousand trajectories and thus permit the evaluation of displacement histograms, i.e., the propagator $P(r, t)$, or of the squared displacements, see Section 2.2.2. Analysis of these distributions helps to disentangle different transport processes, for example in mixtures of slow and fast particles [169, 170] or when stationary and non-stationary processes coexist [171]. Second, the propagator gives insight into the spatial aspects of a transport process that would remain undisclosed by a mere investigation of the mean-square displacement, as has been discussed extensively in Section 3. For example, tracking experiments demonstrated that transport characterised by a diffusive mean-square displacement may be non-gaussian in space [172]. Finally, the ensemble of time-averaged mean-square displacements may display large fluctuations, in particular if transport is anomalous. Comparison of ensemble and time averages tests the ergodic hypothesis and may shed light on the underlying processes in nanoporous structures [173, 174] as well as in cellular membranes [171].

4.2. Fluorescence correlation spectroscopy (FCS)

A second powerful technique that has been widely applied in the biophysical context is fluorescence correlation spectroscopy (FCS). Here the basic idea is to label few molecules by a fluorescent dye and record the fluctuating fluorescent light upon illuminating a small part of the sample. We briefly introduce the theory underlying the measurement and discuss how anomalous transport manifests itself in the corresponding correlation function, comprehensive information about the advantages and limitations of FCS may be found in the pertinent

literature, for reviews see Refs. 175–179. Compared to single-particle tracking, an advantage of FCS is the high temporal resolution in the microsecond regime and the use of tracers as small as a single fluorophore. On the other hand, the spatial sensitivity is typically on the order of some 100 nm (exceptions are discussed below), orders of magnitude larger than that of high-precision tracking experiments.

A typical FCS setup consists of an illumination laser and a confocal microscope with a photon detector.⁵ The laser beam illuminates the detection volume with the intensity profile $W(\mathbf{r})$ and excites the fluorophores in the focal volume. The emitted fluorescent light is collected in the detector, it depends on the fluctuating, local concentration $c(\mathbf{r}, t)$ of labelled molecules. Thus, the detected light intensity is a spatially weighted average [Ref. 14, section 6.6],

$$I(t) = \varepsilon \int d^d r W(\mathbf{r}) c(\mathbf{r}, t), \quad (83)$$

where the prefactor ε accounts for the total quantum efficiency of absorption, fluorescence, and detection. The output of the FCS experiment is the time-autocorrelation function $G(t)$ of the intensity fluctuation $\delta I(t) = I(t) - \langle I \rangle$ around the mean intensity; it is conventionally normalised as

$$G(t) = \langle \delta I(t) \delta I(0) \rangle / \langle I \rangle^2. \quad (84)$$

Introducing a spatial Fourier transform, $W(\mathbf{k}) := \int d^d r e^{i\mathbf{k}\cdot\mathbf{r}} W(\mathbf{r})$, and the intermediate scattering function,

$$S(\mathbf{k}, t) := \frac{1}{\langle c \rangle} \int d^d r e^{-i\mathbf{k}\cdot\mathbf{r}} \langle \delta c(\mathbf{r}, t) \delta c(\mathbf{0}, 0) \rangle, \quad (85)$$

one arrives at the expression

$$G(t) = \frac{1}{N} \frac{\int d^d k |W(\mathbf{k})|^2 S(\mathbf{k}, t)}{\int d^d k |W(\mathbf{k})|^2}, \quad (86)$$

where $N := \langle I \rangle^2 / \langle \delta I^2 \rangle = \langle c \rangle V_{\text{eff}}$ is interpreted as the number of fluorophores in the effective illumination volume V_{eff} . In the experiments, the fluorophores are highly diluted and V_{eff} usually contains only few molecules or even less than 1, turning FCS essentially into a single-molecule fluorescence technique [178]. Thus, $S(\mathbf{k}, t)$ reduces to the *incoherent* intermediate scattering function,

$$S(\mathbf{k}, t) \simeq P(\mathbf{k}, t) = \langle e^{-i\mathbf{k}\cdot\Delta\mathbf{R}(t)} \rangle. \quad (87)$$

Inserting this in Eq. (86) and interchanging the \mathbf{k} -integration and the statistical average provides the fundamental expression for the FCS correlation function [23],

$$G(t) \propto \left\langle \int d^d k |W(\mathbf{k})|^2 e^{-i\mathbf{k}\cdot\Delta\mathbf{R}(t)} \right\rangle. \quad (88)$$

⁵ In practice, the detector consists of two cross-correlated avalanche photodiodes to reduce the detector noise.

It depends solely on the approximation of dilute labelling, it holds for arbitrary illumination profile and makes no assumptions on the fluorophore transport.

For practical purposes, however, Eq. (88) shall be evaluated further. A conventional laser emits a gaussian beam profile, which together with the usual confocal setup leads to an illumination profile that is often approximated by an elongated ellipsoid,

$$W(\mathbf{r}) \propto \exp\left(-2(x^2 + y^2)/w^2 - 2z^2/z_0^2\right) \quad (89)$$

with beam waist w and longitudinal extension z_0 . This implies a gaussian filter function, $|W(\mathbf{k})|^2 \propto \exp\left(-(k_x^2 + k_y^2 + \eta^2 k_z^2)w^2/4\right)$, introducing the anisotropy parameter $\eta = z_0/w$. Then, the \mathbf{k} -integration can be carried out and gives

$$G(t; w) = \frac{1}{N} \left\langle \exp\left(-\frac{\Delta\mathbf{R}(t)^2}{w^2} + \frac{1 - \eta^2}{w^2} \Delta Z(t)^2\right) \right\rangle. \quad (90)$$

For planar motion, the displacement along the beam axis vanishes, $\Delta Z(t) = 0$, and a compact statistical expression for the FCS correlation follows. It reveals the close relationship to the probability distribution of the squared displacements, Eq. (29), if $G(t; w)$ is interpreted as the corresponding characteristic function. The similarity of the representations in Eqs. (87) and (90) suggests that the FCS correlation encodes important spatial information analogous to scattering methods as soon as the beam waist w is considered an experimentally adjustable parameter [23]. Several FCS setups with spatio-temporal resolution have been implemented recently by introducing variable beam expanders [180, 181], z-scan FCS [182, 183], sub-wavelength apertures [184, 185], near-field scanning optical microscopy [186], or stimulated emission depletion (STED) permitting spot sizes as small as 20 nm [187–189]. Finally, Eq. (90) provides a simple scheme for the efficient evaluation of autocorrelated FCS data in computer simulations from a given trajectory.

For the analysis of a specific FCS experiment, the statistical average needs to be performed and some knowledge about the statistical nature of the fluorophore displacements is required. A common, but in the context of anomalous transport strong assumption is that of a gaussian and isotropic distribution of the displacements $\Delta\mathbf{R}(t)$ after a fixed time lag, i.e., $\langle \Delta\mathbf{R}(t) \rangle = 0$ and only the second cumulant $\delta r^2(t) \equiv \langle |\Delta\mathbf{R}(t)|^2 \rangle$ is non-zero. It follows that $P(\mathbf{k}, t) = \exp(-k^2 \delta r^2(t)/2d)$ being the characteristic function of the random displacements, and the FCS correlation in $d = 3$ is given by [190]

$$G_{\text{Gauss}}(t) = \frac{1}{N} \left[1 + \frac{2}{3} \frac{\delta r^2(t)}{w^2} \right]^{-1} \left[1 + \frac{2}{3} \frac{\delta r^2(t)}{z_0^2} \right]^{-1/2}, \quad (91a)$$

which simplifies in two dimensions to [191]

$$G_{\text{Gauss}}(t) = \frac{1}{N} \frac{1}{1 + \delta r^2(t)/w^2}. \quad (91b)$$

Both expressions allow for a (numerical⁶) inversion at fixed time t and conveniently provide direct access to the mean-square displacement from an FCS experiment [192, 193], without resorting to fitting algorithms. This will be particularly useful in the generic situation where the transport exhibits different regimes depending on the time scale, including crossovers from subdiffusion to normal diffusion (see, e.g., Ref. 19). The quality of the gaussian approximation can be tested experimentally by resolving the spatio-temporal properties of the molecular motion [23], e.g., by systematic variation of the confocal volume [180–189]. Then, the mean-square displacements obtained from Eqs. (91) for different values of w should coincide if the gaussian approximation is applicable.

Specialising to free diffusion, it holds $P(\mathbf{k}, t) = \exp(-Dk^2t)$, and $G(t)$ attains the well-known form

$$G_{\text{free}}(t) = \frac{1}{N} \left(1 + t/\tau_D\right)^{-1} \left(1 + \eta^{-2}t/\tau_D\right)^{-1/2}, \quad (92)$$

with the dwell time $\tau_D = w^2/4D$. Imposing subdiffusion at all times, $\delta r^2(t) \sim t^\alpha$, and assuming gaussian spatial displacements as in fractional Brownian motion, Eqs. (91) yield

$$G_{\text{FBM}}(t) = \frac{1}{N} \left[1 + (t/\tau_D)^\alpha\right]^{-1} \left[1 + \eta^{-2}(t/\tau_D)^\alpha\right]^{-1/2}. \quad (93)$$

This form has been widely employed in FCS-based studies of anomalous transport, maybe because it simply supplements the usual model, Eq. (92), by an additional fitting parameter α . Care must be taken that the additional fitting parameter α is not abused for disclosing experimental deficiencies (e.g., drift) or apparent subdiffusion where the physical picture would actually favour several species with different diffusion coefficients.

For FCS experiments with variable detection volume, it is beneficial to develop some scaling properties of the FCS correlation [23]. Starting from a fairly general scaling ansatz for the transport propagator, $P(r, t) = r^{-d}\mathcal{P}(rt^{-1/d_w})$, Eq. (90) implies the existence of a scaling function $\mathcal{G}(\cdot)$ such that

$$G(t; w)/G(0; w) = \mathcal{G}(tw^{-d_w}). \quad (94)$$

A representation of the l.h.s. as function of the scaling variable tw^{-d_w} should collapse the FCS correlation data for different beam waists w onto a single master curve [23]. In particular, the half-value times $\tau_{1/2}$, defined via $G(\tau_{1/2})/G(0) = 1/2$, are expected to obey

$$\tau_{1/2}(w) \sim w^{d_w}. \quad (95)$$

Wawrezynieck *et al.* [181] suggested to study the phenomenological relation $\tau_d(w) = t_0 + w^2/4D_{\text{eff}}$, termed *FCS*

⁶ In three dimensions, one may alternatively consider to expand the last factor of Eq. (91a) for $\eta \gg 1$, yielding the approximation

$$\delta r^2(t) \simeq 3w^2 \frac{1 - NG(t)}{2NG(t) - \eta^{-2}} \left\{ 1 + \frac{3}{8} \frac{1 - NG(t)}{[NG(t)]^2} \eta^{-4} \right\},$$

which is useful as long as $NG(t) \gtrsim \eta^{-2}$.

diffusion law, where $\tau_d(w)$ is obtained from fitting the simple diffusion model to the FCS data for different beam waists. Based on simulations, they proposed that the transport mechanism can be inferred from the sign of the axis intercept t_0 : negative values would indicate transport hindered by barriers and $t_0 > 0$ would hint at transport in the presence of microdomains with slower diffusion. For a meshwork model, where the tracer diffuses freely in square domains separated by barriers of finite probability, the relation $\tau_{1/2}(w) = (w^2 - a^2/12)/4D$ has been derived analytically for large w , with a being the mesh size and D the long-time diffusion constant [194]. This is consistent with the empirical findings of Ref. 181. A thorough theoretical analysis for other transport models, however, remains still to be done [195].

A general representation of a correlation function for pure relaxation dynamics, e.g., for the incoherent intermediate scattering function, is given by [196]

$$P(k, t) = \int_0^\infty e^{-t/\tau} \Pi_k(\tau) d\tau \quad (96)$$

with a set of positive and k -dependent probability distributions Π_k for the relaxation times τ . From Eqs. (87) and (88), one finds for the FCS correlation function

$$G(t) = \int_0^\infty e^{-t/\tau} \Pi_W(\tau) d\tau, \quad (97)$$

where the distribution Π_W is given by Π_k and depends on the illumination profile, $\Pi_W(\tau) \propto \int d^d k |W(k)|^2 \Pi_k(\tau)$. An interpretation in terms of many diffusing components may be obtained by transformation to

$$G(t) = \int_0^\infty G_{\text{free}}(t; \tau_D) \Pi_{\tau_D}(\tau_D) d\tau_D, \quad (98)$$

using the representation

$$(1 + t/\tau_D)^{-d/2} = \int_0^\infty e^{-t/\tau} \frac{(\tau_D/\tau)^{d/2+1} e^{-\tau_D/\tau}}{\tau_D \Gamma(d/2)} d\tau. \quad (99)$$

The specialisation to two freely diffusing components is widely employed to fit experimental data for transport in crowded media,

$$\Pi_{\tau_D}(\tau_D) = f_1 \delta(\tau_D - \tau_1) + f_2 \delta(\tau_D - \tau_2). \quad (100)$$

For normal as well as for subdiffusive motion, $G(t)$ displays a power-law decay at long times, $G(t) \sim t^{-\beta}$, implying a power law also for the distribution of relaxation times, $\Pi_W(\tau) \sim \tau^{-\beta-1}$ as $\tau \rightarrow \infty$, by means of a Tauber theorem [53, 59]. Iterating the application of the Tauber theorem, the distribution of residence times displays a power-law tail, $\Pi_{\tau_D}(\tau_D) \sim \tau_D^{-\beta-1}$ for $\tau_D \rightarrow \infty$, only in the case of subdiffusion, $\beta < d/2$. Note that for spatially non-gaussian transport, the exponent β and the subdiffusion exponent may not be connected by a simple relation; in case of the Lorentz model, it

involves the fractal space dimension, $\beta = d_f/d_w$ [23]. The numerical determination of the distributions of relaxation times from a given data set for a slowly decaying correlation function is a formidable task [196]; it amounts to performing an inverse Laplace transform, which is a mathematically ill-posed problem [178, 197]. Imposing the additional constraint that the “entropy” of the distribution shall be maximal, Sengupta *et al.* [198] nevertheless introduced a numerical procedure to determine the distribution of diffusion times Π_{τ_D} from a given FCS correlation function $G(t)$, which was successfully applied to the interpretation of experiments [199, 200].

For the measurement of slow, anomalous transport, it is crucial that the FCS correlation covers several decades in time and that the data at long times are still significant. In particular, the choice of an appropriate fit model requires sufficient knowledge about the physics of the sample, and physical constraints on fit parameters or fit windows need consideration [201]. The application of FCS in complex cellular environments has several limitations which may artificially induce weakly subdiffusive behaviour [202, 203] or modify the properties of true anomalous transport [201]; some of these limitations are addressed by advanced derivatives of the FCS technique [178, 204]. We agree that “the physical insight gained from the empirical application of the concept of anomalous diffusion to experimental FCS data may be quite limited, especially if no convincing microscopic origin of the deviation from the normal diffusion law is provided” [178]. This conclusion emphasises the need for more refined theoretical models and for the possibility of their experimental discrimination. Long measurement times, a high signal-to-noise ratio, and the combination of spatial and temporal information seem essential for this task.

4.3. Fluorescence recovery after photobleaching (FRAP)

Simultaneously to the FCS technique, fluorescence recovery after photobleaching (FRAP) was developed [205, 206] and readily applied to membrane proteins on cells [205, 207–209], see Refs. 179, 210–214 for reviews. The method is based on a similar experimental setup as FCS, but initially the fluorophores in the observation region are bleached by a brief, intense laser pulse. Afterwards the fluorescent light intensity emitted from this region is monitored while it recovers due to the diffusion of unbleached fluorophores from outside into the observation region. The method is in some sense complementary to FCS: it uses a high fluorophore concentration and measures the collective transport in form of a diffusion front. It is applicable to very slow processes (even on the scale of several seconds [214]) and appears more robust than FCS if a significant fraction of molecules is immobile [179]. FRAP has become a valuable tool to measure protein motion and activity in drug delivery in pharmaceutical research [211] as well as in living cells [213].

A transparent presentation of the theoretical background

was given by Elson [210] for normal diffusion in two dimensions, which we will briefly summarise. The experiment measures the response of the local fluorophore concentration to an initial quench out of equilibrium. Similar to FCS, the detected fluorescent light intensity $I(t)$ is given by Eq. (83) as integral over the time-dependent, local concentration $c(\mathbf{r}, t)$ weighted with the intensity profile of the detection laser $W(\mathbf{r})$. Let $c_{\text{eq}}(\mathbf{r}) \equiv c_0$ be the homogeneous background concentration of fluorophores before bleaching, $c(\mathbf{r}, 0)$ the imprinted profile directly after the bleaching pulse, and $\delta c(\mathbf{r}, t) := c(\mathbf{r}, t) - c_0$ the partially recovered disturbance after a time t . Repeated measurements of the intensity evolution $I(t)$ result in a non-equilibrium average, $\langle I(t) \rangle_{\text{n.e.}}$; fluctuations across different measurements are not considered. The prebleach intensity and the recovery curve are then given by

$$I_{-\infty} := \langle I(t \rightarrow \infty) \rangle_{\text{n.e.}} = \varepsilon c_0 \int d^d r W(\mathbf{r}), \quad (101)$$

$$I_t := \langle I(t) \rangle_{\text{n.e.}} = I_{-\infty} + \varepsilon \int d^d r W(\mathbf{r}) \langle \delta c(\mathbf{r}, t) \rangle_{\text{n.e.}}. \quad (102)$$

The postbleach intensity is defined as $I_0 := \lim_{t \rightarrow 0} I_t$, and we will give results for the reduced fluorescence recovery function in the following,

$$I(t) := \frac{I_{-\infty} - I_t}{I_{-\infty} - I_0}. \quad (103)$$

Assuming an irreversible conversion of the bleached molecules to a non-fluorescent state, the fluorescence recovery is solely governed by fluorophore transport. Arguing along the lines of Onsager’s regression hypothesis, the macroscopic relaxation to the equilibrium distribution follows the same laws as the regression of a microscopic disturbance of the local fluorophore concentration induced by thermal fluctuations [Ref. 11, section 7.6]. (While the fluctuation–dissipation theorem supports this procedure for small concentration gradients, even for complex dynamics, the validity of this assumption beyond linear response remains to be corroborated.) Specifically, the time evolution of a disturbance $\delta c(\mathbf{r}, 0)$ is governed within linear response theory by the equilibrium correlation function of the concentration fluctuations, namely the van Hove function,

$$\langle \delta c(\mathbf{r}, t) \rangle_{\text{n.e.}} = \int d^d r' S(\mathbf{r} - \mathbf{r}', t) \delta c(\mathbf{r}', 0), \quad (104)$$

where

$$S(\mathbf{r} - \mathbf{r}', t) = \frac{1}{c_0} \langle \delta c(\mathbf{r}, t) \delta c(\mathbf{r}', 0) \rangle \quad (105)$$

for spatially and temporally homogeneous transport. In Fourier space, perturbations with different wavevector decouple and their relaxation is dictated by the intermediate scattering function, Eq. (85),

$$\langle \delta c(\mathbf{k}, t) \rangle_{\text{n.e.}} = S(\mathbf{k}, t) \delta c(\mathbf{k}, 0). \quad (106)$$

For the recovery of detected fluorescence intensity, one finds

$$I_{-\infty} - I_t = -\varepsilon \int d^d r d^d r' W(\mathbf{r}) S(\mathbf{r} - \mathbf{r}', t) \delta c(\mathbf{r}', 0) \quad (107)$$

$$= -\varepsilon \int \frac{d^d k}{(2\pi)^d} W(-\mathbf{k}) \delta c(\mathbf{k}, 0) S(\mathbf{k}, t). \quad (108)$$

The reduced fluorescence recovery function follows as

$$I(t) = \int d^d k \mathcal{W}(\mathbf{k}) S(\mathbf{k}, t), \quad (109)$$

introducing a filter function,

$$\mathcal{W}(\mathbf{k}) := \frac{W(-\mathbf{k}) \delta c(\mathbf{k}, 0)}{\int d^d k W(-\mathbf{k}) \delta c(\mathbf{k}, 0)}, \quad (110)$$

to describe the specific experimental setup. Note that bleaching and detection enter independently and may be implemented with different beam profiles. $S(\mathbf{k}, t)$ is solely determined by the physics of fluorophore transport in the investigated sample. If the molecules diffuse freely,

$$S_{\text{free}}(\mathbf{k}, t) = \exp(-D_c k^2 t), \quad (111)$$

where the collective diffusion constant D_c differs in general from the diffusion constant of a single tracer molecule.

Modelling the fluorophore bleaching as an irreversible first-order reaction, the concentration of unbleached fluorophore immediately after the bleaching pulse is given by $c(\mathbf{r}, 0) = c_0 e^{-K(\mathbf{r})}$, where $K(\mathbf{r})$ is proportional to the beam profile of the bleaching laser and to the duration of the pulse. For free diffusion in two dimensions, bleaching with a gaussian beam, Eq. (89), and detection with the same, but attenuated beam, the recovery of fluorescence intensity can be expressed in terms of the incomplete gamma function or as an infinite series [206],

$$I_t = I_{-\infty} \sum_{n \geq 0} \frac{(-K)^n}{n!} \frac{1}{1 + n(1 + 2t/\tau_d)}; \quad (112)$$

it involves the bleaching parameter $K = K(\mathbf{0})$ and the diffusion time $\tau_d = w^2/4D_c$. The postbleach intensity is calculated as $I_0 = I_{-\infty}(1 - e^{-K})/K$.

If the beam profiles of both the bleaching and the detection laser are approximated by a step-like disc of radius w , the filter function $\mathcal{W}(\mathbf{k})$ assumes a relatively simple form and is independent of the bleaching parameter,

$$\mathcal{W}(\mathbf{k}) = \frac{J_1(kw)^2}{\pi k^2}, \quad (113)$$

where $J_1(\cdot)$ denotes the Bessel function of the first kind; the postbleach intensity is $I_0 = I_{-\infty} e^{-K}$. In the case of free diffusion, Eqs. (109) and (111) yield the fluorescence recovery curve after performing the \mathbf{k} -integration [215],

$$I_{\text{free}}(t) = 1 - e^{-2\tau_d/t} [I_0(2\tau_d/t) + I_1(2\tau_d/t)]; \quad (114)$$

$I_0(\cdot)$ and $I_1(\cdot)$ denote modified Bessel functions of the first kind.

Bleaching patterns other than a spot were implemented experimentally. In fluorescence pattern photobleaching recovery (FPPR), a fringe pattern of periodic stripes is bleached to probe the anisotropic dynamics at finite, non-zero wavenumber k [216–219]. Using a laser-scanning confocal microscope allows for bleaching and probing an arbitrary geometry, e.g., a line segment, with diffraction-limited resolution [220]. Furthermore, the size of a circular bleaching spot can easily be varied, which permits the intrinsic determination of the instrumental resolution parameters [221] and which can elucidate the spatio-temporal properties of anomalous transport analogous to FCS experiments with variable observation volume.

In some experiments, the initial fluorescence is only partially recovered, even after long measurement time, which is commonly attributed to further photobleaching, chemical reactions, or immobile fluorophores [211]. The unrecovered fluorescence intensity is quantified by the ratio

$$R = \frac{I_{-\infty} - I_0}{I_{-\infty} - I_0} = I(t \rightarrow \infty). \quad (115)$$

In this case, fluorophore transport is, strictly speaking, not ergodic and one infers a finite long-time limit of $S(\mathbf{k}, t)$ from Eq. (109),

$$F(\mathbf{k}) := \lim_{t \rightarrow \infty} S(\mathbf{k}, t), \quad (116)$$

determining the incomplete recovery,

$$R = \int d^d k \mathcal{W}(\mathbf{k}) F(\mathbf{k}). \quad (117)$$

In the context of glassy dynamics, $F(\mathbf{k})$ is known as non-ergodicity parameter or Debye–Waller factor [21], and it plays the same role as the Lamb–Möbbauser factor in the case of the incoherent dynamics, c.f. Eq. (77). It follows that the ratio R for the same sample depends via $\mathcal{W}(\mathbf{k})$ on the geometries of the bleaching and detection spots. In particular, FRAP experiments with variable beam waist w of the laser probe the non-ergodicity at different scales. Salomé *et al.* [222] suggested that R is an affine function of the inverse radius, $1/w$, which is motivated by simulations and experiments on compartmentalised membranes. Let us assume that a fraction R_i of the fluorophores is immobile and homogeneously distributed and that the mobile part is ergodic despite the presence of immobile molecules. Then, $F(\mathbf{k}) = R_i$ and the unrecovered intensity is identified with the immobile fraction, $R = R_i$, which is regularly encountered in the literature. More generally, R_i is obtained as small-wavenumber limit of the non-ergodicity parameter,

$$R_i = \lim_{k \rightarrow 0} F(\mathbf{k}). \quad (118)$$

For the study of anomalous transport, Feder *et al.* [223] generalised the FRAP recovery curve, Eq. (112), by assuming

a gaussian subdiffusion model, which effectively amounts to replacing t/τ_d by $(t/\tau_d)^\alpha$. For the intermediate scattering function, this implies a gaussian ansatz in space and a stretched exponential decay in time,

$$S(\mathbf{k}, t) = \exp(-(t/\tau_k)^\alpha), \quad \tau_k \propto k^{-2/\alpha}. \quad (119)$$

Such a stretched fluorescence recovery occurs quite slowly and long measurements are required to distinguish the subdiffusion model from incomplete recovery [223]. More general considerations on FRAP for anomalous transport are still to be worked out; in particular, an extension to spatially non-gaussian transport would be useful. To this end, Eq. (109) may serve as starting point for a similar scaling analysis as above for the FCS correlation function.

5. Anomalous transport in crowded biological media

Application of the discussed techniques to crowded biological media have led to a plethora of experimental results on anomalous transport in the cell interior and in related model systems. In the main part of this section, we provide a compilation of the most significant biophysical experiments addressing anomalous transport and report on the progress made during the past decade. Since a proper characterisation of anomalous transport requires many time and length scales, emphasis is put on the scales investigated by the different experiments. The presentation is divided into three-dimensional transport in cellular fluids (Table II) and crowded model solutions (Table III), and quasi-two-dimensional transport in cellular membranes (Table V) and lipid bilayer models (Table VI). Each experimental subsection is supplemented by a discussion of related computer simulations (Tables IV and VII). The section closes by briefly accounting for recent insights in the implications of crowding for biochemical reactions.

The topic is rather controversially discussed in the biophysics community. Shortly after the turn of the millennium, it was recognised that the heterogeneous structure of intracellular environments can not be neglected in the modelling and description of macromolecular transport and biochemical reactions, with impact on basically all intracellular processes [224–227]. While a number of sound experiments on intracellular transport and related model systems have observed pronounced subdiffusion, other experimental findings are well explained in terms of normal diffusion [158, 228]. The situation becomes even more delicate since “the sub-optimal experimental conditions often encountered in cellular measurements do not allow ruling out simple Brownian diffusion models” [228]. Further, the microscopic mechanisms underlying the subdiffusive motion have not been identified unambiguously until today. We agree with Elcock [229] that there is clearly a need for theory and simulation of microscopic models that can make qualitative and quantitative predictions of the transport behaviour in crowded environments, at least *in vitro*.

5.1. Crowded cellular fluids

5.1.1. Cytoplasm and nucleoplasm (in vivo)

Measurement of molecular transport in living cells faces a series of complications typical for *in vivo* experiments: the cell size of 1 to 100 μm puts a natural upper limit on the accessible length scales, cells may be in different internal states of their cell cycle, and artificial probes may trigger a specific cell response. Further, transport may depend on various cellular processes like directed and active motion by motor proteins along the microtubule network, or cytoplasmic flows induced by the cytoskeleton pushing and pulling organelles around and locally liquefying the cytoplasm [251–253]. For example, the transfection pathway of viruses or gene carriers, visualised by *in vivo* single-particle tracking, crucially involves an intermediate phase of slow passive transport, although cargo transport over large distances is mainly driven by molecular motors [254, 255]. Such enzymatically driven processes may be suppressed or switched off by reduction of temperature or by depletion of ATP [256]. In the following, we will focus on passive transport induced by thermal fluctuations.

An interesting question is to which extent may the cell be considered in a stationary state? The cell is certainly not in an equilibrium state, rather a plethora of biochemical processes is continuously taking place. The cell’s life time is finite, it ages, and the cellular structures and processes change during the cell cycle. These changes, however, occur usually orders of magnitude slower than the typical experimental time scales of milliseconds or seconds at which intracellular transport is studied. We anticipate that a description of the cell as a stationary state is a useful approximation, which of course has its limitations. The issue is partially addressed by some of the experiments covered in this section, a definite answer, however, requires future experimental work.

The fission yeast *Schizosaccharomyces pombe* is a eukaryote with a stiff cell wall that maintains a stable cylindrical shape, 12 μm in length and 4 μm in width. It naturally contains lipid granules with diameters of about 300 nm, which can serve as endogenous, nearly spherical probe particles [230–233]. In their prominent work, Tolić-Nørrelykke *et al.* [230] combined the advantages of 2–3 min long trajectories from video microscopy (at 25 Hz) and the high temporal resolution of laser-based particle tracking (22 kHz) to obtain mean-square displacements (MSDs) spanning a time window of more than 4 decades. The data sets from the two techniques can be consistently extrapolated, bridging the gap between 1 and 40 ms. The data provide clear evidence of subdiffusive motion with an exponent between 0.70 and 0.74 in essentially the whole accessible time window. The optical trapping experiments were refined five years later by the same laboratory [231], focusing on the different phases of the cell cycle. From the positional power spectrum, the subdiffusive motion was confirmed at time scales between 0.1 and 10 ms in all phases with a small,

cell type	probe (size)	experimental technique	temporal and spatial scales investigated	subdiffusion exponent α or diffusion constant D	year	reference
<i>S. pombe</i>	lipid granules (300 nm)	laser tracking, video microscopy	50 μ s–1 ms, 40 ms–3 min	0.70–0.74	2004	ref. 230
		laser tracking	0.1 ms–10 ms (PSD)	0.81 (interphase) 0.84 (cell division)	2009	ref. 231
		video microscopy	10 ms–10 s	0.4 (time average)	2010	ref. 232
		video microscopy, laser tracking	> 10 ms, 0.1 ms–1 s	0.8, normal for $t \lesssim 3$ ms, then $\beta = 1 - \alpha \approx 0.2$	2011	ref. 233
<i>E. coli</i>	mRNA (100 nm)	video microscopy	1 s–30 s, 10^{-3} –1 Hz (PSD)	0.70 ± 0.07 , 0.77 ± 0.03	2006	ref. 234
		video microscopy	1 s– 10^3 s	0.71 ± 0.10	2010	ref. 235
<i>E. coli</i> , <i>C. crescentus</i>	chromosomal loci (GFP labelled)	video microscopy	1 s– 10^3 s	0.39 ± 0.04 (ensemble and time averages coincide)	2010	ref. 235
human osteo-sarcoma cells (nucleus)	telomeres (GFP labelled)	video microscopy	10 ms–1 h	subdiffusion with α varying with lag time, $\alpha(t)$: 0.32 \rightarrow 0.51 \rightarrow 1.	2009	ref. 236
SV-80 cells	PS beads (3 μ m)	video microscopy	40 ms–50 s	0.5–1 for $t > 10$ s, 3/2 for $t < 3$ s (motor proteins)	2002	ref. 237
mammalian & plant cells	rhodamine dye	FCS	$0.1 \text{ ms} < \tau_{1/2} < 1 \text{ s}$	0.6, or 2 components: $D_1 = D_{\text{aq}}/5$, $D_1/D_2 = 40$	1999	ref. 238
COS-7 and AT-1 cells	EGFP proteins	FCS	$\tau_{1/2} \approx 1 \text{ ms}$	0.7–1, or 2 components: $D_1 = D_{\text{aq}}/5$, $D_1/D_2 = 10$	2000	ref. 239
HeLa cells	FITC-dextran (1.8–14.4 nm)	FCS	$0.4 \text{ ms} < \tau_{1/2} < 16 \text{ ms}$	0.71–0.84 (depending on tracer size)	2004	ref. 240
HeLa and liver cells	gold beads (5 nm)	FCS	10 μ s–1 s, $\tau_{1/2} \approx 0.3 \text{ ms}$	0.53, with sucrose added: 0.66	2007	ref. 241
mammalian cells	gold beads (5 nm)	FCS	$0.1 \text{ ms} < \tau_{1/2} < 0.9 \text{ ms}$	0.52 (cytoplasm), 0.58 (nucleoplasm)	2007	ref. 242
HeLa cells	DNA (20 bp–4.5 kbp)	FCS	$5 \text{ ms} < \tau_{D1} < 20 \text{ ms}$, τ_{D2} up to 500 ms (3 kbp)	normal for small tracers, 2 components above 250 bp: $D_2 = D_{\text{aq}}/40$ (size dependent)	2005	ref. 243
<i>D. discoideum</i>	GFP-actin, free GFP	FCS	170 μ s (globular actin), 240 μ s (free GFP)	0.83 (both tracers)	2010	ref. 244
3T3 fibroblasts	dextran, Ficoll (3–58 nm)	FRAP	50 μ m spot size	normal with incomplete recovery, D depends on tracer size, D_{aq}/D up to 30	1986, 1987	refs. 245, 246
3T3 fibroblasts, MDCK cells	dextran, Ficoll (4–30 nm)	FRAP	1 μ s–5 s	normal, $D_{\text{aq}}/D \approx 4$, no dependence on tracer size	1997	ref. 247
myotubes	globular proteins (1.3–7.2 nm)	fringe pattern photobleaching	$\tau_{1/2} \approx 1 \text{ s}$ and 208 s, 10–17 μ m wide stripes	normal, D_{aq}/D : 3–7, but 10^4 for largest protein	2000	ref. 248
	FITC-dextran (2.9–12.6 nm)	fringe pattern photobleaching	–	normal, D_{aq}/D : 2.5–7.7	1996	ref. 249
<i>E. coli</i>	GFP	FRAP	0.1–1 s	normal, $D \approx D_{\text{aq}}/11$	1999	ref. 250

Table II. Overview of *in vivo* experiments on crowded cellular fluids as guide to the discussion in Section 5.1.1. Empty fields repeat the entry above. PSD refers to the power spectral density in the optical trap, and D_{aq} to the diffusion constant in aqueous solution.

but significant variation of α from 0.81 in the interphase to 0.85 during cell division. The larger exponents compared to the earlier work were attributed to possibly disrupted intracellular actin filaments there, and the difference in exponents during the cell cycle was interpreted as a sensitivity to changes of the cytoskeleton.

From the corresponding video microscopy data in the interphase of *S. pombe*, time-averaged MSDs were computed from a small set of 8 long trajectories (up to 200 s) [232]. The MSDs cover time scales from 10 ms to 10 s and indicate subdiffusion with a relatively low exponent of $\alpha \approx 0.4$. The ensemble- and time-averaged MSDs support this low exponent

for $0.1 \text{ s} < t < 1 \text{ s}$, but the statistical noise permits a possible crossover to the previously found larger exponent at shorter times. Additional statistical quantities like higher cumulants or the mean maximal excursion are used to test the shape of the probability distribution of the displacements. It was concluded that the investigated data set is neither compatible with the CTRW model nor with a percolation scenario, but shares some features with fractional Brownian motion. Further improvements of the laser-tracking setup yielded very long trajectories with 22 kHz resolution of lipid granules during cell division of *S. pombe* [233]. The time-averaged MSDs at time scales between 10^{-4} to 1 s, clearly exhibit a crossover around 3 ms from normal diffusion to subdiffusion with exponent $\beta \approx 0.2$, while the short-time MSDs obtained earlier [230, 231] display subdiffusion with the exponent $\alpha \approx 1 - \beta$. Such a peculiar behaviour is recreated in terms of a CTRW model with truncated power-law waiting-time distribution and has been related to the confinement by the optical trap. We refer the reader to the original literature for a detailed discussion [231–233]. Tracking the granules by video microscopy at time scales above 10 ms yielded subdiffusive motion with $\alpha \approx 0.8$, similarly as in the earlier experiments.

Summarising, the transport of granules in fission yeast has been studied with great precision over almost a decade and displays a complex behaviour varying over the range of observation time scales. The experimental data are partially described in terms of FBM and a properly adapted CTRW model, but a consistent phenomenological description valid at all time scales is yet to be found. The microscopic mechanism leading to subdiffusive motion has not yet been resolved.

In a highly recognised experiment addressing the physical nature of bacterial cytoplasm, Golding and Cox [234] used video microscopy at 1 Hz to follow the motion of fluorescently labelled mRNA macromolecules (radius on the order of 100 nm) over up to 30 minutes in *E. coli*, a rod-shaped bacterium about 2 μm long and half a micron in diameter. The analysis of 70 trajectories yielded subdiffusion at time scales between 1 to 30 s with varying prefactor, but rather robust exponent $\alpha = 0.70 \pm 0.07$. Concatenating all trajectories, a power spectrum was obtained over three decades in time, which clearly indicates subdiffusive behaviour with exponent $\alpha = 0.77 \pm 0.03$. These findings agree with the limiting value of α in artificial crowding conditions using dextran [199], see Section 5.1.2.

Subdiffusion with a significantly smaller value $\alpha = 0.39 \pm 0.04$ was obtained from time-lapse fluorescence microscopy tracking of GFP-labelled chromosomal loci in *E. coli* and *Caulobacter crescentus* over 10^3 s [235]. For RNA proteins in *E. coli*, subdiffusion with $\alpha = 0.71 \pm 0.10$ was observed in agreement with Ref. 234. These findings were rationalised by supplementing the Rouse model for polymer dynamics by a fractional gaussian noise term [257] and arguing that the monomer dynamics at short times is then characterised by the

exponent $\alpha' = \alpha/2$. Further, a CTRW scenario was ruled out as time- and ensemble-averaged data coincide. Analysis of the VACF showed pronounced anti-correlations and a description in terms of a Langevin equation with power-law correlated, spatially gaussian noise was favoured.

Tracking the motion of telomeres in the nucleus of human osteosarcoma cells in a broad time range of almost 6 orders of magnitude displayed subdiffusive motion with varying exponent depending on lag time [236]. Between 0.1 ms and 1 s, a small value of $\alpha \approx 0.32 \pm 0.12$ was found, changing to 0.51 ± 0.20 in the intermediate regime up to 200 s, and approaches normal diffusion for longer times; the amplitude of the power laws varied over an order of magnitude from one telomer to another. An interpretation in the framework of the CTRW was found to not fully explain the experimental results, mainly since ageing behaviour could not be corroborated. The dynamics is, however, compatible with the dynamics of entangled polymers: the reptation model for a Rouse chain predicts an exponent of 1/4 for the short-time relaxation, crossing over to 1/2, and finally free diffusion.

The interaction with cytoskeletal fibres and motor proteins was probed by engulfing 3 μm polystyrene beads into various eukaryotic cells and monitoring their motion by video microscopy [237]. The obtained MSD was found to grow superdiffusively with $\alpha \approx 3/2$ at time scales less than 3 s, while a crossover to subdiffusive motion was observed for longer times ($0.5 < \alpha < 1$). The latter finding, however, is subject to statistical noise and could be followed over less than half a decade only. The superdiffusive transport, $\delta r^2(t) \sim t^{3/2}$, was explained in terms of a generalised Langevin equation that accounts for the stochastic driving by motor proteins and the power-law memory due to the subdiffusive thermal fluctuations of semiflexible polymers, $\delta r^2(t) \sim t^{3/4}$. Further, the crossover to subdiffusion with $\alpha = 1/2$ was rationalised by the decorrelation of motor activity at long time scales.

Owing to technological advances in the 1990s, the FCS technique has quickly become an established tool for dynamic studies at the mesoscale, permitting also intracellular applications. *In vivo* measurements benefit from the high temporal resolution as well as from the choice of tracers ranging from tiny fluorescent proteins to labelled polymer coils and inert nanoparticles. Such tracers can be incorporated into the cell with only mild physiological side effects. In a pioneering work, Schwille *et al.* [238] established the application of FCS to the cytoplasm by studying the diffusion of tetramethyl-rhodamine dye with single molecule sensitivity in various mammalian and plant cells. They found subdiffusion in the different cell types with $\alpha \approx 0.6$, but the same data may equally well be rationalised by fitting a mixture of two normally diffusing components, the faster one being 5-fold slower than in aqueous solution. The slow component showed diffusion constants up to 40 times smaller than the fast one and comprised 35–60% of the molecules; the slow component was

attributed to membrane-bound dye as the diffusion coefficients are of similar magnitude.

The variation of anomalous transport with the spatial position in the cell was addressed using genetically modified COS-7 and AT-1 cells that express fluorescent EGFP proteins [239]. The obtained FCS correlations displayed anomalous diffusion depending on the position in the cell, the largest anomalies were observed in the nuclei. The data were analysed in terms of subdiffusion and two diffusive components. In the first case, the exponent α varied between 0.7 and 1 with half-value times around 1 ms. The two-component fits yielded a ratio between the diffusion constants of about 10, where the larger value was 5-fold reduced compared to free diffusion of EGFP in aqueous solution.

Weiss *et al.* [240] introduced differently sized FITC-labelled dextrans in HeLa cells and characterised their motion with FCS. For all molecular weights studied, the correlation functions displayed anomalous transport and were fitted with the gaussian subdiffusion model, Eq. (93). The obtained values for the exponent α varied between 0.71 and 0.84 non-monotonically depending on the size of the dextran polymers, which covered hydrodynamic radii in buffer solution between 1.8 and 14.4 nm. The dwell times τ_D , on the other hand, increased systematically from 0.4 to 16 ms. Complementing their study by *in vitro* experiments with unlabelled dextran as crowding agent, the authors found a systematic decrease of α with the concentration of dextran, which suggests to quantify the degree of crowdedness in terms of the subdiffusion exponent α .

Probing the cytoplasm and the nucleus of living HeLa cells as well as healthy and cancerous liver cells at the nanoscale by introducing fluorescently tagged 5 nm-sized gold beads revealed pronounced anomalous transport over five decades in time [241]. One advantage of using gold particles instead of (branched) polymers as probe is to reduce interactions with the cytoplasm, like polymer entanglement, potentially modifying the tracer transport. The FCS data were fitted with an empiric model that interpolates between subdiffusion at short times and normal diffusion at long times, see Eq. (91a) with $\delta r^2(t) = 6w^2[t/\tau_d + (t/\tau_s)^\alpha]$. It consistently yielded $\alpha \approx 0.53$, $\tau_s \approx 0.3$ ms, and $\tau_d \approx 90$ ms across all cell types, with α being slightly larger in the nucleus; these parameters imply a crossover time scale between the two transport regimes, $t_x = (\tau_d \tau_s^{-\alpha})^{1/(1-\alpha)} \approx 56$ s, which is beyond the scope of current experiments. When the cells were osmotically stressed by adding high, but non-apoptotic concentrations of sucrose, raffinose, or NaCl, the subdiffusive transport changed markedly: α attained values around 0.66, while the dwell time τ_s increased by a factor of 3 in the cytoplasm and up to 2.4 ms in the nucleus. Considering the cyto- or nucleoplasm a concentrated polymer solution, the observations were rationalised by a change of solvent conditions qualitatively modifying the visco-elastic properties of the medium.

An extension of this study [242] covered a representative collection of mammalian cells, with different origin (from Chinese hamster ovary (CHO) cells to human osteosarcoma cells) and state of health (immortalised Thle-3 from a healthy liver vs. highly aggressive human glioma cells). Again, the gold nanobead displayed subdiffusive motion with $\alpha \approx 0.52$ in the cytoplasm and $\alpha \approx 0.58$ inside the nucleus, with only small variations across cell lines; the dwell times varied between 0.1 and 0.3 ms with some exceptions reaching up to 0.9 ms in the nucleoplasm. In conclusion, very different mammalian cells show a similar degree of crowding at the nanoscale with the nucleus being somewhat less crowded than the cytoplasm. In particular, differences in the macroscopic visco-elastic response depending on a cell's development and disease state appear to be not reflected in the transport at the nanoscale.

Dauty and Verkman [243] investigated the size-dependent transport of DNA in the cytoplasm of living HeLa cells with DNA molecules sized between 20 to 4,500 bp and labelled with a single fluorophore. The motion of DNA was followed by FCS, the fitting of correlation functions for sizes above 250 bp required a two-component model with a short diffusion time of 5–20 ms independent of DNA size; the diffusion time of the slow component ranged up to ≈ 500 ms for 3 kbp. Various sources were suggested as origin of the fast component, yet it could not be identified unambiguously. DNA diffusion was found to be significantly reduced in comparison to the free diffusion in saline by factors of up to 40, with a pronounced dependence on molecular weight above 500 bp. This dependence, however, almost disappeared by disrupting the actin cytoskeleton: the FCS data exhibited simple diffusion with an approximately 5-fold reduction. The authors have corroborated their findings by *in vitro* experiments using crowded solutions, cytosol extracts, and reconstituted actin networks. Only for the actin networks, the suppression of the DNA diffusion constant over its free value was sensitive to the molecular weight, recreating the behaviour in intact HeLa cells. In all other environments, simple diffusion was observed with reduction factors not exceeding 5. The authors concluded that mobile obstacles can not explain the strongly reduced mobility of DNA in living cells and that the actin cytoskeleton presents a major restriction to cytoplasmic transport. Further, the sensitivity of diffusion to the molecular weight may be explained by entanglement effects with the actin mesh and reptation dynamics of the elongated DNA molecules.

Transport of globular actin molecules, a building block of the cytoskeleton, was investigated by FCS in living *Dicystostelium discoideum* cells [244] using mutants that express either GFP-labelled actin or free GFP. Measurements in the cytoplasm displayed anomalous transport for both probes, fits of the gaussian subdiffusion model yielded in both cases $\alpha \approx 0.83$ with half-value times of 170 μ s for free GFP and 240 μ s for G-actin. In the lysate of the actin mutant, transport was even slower with $\alpha \approx 0.72$, but with a half-value time reduced

by a factor of 2.5; here, a two-component fit was not able to detect an anticipated slow diffusive component. Further, a low degree of actin polymerisation was found in the cytoplasm, and thus, the slow transport was mainly attributed to crowding effects. Transport in the presence of an highly polymerised actin network was monitored by means of fluorescent LIM proteins marking the actin polymerisation front in the cell cortex. While transport was normal in the corresponding lysate, subdiffusive motion with $\alpha = 0.79 \pm 0.02$ was observed in the living cell. Given that an exponent 3/4 is expected for *in vitro* actin networks [193], the observed anomalous transport may be caused by polymer fluctuations in this case.

Luby-Phelps *et al.* applied the FRAP technique to fluorescently labelled dextran [245] and Ficoll [246] molecules microinjected into the cytoplasm of living Swiss 3T3 fibroblasts. The tracer radii ranged from 3 nm to 25 nm (Ficoll) and 58 nm (dextran). The obtained diffusion constants were substantially reduced relative to their values in aqueous solution, depending on the tracer size; a 30-fold reduction was observed for the largest Ficolls. The initial fluorescence was fully recovered for molecules smaller than 14 nm (dextran) or about 20 nm (Ficoll), indicating that all tracers are mobile. For larger molecules, the fluorescence recovery was increasingly incomplete, and it was inferred that a fraction of the molecules is trapped. These observations are consistent with the picture of a significant excluded volume hindering cytoplasmic transport.

Targeting the same experimental system, Seksek *et al.* [247] made different observations using an improved FRAP apparatus with microsecond resolution and measurement times of several seconds. The diffusion constants of labelled dextran and Ficoll molecules in the cytoplasm of T3T fibroblasts as well as MDCK epithelial cells were only 4-fold reduced relative to aqueous solution. In particular, no size dependence of this factor could be detected for a comparable range of tracer radii, in contrast to the results in Refs. 245 and 246. As in these works, the FRAP analysis was based on the half-value times of fluorescence recovery rather than on fits of the full recovery curve. Nevertheless, investigation of the recovery dynamics at long times did not display deviations from normal diffusion. In agreement with the earlier experiments, fluorescence was only partially recovered for increasing molecular weight, even at the scale of seconds. This is again consistent with the presence of spatial heterogeneity in the form of persistent structures or obstacles that immobilise a significant fraction of the larger macromolecules.

A derivative of the FRAP technique is modulated fringe pattern photobleaching, which was employed by Arrio-Dupont *et al.* [248] to investigate the mobility of different globular proteins in cultured myotubes. The studied myotubes are elongated cells, 10–40 μm wide and up to 1 mm in length. Applying fringe patterns of 10–17 μm wide stripes yielded recovery time constants of several seconds for labelled proteins with hydrodynamic radii between 1.3 and 5.4 nm. These time con-

stants translate into a 3 to 7-fold suppression of protein mobility relative to aqueous solution. For β -galactosidase, which has a hydrodynamic radius of ≈ 7.2 nm, a drastic suppression by 4 orders of magnitude compared to aqueous solution was found from the extremely slow fluorescence recovery with a time constant of 208 s. The results clearly display a monotone dependence of the suppression factor on protein size. Similar results were obtained for a series of differently sized dextran molecules in the same cell type [249], but the mobility is more size-sensitive for globular proteins. The apparent discrepancy with the findings of Ref. 247 may be explained by the very different time and length scales probed by both experiments, and in this sense they complement each other.

Combining FRAP and a photoactivation technique allowed for a non-invasive measurement of the motion of endogenously expressed GFP in the cytoplasm of *E. coli* bacteria [250]. The apparent diffusion constant was obtained as $7.7 \pm 2.5 \mu\text{m}^2/\text{s}$ at the time scale of some 0.1 s, which is about 11 times smaller than for free diffusion in water and significantly lower than in eukaryotic cells.

5.1.2. Crowded model solutions (in vitro)

Important progress in the understanding of anomalous transport was made by biologically motivated model systems, where in contrast to living cells key parameters are adjustable. In many cases, the crowded solutions are made from linear or branched (bio-)polymers of different rigidity, but proteins were used as crowding agents just as well.

A component of the cytoskeleton is filamentous actin, an elongated, semiflexible polymer forming dense, entangled networks, e.g., in the cell cortex. Solutions of reconstituted F-actin offer a model system to investigate the mechanical properties of these networks *in vitro*. The thermal motion of colloidal tracer particles (radius 0.25 μm) in semidilute F-actin solutions was tracked with video microscopy at 30 Hz over 20 min [258]. The obtained MSDs display subdiffusion on time scales between 0.1 and 10 s with an exponent varying between 0 and 1 upon varying the actin concentration and thereby the mesh size of the networks between 0.17 and 0.75 μm . Normal diffusion was observed for mesh sizes larger than the tracer radius. The results can not be interpreted in terms of the macroscopic frequency-dependent shear viscosity. Analysis of the trajectories suggests that the tracers are caged by the network and the motion resembles a series of infrequent and large jumps with power-law distributed waiting times.

Diffusing wave spectroscopy experiments [259] on 0.48 μm -sized colloids embedded in F-actin solutions explored the large temporal window between 1 μs and 100 s. The MSD shows normal diffusion at short times up to 10 ms, where caging effects appear. The time-dependence of the diffusion coefficient is clearly observed and displays a suppression by 6 orders of magnitude.

crowding agent	probe (size)	experimental technique	temporal and spatial scales investigated	subdiffusion exponent α or diffusion constant D	year	reference
F-actin	colloid (0.25 μm)	video microscopy	0.1–10 s	$0 \leq \alpha \leq 1$ depending on mesh size of actin network	2004	ref. 258
	colloid (0.48 μm)	diffusing wave spectroscopy	1 μs –100 s	crossover <i>normal</i> \rightarrow <i>caging</i> near 10 ms, $D(t)$ spans 10^6	1999	ref. 259
	nanosphere (25–250 nm)	video microscopy	50 ms–10 s	normal MSD, but anomalous, exponential propagator	2009	ref. 172
<i>fd</i> virus	protein (3.5 nm), silica spheres (35–500 nm)	FCS, dynamic light scattering, video microscopy	sensitivity: 10 μs –1 s	D_{aq}/D : 1 \rightarrow 10 as $[fd] \uparrow$	2005	ref. 260
dextran	FITC-dextran (10–500 kDa)	FCS	$\tau_{1/2}$: 0.3 \rightarrow 30 ms	1 \rightarrow 0.6 monotonically as $[\text{dextran}] \uparrow$	2004	ref. 240
	apoferritin	FCS	$\tau_{1/2} \approx 100$ ms (675 μs in saline)	0.7–0.9 (mean 0.82), no ageing, stationary process	2009	ref. 261
	streptavidin, EGFP	FCS	1 ms–1 s	1 \rightarrow 0.74 monotonically as $[\text{dextran}] \uparrow$	2005	ref. 199
dextran (30 wt%)	beads (50 nm)	laser tracking	50–500 ms	subdiffusion ($\alpha = 0.82$), no signs of ergodicity breaking, FBM most likely	2012	ref. 67
Ficoll-70	dye, proteins, polymers, beads (1–100 nm)	FCS	$\tau_{1/2}$: 0.3 \rightarrow 100 ms (rhodamine green)	normal, $D_{\text{aq}}/D > 100$, exponential suppression: $D \sim \exp(-a[\text{Ficoll}])$	2004, 2008	refs. 158, 262
micellar solution (C_{12}E_6)	dye, proteins, nanoparticles (1.7–190 nm)	FCS	–	normal, 2 components, D_{aq}/D_1 : 1 \rightarrow 10 (free tracers), $D_1/D_2 \approx 10$	2006	refs. 263, 264
dextran (500 kDa)	ribonuclease A	FCS	–	normal, free and bound protein: $D_1/D_2 \approx 7$	2011	ref. 265
BSA protein	BSA protein (3.6 nm)	neutron scattering	0.3–5 ns, wavelength: 0.5–3.3 nm	normal, $D_{\text{aq}}/D_{\text{short}}$: 1 \rightarrow 10, hydrodynamic effects	2010, 2011	refs. 266, 267
glycerol, PVP, Ficoll, proteins, <i>E. coli</i> lysate	CI2 protein (7.4 kDa)	nuclear magnetic resonance	–	test of Stokes–Einstein relation for translational and rotational motion	2010	ref. 268

Table III. Overview of *in vitro* experiments on crowded model fluids as guide to the discussion in Section 5.1.2. Empty fields repeat the entry above, right arrows indicate a systematic change upon variation of some parameter, up/down arrows indicate increase/decrease of some quantity. Abbreviations: FBM... fractional Brownian motion, [X]... concentration of X.

In a related experiment, Wang *et al.* [172] tracked the motion of nanospheres in semidilute F-actin solution. Choosing the tracer radius (25–250 nm) much smaller than the mesh size, normal diffusion was expected. The measured MSDs indeed grow linearly in the window between 50 ms and 10 s. Yet, transport is anomalous: the van Hove function $P(r, t)$ decays exponentially with r rather than following a gaussian. Likewise, the propagator exhibits scaling upon rescaling distances as in normal diffusion, $\hat{r} \propto rt^{-1/2}$, but the resulting scaling function is anomalous. Similar findings were made for the quasi-one-dimensional diffusion of beads along phospholipid bilayer tubes.

Another model system for a semiflexible biopolymer is the *fd* virus, being a stiff filamentous phage of contour length 880 nm, diameter 6.6 nm, and persistence length 2.2 μm . Kang *et al.* [260] studied transport in semidilute suspensions of *fd* virus using differently sized tracers: a protein of radius 3.5 nm

and labelled silica spheres with radii from 35 to 500 nm. Measurement of the long-time self-diffusion constant required suitable techniques to cover the large range of particle sizes: fluorescence correlation spectroscopy for the protein and the small colloids, dynamic light scattering for intermediate-sized spheres, and video microscopy was found most appropriate for the large spheres. The obtained diffusion constants are systematically suppressed by up to an order of magnitude when the concentration of *fd* increases; the effect is more pronounced for the larger tracers. Above the overlap concentration, i.e., in the semidilute regime, the *fd* rods span a network and an average mesh size can be assigned. The diffusion constants as function of the tracer radius divided by the mesh size, however, display strong deviations from scaling—in contrast to the findings for cross-linked networks. This may be explained by the dynamically changing structure of the *fd* network, whose constituents themselves are subject to Brownian motion.

Aqueous solution of dextran molecules may also serve as a model system for a crowded fluid [240]. FCS measurements on a small fraction of labelled dextran molecules (10, 40, and 500 kDa in weight) revealed a systematic decrease of the exponent α with a concomitant increase of the half-value time as the crowding agent is more concentrated. The half-value times varied over an order of magnitude as a function of unlabelled dextran concentration, and the ‘‘anomaly parameter’’ α reached values below 0.6 for the 40 kDa-dextran tracers.

A benefit of using well-defined model systems is the possibility to perform a detailed statistical analysis of anomalous transport at a given point in parameter space. FCS measurements on labelled apoferritin in a concentrated dextran solution were repeated many times at the same spot to generate histograms of the residence times and of the exponent α [261]. The exponent covered values between 0.7 and 0.9 with mean 0.82; a systematic variation of α , indicating ageing of the sample, was not observed. These distributions were then critically compared to computer simulations of the FCS experiment for various models of anomalous transport: CTRW, FBM, and obstructed diffusion on a percolating cluster (see Section 3), all of them generating the same subdiffusive MSD with (apparent) exponent $\alpha = 0.82$. While FBM and obstructed diffusion provide a good description of the experimental data, the results from the CTRW model are in qualitative and quantitative disagreement. This indicates that crowding-induced subdiffusion is more appropriately described by a stochastic motion with stationary increments than by a CTRW with untruncated waiting-time distribution.

In the same lab, single-particle tracking experiments of fluorescent 50 nm beads in a solution of 30% 500 kDa-dextran were performed with temporal and spatial resolution of 4 ms and 10 nm, respectively [67]. For lag times between 50 ms and 500 ms, the time-averaged MSDs exhibited subdiffusion with an average exponent $\alpha \approx 0.82$ as before. At about 1 s, a crossover towards normal diffusion was observed. The analysis of 21 trajectories showed no signs of ergodicity breaking, and comparing their geometric properties to the models of Section 3, fractional Brownian motion was found to match quantitatively.

The monotone dependence of the subdiffusion exponent α with the concentration of crowding agent was corroborated by Banks and Fradin [199], who used the globular proteins streptavidin and EGFP as tracers in dextran solution. The conventional χ^2 -fit of the FCS data with the gaussian subdiffusion model was substantiated further: On a double-logarithmic representation, the long time decay of the FCS correlation is compatible with the subdiffusion model down to the noise level of about 5×10^{-3} and clearly deviates from the power law $t^{-3/2}$, expected for normal diffusion. Second, an analysis assuming a large number of diffusive species, Eq. (98), yields a continuous distribution of diffusion times between 0.1 and 10 ms, rather than, e.g., a bimodal distribution. The resulting expo-

nents of subdiffusion decrease rapidly for increasing concentrations of dextran obstacles and approach $\alpha = 0.74 \pm 0.02$ for high concentrations. This value appears to be related to the exponent $3/4$ characterising the internal polymer dynamics of the dextran chains. Dextran aggregates are ruled out as source of anomalous diffusion, and the subdiffusive motion is remarkably robust against temperature variations, merely the half-value times reflect the changing viscosity of water. Further, the motion of the small fluorescein molecules as well as of the dextran crowders itself shows simple diffusion even at high dextran concentration. If a globular protein is used as crowding agent, streptavidin motion is only slightly anomalous with $\alpha \approx 0.91$ at high concentrations.

Ficoll-70 served as crowding agent as well, being an inert, highly branched polysaccharide of approximately spherical shape with a hydrodynamic radius of 5.5 nm. Verkman *et al.* [158, 262] characterised the transport of differently sized tracers in Ficoll-crowded solution using FCS with an illumination region of 0.5 μm in diameter. The tracers covered about two decades in size and ranged from rhodamine green over labelled proteins, dextrans, and DNA fragments to fluorescent polystyrene beads with up to 100 nm in diameter, the latter mimicking cellular organelles. Although the FCS correlations displayed simple diffusion in all cases, tracer transport slows down drastically upon systematically crowding the solution. The obtained diffusion coefficients are suppressed by two to three orders of magnitude as Ficoll concentration increases up to 60 wt% and follow an exponential law. All tracers showed qualitatively the same behaviour, independently of their size. Using the smaller glycerol as crowding agent, the reduction of diffusion is smaller, but still exponential. For the large tracers, the slow diffusion can to a large extent be explained by the change of the macroscopic viscosity of the crowded fluid. This correlation is less pronounced for the small rhodamine green molecule, which appears to sense the microviscosity of its local environment.

Another model for a crowded environment is given by aqueous micellar solution made of the non-ionic surfactant C_{12}E_6 . Szymański *et al.* [263] studied diffusion constants of TAMRA-labelled lysozyme proteins with FCS for a wide range of C_{12}E_6 concentrations and found systematic deviations from free diffusion for concentrations above 3 wt%. A fit of the FCS correlation data, however, required a two-component diffusion model with only 10% of the proteins in the slow component; a possible explanation for the slow diffusion is the formation of protein–micelle complexes. Slow and fast diffusion constants are both suppressed by up to an order of magnitude at the highest concentration studied (37 wt%) and are separated by another order of magnitude. The gaussian subdiffusion model fits the data equally well yielding a systematic decrease of the exponent α down to 0.88, but the interpretation in terms of two components was favoured due to its clear physical interpretation. Focusing on the unbound fraction, the exponential

suppression of diffusion with concentration was consistently reproduced for a variety of fluorescent tracers covering sizes from 1.7 to 190 nm [264]. For the larger tracers, the diffusion constants are determined by the macroscopic viscosity of the micellar solution via the Stokes–Einstein relation. In contrast, the diffusion constant of small tracers show a high sensitivity to the tracer size: in the concentrated solution, apoferritin diffuses about 100-fold slower than lysozyme although the radii of the two proteins differ only by a factor of 3.6. The crossover length scale of 17 nm was identified with the persistence length of the micelles.

The interplay of binding and crowding was addressed by means of a model system of negatively charged dextran molecules (500 kDa) as crowders and the positively charged protein ribonuclease A as tracer [265]. The tracer protein binds reversibly and non-specifically to a dextran molecule. Already at dilute concentrations of dextran (1 μM), the FCS correlation signals the presence of a large fraction of bound protein with about 7-fold suppressed diffusion constant, reflecting the increased hydrodynamic radius of the compound. Protein diffusion in solution of positively charged and neutral dextrans is unaffected at these low concentrations and reduced by merely a factor of 2 at the highest polymer concentration studied (100 μM), crowding effects are still small. The data are fully explained by the coexistence of free and bound protein, both of them exhibiting simple diffusion.

Neutron scattering is a non-invasive technique to access protein solution samples at high protein concentrations at nanosecond and nanometre scales. Using quasi-elastic neutron backscattering, Roosen-Runge *et al.* [266, 267] probed the self-diffusion of bovine serum albumin (BSA) proteins in crowded aqueous solutions, where the same protein served as crowding agent. The protein motion was inferred from the incoherent dynamic structure factor $P(k, \omega)$ of the hydrogen atoms, and the data are compatible with simple diffusion for wavelengths between 0.5 and 3.3 nm and time scales between 0.3 and 5 ns. Increasing the protein content up to 30% volume fraction, a 10-fold reduction of the translational *short-time* diffusion coefficient over its value in dilute solutions was observed. Previous theoretical and experimental studies for hard-sphere colloids showed that diffusion is considerably slowed down already at short times when hydrodynamic interactions are taken into account, followed by a further slowing down at long times for high volume fractions [269, 270], see also Ref. 271 discussed in Section 5.1.3. The reported BSA diffusion constants compare well with the findings for short-time diffusion of hard spheres if an effective hydrodynamic protein radius is used, which accounts for the hydration shell and the oblate ellipsoidal protein shape; the effective radius was determined to 3.6 nm from small-angle X-ray scattering. Noting further that at time scales of a few nanoseconds the caging by surrounding proteins is expected to be not yet effective, this suggests that the observed slow-down of protein diffusion

is mainly caused by hydrodynamic interactions and that protein diffusion in a crowded environment cannot be understood merely by excluded volume and confined motion.

Nuclear magnetic resonance spectroscopy was employed to quantify both the rotational and translational diffusion of the protein chymotrypsin inhibitor 2 (CI2) in a variety of crowded solutions as function of crowder concentration [268]. The crowding agents comprised glycerol, synthetic polymers (PVP, Ficoll), globular proteins (BSA, ovalbumin, lysozyme), and *E. coli* cell lysates. The macroscopic shear viscosity of the solution, η , increases with crowder concentration. Then the Stokes–Einstein relation already suggests a reduced diffusivity, $D \propto 1/\eta$, which describes the measured CI2 diffusion constants in glycerol solution and also translational diffusion in ovalbumin, BSA, and cell lysate. In solutions of synthetic polymers, transport is affected less than expected from the increase of viscosity, and the translational motion of CI2 is impeded more than its rotational motion. Surprisingly, the opposite effect was found in protein-crowded solutions and in the cell lysate: rotational diffusion constants were suppressed stronger than translational diffusion and stronger than the Stokes–Einstein relation would imply. The findings were attributed to weak non-specific, non-covalent chemical interactions between proteins, while synthetic polymers tend to form a loose mesh work. This suggests that crowded protein solutions are preferred for modelling the effects of the intracellular environment on protein transport.

5.1.3. Computer simulations (in silico)

Anomalous transport and subdiffusion were unambiguously identified in computer simulations for minimalist, generic models as well as for elaborate cytoplasm models targeting a specific cell type. These results provide essential support for the interpretation of experiments and test various microscopic pictures behind anomalous transport.

A paradigm of anomalous transport is provided by the motion of a small tracer in a disordered matrix of spherical obstacles, known as Lorentz models [79, 115, 126, 127]; see Section 3.3 for a thorough discussion and its connection to continuum percolation theory. As a localisation transition is approached by tuning the excluded volume, a growing window of subdiffusion emerges at intermediate time scales. The tracer dynamics generically displays a double-crossover scenario from microscopic motion at very short time scales to subdiffusion and to normal diffusion at large times [115]. This phenomenology is preserved, whether the microscopic tracer motion is ballistic like in a porous medium or overdamped like in the cytoplasm [79]. The apparent exponent of the subdiffusive regime decreases monotonically upon approaching the transition and converges to its universal value, $\alpha \approx 0.32$ or 0.42, depending on whether the tracer is restricted to the percolating space or not [127]. Subdiffusive transport over 6 decades in times at the critical obstacle density and a suppres-

crowded environment	tracer	interactions	subdiffusion exponent α and temporal window	year	reference
10 ⁶ spherical obstacles (overlapping, equal size)	point (ballistic and overdamped motion)	hard core	1 \rightarrow 0.32 \rightarrow 0, subdiffusion over up to 6 decades in time	2006, 2008	refs. 79, 115
			1 \rightarrow 0.42 \rightarrow 0 (percolating cluster only)	2011	ref. 127
1000 spheres (equal size), fluid in obstacle matrix	fluid particles	hard core	1/2 over 4 decades in time	2009, 2011	refs. 100, 101
1000 spheres (bidisperse, partially quenched)	mobile particles	hard core	0.3 over 4 decades in time	2009, 2010	refs. 102, 103
2000 spheres (size-disparate mixture)	small particles	soft repulsion	0.63 and 0.5 over several decades	2006, 2009	refs. 272, 273
5000 spheres with weight distributed modelling HeLa	small spheres (2–5 nm)	hard core, soft repulsion	1 \rightarrow 0.55, subdiffusion over 3 decades in time	2004	ref. 240
atomistic <i>E. coli</i> model: 1000 macromolecules of 50 different types	macromolecules (10–1000 kDa)	repulsion, vdW attraction, electrostatic, hydrodynamic	0.75–0.85 @ 100 ps–1 μ s (full set of interactions)	2010	ref. 274
<i>E. coli</i> model: 15 molecule types, 1300 molecular-shaped or spherical particles	macromolecules	repulsion, vdW attraction, hydrodynamic (spheres only)	D_0/D_{short} : 3–10 (with HI), anomalous \rightarrow normal at 1 μ s, $D_{\text{short}}/D \approx 2$ (with HI) or 20	2010	ref. 271
1000 spherical obstacles (non-overlapping, equal size) and 10 ⁶ solvent particles	globular polymer (400 beads)	repulsion, vdW attraction, hydrodynamic (MPCD)	1–0.7 depending on excluded volume and polymer size	2010	ref. 275
polymeric network	free monomer	repulsion, vdW attraction	1/2 or 3/5 over up to 2 decades in time	2011	ref. 276

Table IV. Overview of computer simulations on crowded fluids as guide to the discussion in Section 5.1.3. Empty fields repeat the entry above, arrows indicate a systematic change upon variation of some parameter. Abbreviations: vdW...van der Waals, HI...hydrodynamic interactions, MPCD...multi-particle collision dynamics.

sion of the time-dependent diffusion constant by 5 orders of magnitude was observed in the simulations [126, 127]. Even 10% off the critical obstacle density, the motion is subdiffusive with exponent $\alpha \approx 0.5$ over still 2 decades in time. Thus for the observation of anomalous transport over a finite time window, it is not essential that the system is fine-tuned to the critical point. The scenario of the localisation transition appears to be robust: subdiffusive motion with exponent 1/2 over 4 decades in time was found in simulations for a hard-sphere fluid adsorbed in a matrix of disordered, non-overlapping hard-sphere obstacles [100, 101]. Simulations for a similar system where the tracer fluid and the obstacles are correlated yielded subdiffusion over 4 decades in time with an exponent 0.3 resembling the value from the Lorentz model [102, 103]. Anomalous transport was even found in simulations for transport of small particles in a glassy, slowly rearranging matrix of large particles [272, 273]; although the MSD does not display unambiguous power-law behaviour, the apparent exponent $\alpha(t)$, defined by $\alpha(t) = d \log(\delta r^2(t)) / d \log(t)$, was found to be 0.5 and less over several decades in time [273], and there is evidence that the localisation scenarios in the binary mixture and the Lorentz model are related [277]. At high volume fractions of the obstacle matrix, all of the mentioned models share

non-vanishing non-ergodicity parameters due to trapped particles [100–103, 126, 273, 277] that would appear as immobile fraction in a FRAP experiment, see Section 4.3.

Aiming at a more realistic modelling, the measured distribution of protein sizes in the cytoplasm of HeLa cells served as input for a simple cytoplasm model consisting of 5000 spherical particles with exponentially distributed molecular weights [240]. The particles interact via a hard core plus a soft repulsive, parabolic potential; their overdamped motion was followed by Brownian dynamics simulations. The obtained MSDs display subdiffusion over 3 decades in time, where the exponent α decreases as function of the particle radius in a sigmoidal fashion from unity for the smallest particles (2 nm) to about 0.55 for the largest radii studied (5 nm). Thus, the excluded volume can, to a large extent, account for the experimentally observed subdiffusion in HeLa cells.

A step towards a realistic modelling of the *E. coli* bacterium was taken by McGuffee and Elcock [274], who developed an atomistically detailed model of its cytoplasm including 50 different types of macromolecules at physiological concentrations. For systems of 1000 macromolecules in total, Brownian dynamics simulations including electrostatic and hydrodynamic interactions yielded system trajec-

tories over 6 million steps or a time span of 15 μs . Thereby, molecular behaviour inside a cell is illustrated by vivid movies of educational value. Further, anomalous transport was observed over 4 decades in time with local MSD exponents $\alpha(t)$ between 0.75 and 0.85. Focusing on the role of excluded volume by including only repulsive interactions in the model, the anomaly was markedly reduced. Hence, the effects of macromolecular crowding extend beyond those of excluded volume, although a ramified excluded volume appears to be essential for pronounced subdiffusive motion.

The role of hydrodynamic interactions (HI) on protein motion was elucidated by Ando and Skolnick [271], who performed Brownian dynamics simulations of models for the *E. coli* cytoplasm comprised of 15 different macromolecule types: proteins were represented either by their molecular shape or by equivalent spheres of the same hydrodynamic radius, the particles interact non-specifically via a soft repulsive parabolic potential or via attractive van der Waals forces, and hydrodynamic interactions were included for the equivalent-spheres model. It was found that HI yield a 3- to 10-fold reduction of the *short-time* diffusion constants, depending on protein radius and concentration. This finding is supported by previous results for monodisperse spheres [269, 270] and corroborates recent experiments [266, 267], see above. Long-time diffusion constants were determined as function of the protein radius at an observation time scale of 5 μs and display a further reduction by a factor of 2 (with HI) or up to 20 (repulsion only). Notably, the equivalent-sphere model including HI reproduced the experimentally observed diffusion constant of GFP *in vivo* without any adjustable parameters. As a key result, excluded volume effects and hydrodynamic interactions are likely the two major factors for the large reduction in diffusion of macromolecules observed *in vivo*.

Echeverria and Kapral [275] studied the effect of crowding on the conformation and transport of a globular polymer in an explicit, albeit mesoscopic, poor solvent. The crowded environment was formed by a frozen, random array of hard spherical obstacles, and the system was propagated using the multi-particle collision dynamics (MPCD) scheme (which intrinsically includes hydrodynamic effects) for up to 1 million solvent particles. The simulation results show that the equilibrium structure of long polymer chains is significantly altered towards a chain of polymer blobs being trapped in voids between the obstacles. For increasing volume fraction of obstacles, subdiffusive motion of the centre of mass emerges with exponents α down to 0.7, and it appears that α decreases further as the polymer size increases. These findings are in accord with earlier lattice studies for polymers in disordered media [278–280], which showed that entropic trapping of the polymer in the voids leads to a stark slowing down of transport and to subdiffusive motion.

Transient binding to polymeric networks, e.g., in hydrogels, can render the transport of tracer molecules anoma-

lous as well as demonstrated by molecular dynamics simulations [276]. Strongly bound tracers sliding along a relaxed polymer strand exhibit pronounced subdiffusive motion with exponents $\alpha = 1/2$ or $3/5$, depending on the fractal structure of the coiled strands. For a swollen hydrogel, the polymer coils are stretched and the window of subdiffusion was found to decrease quickly. Further, there is a competition between sliding along the polymer and free diffusion within the pores of the network. The observed anomalous transport depends sensitively on the attraction strength between the tracer and the polymer chain, which governs this competition.

5.2. Crowded membranes

5.2.1. Cellular membranes (in vivo)

According to the “fluid mosaic” model by Singer and Nicolson [299], the plasma membrane of cells is thought of as an essentially homogeneous fluid bilayer of phospholipids with freely diffusing protein inclusions. Numerous *in vivo* measurements of protein motion in membranes during the past two decades, however, required several revisions of this simple picture. Today, the plasma membrane is considered a patchy lipid bilayer densely packed with integral and peripheral proteins, where some of the lipids are organised into microdomains, some of the proteins form clusters, and others are tethered to the cytoskeleton [19, 300, 301].

First hints on the heterogeneous landscape of the plasma membrane go back to early FRAP experiments [207, 295], indicating that a significant fraction of certain membrane proteins is immobile. These findings were corroborated by single-particle tracking techniques emerging in the 1990’s, which enabled the observation of individual fluorescently labelled membrane proteins [223, 281–283]. The dynamics of membrane receptors in mouse keratinocytes was found to be highly heterogeneous within the same type of protein, and the trajectories were classified after their MSDs into four types of motion: free diffusion, confined diffusion, immobile, and directed motion [281].

SPT experiments on IgE receptors by Feder *et al.* [223] yielded another class of MSDs, which required a subdiffusive power-law fit for 56% out of 241 trajectories (150 frames every 1.6 s) with an average exponent $\alpha = 0.64 \pm 0.45$; 27% of the receptors were immobile. The findings are consistent with corresponding FRAP measurements, see below. In similar experiments, Sheets *et al.* [282] preferred to account for the subdiffusive fraction by refining the classification of trajectories also according to their “shape” and by introducing the additional class of slow normal diffusion. For the Thy-1 protein, the classes of fast and slow diffusion yielded diffusion constants as different as 0.081 and 0.0035 $\mu\text{m}^2/\text{s}$, respectively.

Significant enhancement of the temporal resolution to 0.22 ms of the SPT experiments [283] provided a more detailed picture of band-3 protein transport in erythrocyte mem-

cell type (membrane)	probe	experimental technique	temporal and spatial scales	observation	year	reference
keratinocytes	E-cadherin and transferrin receptor	SPT, FRAP	33 ms–30 s	heterogeneous MSDs: free, confined, immobile, directed	1993	ref. 281
RBL cells	IgE receptor	SPT, FRAP	1–100 s	56% of tracers: subdiffusion with $\alpha = 0.65 \pm 0.45$; 27% immobile	1996	ref. 223
C3H 10T1/2 fibroblasts	Thy-1 protein	SPT	30 ms–1 s	normal diffusion, fast and slow components	1997	ref. 282
erythrocytes	band-3 protein	SPT	0.22 ms–1 s	$D_{10\text{ms}}/D_{1\text{s}} \approx 80-90$, 1/3 immobile	1998	ref. 283
rat kidney fibroblasts	DOPE phospholipid	SPT	25 μs –3 s	3 subdiffusion regimes (double crossover): $\alpha = 0.74 \rightarrow 0.55 \rightarrow 0.79$	2002	ref. 284
various cell types				subdiffusion @ 0.1–10 ms ($\alpha = 0.53$), short- and long-time diffusion: $D_0/D \approx 10$	2004	ref. 285
HeLa cells	MHC class I protein	SPT	4–300 s	subdiffusion: $\alpha = 0.49 \pm 0.16$	1999	ref. 286
CHO cells	MHC class II protein	SPT	100 ms–3 s	normal diffusion	2002	ref. 287
<i>C. crescentus</i>	PleC protein	SPT	1–9 s	normal: $D \approx 10^{-2} \mu\text{m}^2/\text{s}$	2004	ref. 288
COS-7 fibroblasts, MDCK cells	AQP-1 protein	SPT	10 ms–6 min	heterogeneous MSDs (free, restricted, immobile), normal case: D depends on protein content	2008	ref. 289
HEK 293 cells	Kv2.1 potassium channel	TIRFM	0.1–100 s	subdiffusion ($\alpha \approx 0.8$), ageing, fractal space, stationary and non-stationary displacements	2011	ref. 171
RBL cells	diI-C ₁₂ lipid	FCS	$\tau_{1/2} \approx 30$ ms	subdiffusion $\alpha = 0.74 \pm 0.08$, or two components: $D_1/D_2 = 30$	1999	ref. 290
oligodendroglia	MOG protein, sphingomyelin lipid	FCS	0.01–100 ms	subdiffusion of MOG protein ($\alpha = 0.59$), two-component diffusion of lipid	2005	ref. 291
HeLa cells (intracellular membranes)	Golgi-resident enzymes	FCS	0.3–100 ms	subdiffusion: $\alpha \approx 0.5-0.8$	2003	ref. 292
yeast cells	Fus-Mid-GFP protein	scanning FCS	$\tau_{1/2} \approx 2$ s	slow, normal diffusion: $D \approx 10^{-3} \mu\text{m}^2/\text{s}$	2006	ref. 293
COS-7 cells	transferrin receptor (TfR), sphingolipids, anchored proteins	variable-area FCS	beam waist: 190–390 nm	w -dependent effective D : $\tau_{1/2}(w) = t_0 + w^2/4D_{\text{eff}}$, $t_0 > 0$ for lipids and anchored proteins, $t_0 < 0$ for TfR	2005, 2006	refs. 181, 294
PtK2 cells	sphingomyelin, anchored protein	variable-area FCS	beam waist: 75–350 nm	3–5-fold reduction of $D(w)$ for small w	2007	ref. 185
PtK2 cells	sphingomyelin, anchored protein	STED-FCS	beam waist: 15–125 nm	anomalous w -dependence: $\tau_{1/2}(w \rightarrow 0) \approx 10$ ms	2009	ref. 189
rat myotubes	ACh receptor	FRAP	1 min	immobile fraction of ACh in dense patches	1976	ref. 207
human embryo fibroblasts	WGA receptor	FRAP	$\tau_{1/2} \approx 30$ s	only 75% mobile receptors	1976	ref. 209
thymocytes, lymphoma cells, fibroblasts	Thy-1 protein	FRAP	$\tau_{1/2} < 1$ s	$\approx 50\%$ immobile	1987	ref. 295
COS-7 cells	anchored, acylated, and transmembrane proteins	FRAP	bleaching stripe: 4 μm	normal, $D = 0.1-1.2 \mu\text{m}^2/\text{s}$ for different proteins	2004	ref. 296
	4 membrane proteins	FRAP	$\tau_{1/2} \approx 2$ s, spot radius: 3.6 μm	normal, but D 10-fold smaller than for GPI-proteins	2007	ref. 297
HEK 293T	CD4 and chemokine receptors	variable-radius FRAP	spot radius: 1.40–3.45 μm	D and recovery ratio depend on size of bleaching spot	2007	ref. 298

Table V. Overview of *in vivo* experiments on cellular membranes as guide to the discussion in Section 5.2.1. Empty fields repeat the entry above. Abbreviations: TIRFM... total internal reflection fluorescence microscopy, STED... stimulated emission depletion.

branes: a fraction of proteins was immobile, the remaining two thirds exhibited normal diffusion at macroscopic time scales of a few seconds. The diffusion constant, however, was drastically reduced by a factor of 80–90 compared to its microscopic value at 10 ms. Refined experiments suggested a hopping mechanism due to interaction with the spectrin network, characterised by a mesh size of 110 nm and an average hop frequency of 2.8 s^{-1} .

Some years later, the same lab implemented a high-speed SPT setup with a temporal resolution of remarkable $25 \mu\text{s}$ [284], which permitted the detailed tracking of DOPE phospholipids in rat kidney fibroblasts. The obtained MSD covers five(!) decades in time and exhibits two crossovers at 12 and 590 ms, connecting three regimes of motion (see supplement of Ref. 284). All three regimes are compatible with subdiffusive motion with exponents $\alpha = 0.74$ (short times), $\alpha = 0.55$ (intermediate times), and $\alpha = 0.79$ (long times, but regime covers less than a decade). Extrapolating to short time scales, the MSD appears to approach the free diffusion in a homogeneous lipid bilayer. It was concluded that the plasma membrane is doubly compartmentalised into 750 nm and then into 230 nm compartments with regard to the lateral diffusion of DOPE lipids. Repetition of the measurements for many other cell types [285] corroborated these findings qualitatively with hopping rates between 1 and 59 s^{-1} and compartment sizes between 30 and 230 nm. For FRSK cells (fetal rat skin keratinocytes), the regimes at short and long times exhibited essentially normal diffusion with diffusion constants separated by an order of magnitude; the intermediate regime between 0.1 ms and $\approx 10 \text{ ms}$ was found to be subdiffusive with exponent $\alpha = 0.53$.

On the basis of these observations, Kusumi *et al.* [19, 302] have proposed a revised model for the plasma membrane, which should be viewed as a compartmentalised fluid. The structure is provided by barriers or obstacles like the actin-based membrane skeleton (“fences”) and anchored transmembrane proteins (“pickets”). The motion of proteins and lipids is then thought of as a hopping process between differently sized membrane compartments, and transport is slowed down by such specific barriers.

Deeper insight into the stochastic transport process is expected from the investigation of displacement histograms for fixed lag times, i.e., the van Hove function. Such a route was taken by Smith *et al.* [286], who performed SPT experiments using fluorescence imaging of major histocompatibility complex (MHC) class I molecules on HeLa cells. Fitting the propagator of normal diffusion to the displacement histograms yielded the diffusion coefficients $D(t)$ as function of the observation time scale. A marked decrease of $D(t)$ with increasing time interval was found, and the data were best described by subdiffusive motion with $\alpha = 0.49 \pm 0.16$ over the whole accessible temporal window between 4 s and 300 s. Unfortunately, the histograms suffered from large statistical noise prohibiting

an answer to the question whether the distribution of displacements is gaussian or not.

The translational diffusion of MHC class II membrane proteins in Chinese hamster ovary cells was studied by Vrljic *et al.* [287] to probe the plasma membrane for barriers from putative lipid microdomains. Using SPT at a rate of 100 ms, the cumulative probability distribution function of displacements was extracted at time scales up to only a few seconds (limited by photobleaching). In this time window, however, almost negligible deviations from simple Brownian motion and no significant confinement could be inferred. Most notably, the authors also studied correlations in the transport of *close pairs of proteins*, initially separated between 0.3 and 1 μm . The idea was to detect a possible confinement by impermeable, but diffusing barriers. Again, the results followed the predictions of free diffusion and no evidence for a restriction to small, freely diffusing domains was found at the length scales under investigation.

Normal diffusion was also observed by tracking the transmembrane histidine kinase PleC in the bacterium *Caulobacter crescentus* [288], which yielded the relatively low value $D = 12 \times 10^{-3} \mu\text{m}^2/\text{s}$. The experimental MSDs, however, covered only a small time window between 1 and 9 s (due to limitations of the fluorescent label) and are subject to large statistical errors. Hence, the question whether transport is normal or anomalous could actually not be addressed. Further, transport was found to be spatially uniform across all positions in the elongated cell with exception of the cell poles and without evidence for active transport.

The impact of putative lipid microdomains on the motion of integral membrane protein aquaporin-1 (AQP-1) in COS-7 fibroblasts and Madin–Darby canine kidney cells was studied by long-time SPT experiments [289]. Labelling with quantum dots enabled the recording of long trajectories at 1 Hz over 6 min. Trajectories were classified into free, restricted, and immobile according to their deviation from the extrapolated short-time MSDs at 91 Hz. Most AQP-1 proteins diffused freely over several microns on the scale of minutes, and diffusion was faster by a factor of 4 in protein-poor membrane blebs. It was concluded that AQP-1 is a largely non-interacting protein with a macroscopic diffusion constant determined by the concentration of obstructions in the membrane.

Only recently, Weigel *et al.* [171, 303] investigated the dynamics of Kv2.1 potassium channels in the plasma membrane of human embryonic kidney (HEK 293) cells. Labelling with quantum dots and tracking by means of total internal reflection fluorescence microscopy (TIRFM) permitted the collection of 1000 trajectories each about 10 min long at temporal and spatial resolution of 50 ms and 8 nm, respectively. Scrutinising time- and time-ensemble-averaged MSDs, ageing behaviour, the propagator, and the distribution of waiting times indicated the coexistence of a non-stationary transport process compatible with a CTRW and a stationary walk in a fractal space.

The non-stationary process was attributed to binding of the potassium channels to the actin network, while the stationary process may have its origin in the molecular crowding of the membrane.

During the past decade, FCS has routinely been applied to cellular membranes for *in vivo* measurements of lipids and proteins. Introducing fluorescent lipid probes in the plasma membranes of rat basophilic leukaemia (RBL) cells, Schwille *et al.* [290] obtained FCS correlations which clearly deviate from normal diffusion. The data can be described by the gaussian subdiffusion model with $\alpha = 0.74 \pm 0.08$ and half-value times around 30 ms, or alternatively well, by the two-component diffusion model yielding diffusion times of 3 ms and 100 ms. A control experiment with giant unilamellar vesicles (GUVs) showed normal diffusion, but inducing phase separation of the lipid mixture by adding cholesterol rendered the lipid transport anomalous again.

For myelin oligodendrocyte glycoproteins bound to oligodendrocyte membranes, anomalous diffusion with $\alpha = 0.59$ was reported [291], while a two-component diffusion model appeared to be less likely. The results for sphingomyelin lipids in the same membrane suggest a two-component description with diffusion constants of 0.37 and $70 \mu\text{m}^2/\text{s}$; here, a possible explanation for the highly mobile fraction are dye molecules moving freely in solution.

Intracellular membranes were addressed by Weiss *et al.* [292], who monitored three Golgi-resident enzymes both in the endoplasmic reticulum and in the Golgi apparatus of HeLa cells. Subdiffusive motion was found over more than two decades in time with half-value times of 10–30 ms and with exponents α that depend on the type of enzyme and range between 0.5 and 0.8; for the same enzyme, similar values of α were obtained in the two different membrane structures. The data can be equally well fitted by the two-component diffusion model, but it was argued that such a fit seems unlikely.

A modification of the FCS technique is *scanning FCS* [304], where the illumination laser repeatedly scans the probe, e.g., along a large circle. The same spot is visited with a low frequency, giving access to the fluorophore dynamics at very long time scales. Combining this method with continuous wave excitation, very slow, albeit normal diffusion was observed for Fus-Mid-GFP proteins on yeast cell membranes [293], with diffusion constants on the order of $10^{-3} \mu\text{m}^2/\text{s}$ and FCS diffusion times of up to 2 seconds. Compared to the motion of these slow proteins, the other membrane components rearrange quickly, effectively homogenising the originally heterogeneous environment of the protein. This may explain the finding of simple diffusion at long times, resolving an apparent contradiction with the measurements quoted above. The example further highlights the importance of taking into account the experimental time and length scales for the interpretation of transport in complex environments.

Complementary to the previous FCS studies, the spatial as-

pects of complex molecular transport in membranes were explicitly addressed by systematic variation of the detection area. Using beam waists ranging from 190 to 390 nm, Wawrezynieck *et al.* [181] have measured the motion of the GFP-labelled transmembrane protein TfR (transferrin receptor) and of a sphingolipid in the plasma membrane of COS-7 cells. The obtained two sets of diffusion times exhibit an affine dependence on w^2 motivating the FCS diffusion law, $\tau_d(w) = t_0 + w^2/4D_{\text{eff}}$. Extrapolation to zero beam waist yields the axis intercepts t_0 , which were found to be +25 ms for the lipids and –20 ms in case of the TfR proteins, with uncertainty of 10%. The signs of t_0 can give a hint on the transport mechanism, and it was concluded that the motion of sphingolipids is hindered by isolated microdomains and those of the TfR proteins by a meshwork of barriers. Alternatively, the protein diffusion times may be interpreted in terms of fractal scaling law $\tau_d(w) \sim w^{2.6}$ according to Eq. (95), indicating subdiffusion with $\alpha = 2/d_w \approx 0.77$ [23]. The findings of Ref. 181 were substantiated by further experiments with a variety of molecules [294], providing a broad range of intercept values: sphingolipids and GPI-anchored proteins yielded clearly positive t_0 , the transmembrane TfR-GFP is characterised by a strongly negative value, and the axis intercept vanished for glycerophospholipid analogues. In conclusion, the slow dynamics of sphingolipids is attributed to cholesterol and sphingomyelin levels in the membrane, and the transferrin receptor protein is likely to be dynamically confined by actin-based cytoskeleton barriers.

It is clear from Eq. (90) that the diffusion time must vanish as the observation area approaches zero. Thus, the extrapolation $w \rightarrow 0$ of the above diffusion law can only hold approximately, and it is of interest to elucidate the behaviour at small w , below the diffraction limit. Observation areas with radii ranging down to 75 nm were achieved by equipping the microscope coverslips with circular nanometric apertures in a metallic film [185]. This approach permitted the elucidation of nanometric membrane heterogeneity and a considerable extension of the measured diffusion laws $\tau_d(w)$ of Ref. 294, revealing non-trivial crossovers. For ganglioside lipid analogues and GPI-anchored GFP in the plasma membrane of COS-7 cells, the apparent, w -dependent diffusion constants $w^2/4\tau_d(w)$ at short scales are 5- and 3-fold reduced compared to their large-scale values, with a crossover length scale of $w \approx 100$ nm. Even more interestingly, the diffusion law of TfR-GFP shows two transitions around 150 and 230 nm; the latter transition is explained by a meshwork of cytoskeletal barriers hindering transport of the transmembrane protein.

Application of STED-FCS to the plasma membrane of living mammalian cells gives access to nanosized detection areas down to $w = 15$ nm in radius [189]. Phosphoethanolamine molecules, which are assumed not to form molecular complexes with membrane components, exhibited free diffusion, $\tau_d(w) \propto w^2$, over the full range of investigated areas. The diffusion of sphingomyelin, however, was found to be strongly

heterogeneous: only for large radii, $w > 80$ nm, unobstructed, normal transport was found. For small detection areas, $w < 40$ nm, the FCS correlations showed clear deviations from normal diffusion. Fits with the subdiffusion model yielded $\alpha \lesssim 0.7$, but an explanation of the transport in terms of two diffusive components was favoured. The fast fraction resembled the unobstructed transport of phosphoethanolamine, both in space and time. The diffusion times of the slow fraction approached a minimum of about 10 ms for small areas. This offset was explained by a brief trapping event of that duration by cholesterol-mediated complexes within an area of less than 20 nm in diameter. Similar findings were made for GPI-anchored proteins.

The first applications of fluorescence recovery after photobleaching (FRAP) on plasma membranes addressed the lateral motion of fluorescently marked receptor proteins in rat myotubes [207] and human embryo fibroblasts [209]. In both experiments, only about 75% of the initial fluorescence was recovered indicating that a significant fraction of receptors is immobile. Similarly, the fluorescence recovery was found to be only about 50% for labelled Thy-1 antigen in the plasma membrane of lymphoid cells and different fibroblasts [295]. The obtained diffusion constant of the mobile fraction of Thy-1 proteins was comparable to those of the lipid analogues in the bilayer, which is consistent with a putative lipid anchoring to the plasma membrane. Feder *et al.* [223] studied the motion of IgE receptors in the membrane of leukocytes using SPT and FRAP. Motivated by the SPT measurements, they suggested a gaussian subdiffusion model for the analysis of the FRAP curves. The given data sets were fitted equally well by the subdiffusion model and the diffusion model with incomplete recovery, a fit to a combined model yielded a recovery of 90% and a subdiffusion exponent $\alpha \approx 0.6$. It was shown how subdiffusion could be discriminated from an immobile fraction if the recovery curves would span a much larger time window.

In contrast, almost complete recovery of fluorescence was found in FRAP experiments on the plasma membrane of COS-7 cells for a variety of putative raft and non-raft proteins [296]. The recovery curves from bleaching a large, 4 μm wide stripe were rationalised with normal diffusion, yielding diffusion constants between 0.1 and 1.2 $\mu\text{m}^2/\text{s}$ for the different proteins. These values appear to be mainly determined by the type of anchorage, since they change uniformly upon perturbing the membrane by variation of the cholesterol level or temperature.

In another FRAP study on four different membrane proteins expressed in COS-7 cells [297], it was found that transport over micron-scale distances is normal with 80–90% fluorescence recovery. The diffusion constants, obtained from fitting a single exponential to the recovery data, are in agreement with other *in vivo* measurements, but are an order of magnitude smaller than those of GPI-linked proteins reconstituted into liposomes [297]. The diffusion constants of the membrane proteins were unaffected by manipulations of the cor-

tical cytoskeleton, but they increased markedly (up to 3-fold) if the protein density in the membrane was reduced in semi-intact cells. In conclusion, the reduced mobility of membrane proteins is likely a consequence of the crowdedness of cellular membranes leading to anomalous transport on smaller time and length scales than accessible by a typical FRAP setup.

Baker *et al.* [298] employed FRAP experiments with a variable radius of the observation spot (vrFRAP) to address the distribution and transport of CD4 proteins and chemokine receptors on the plasma membrane of living HEK 293T cells. The obtained ratio of incomplete fluorescence recovery and the apparent diffusion constants depends sensitively on the radius, which was varied between 1.40 and 3.45 μm . Interpretation of this dependency allowed for the conclusion that proteins and receptors are compartmentalised into domains of about 350 nm.

5.2.2. Model membranes (in vitro)

Model membranes reduce the complexity of cellular membranes and permit a detailed study of macromolecular transport under controlled lipid composition and crowding conditions, vital for a physical understanding of anomalous transport. Membranes are usually modelled by bilayers of phospholipids, either supported by a flat substrate or forming a giant unilamellar vesicle. The structure of the lipid bilayer can be modified by addition of another lipid type, and crowding effects can be mimicked by covering the bilayer with anchored proteins or by introducing protein inclusions. It is possible to fluorescently label lipids as well as proteins and to follow their motion individually.

Schütz *et al.* [169] performed SPT experiments on a supported POPC lipid bilayer modelling a fluid membrane, where highly diluted fluorescent TRITC-DHPE lipids were introduced in the outer leaf. It was found that 69% of the labelled lipids showed normal, free diffusion with $D = 4.4 \mu\text{m}^2/\text{s}$, while the motion of the remaining part was still diffusive, although suppressed by a factor of 63. These results rely on the analysis of the cumulative probability distribution of the square displacements for a series of large times (from 20 ms to 300 ms), an approach that is well suited to identify and account for a mixture of fast and slowly diffusing molecules. The data for the slow fraction indicate further that motion is confined at short times below 100 ms, which the authors interpreted as evidence for corrals of about 130 nm size after correcting for the tracking uncertainty.

A systematic development of anomalous diffusion was observed in a supported bilayer using SOPC lipids where the motion of the monitored TRITC-DHPE lipids was hindered by essentially immobile “obstacles” [170], the obstacles were realised by lipopolymers in the inner leaflet tethered to the substrate. Similarly as in Ref. 169, the distribution of squared displacements was analysed for a fixed lag time of 50 ms. At obstacle concentrations below 10 mol%, the distribution

model membrane (composition)	probe (size)	experimental technique	temporal and spatial scales	observation	year	reference
SLB (POPC)	DHPE lipid	SPT	20–300 ms	normal, two components: $D_1 = 4.4 \mu\text{m}^2/\text{s}$, $D_2 = D_1/63$	1997	ref. 169
SLB (SOPC) + tethered lipopolymer (“obstacles”)	DHPE lipid, bacteriorhodopsin	SPT	$t_{\text{lag}} = 50$ ms	anomalous diffusion, $D \downarrow$ linearly for [lipopolymer] \uparrow	2005	ref. 170
SLB (DOPC/cholesterol)	DHPE lipid	FCS	beam radius: 0.25 μm	D : 4.2 \rightarrow 0.5 $\mu\text{m}^2/\text{s}$ for [cholesterol] \uparrow , deviations from simple diffusion	2003	ref. 305
multilamellar vesicles (DMPC/DSPC)	DPPE lipid	FCS	$\tau_{1/2}$: 108–230 ms	two-component diffusion for fluid–gel coexistence in bilayer, heterogeneous structures	2005	ref. 306
	C5-Bodipy-PC	variable-waist FCS	$\tau_{1/2}$: 1 – 150 ms w : 210–300 nm	w -dependent diffusion constant: $\tau_{1/2}(w) = t_0 + w^2/4D_{\text{eff}}$, $t_0 < 0$ in gel phase	2011	ref. 307
multibilayers (DMPC/cholesterol)	phospholipid	FRAP	spot radius: 4 μm	normal diffusion, D 2-fold reduced for [cholesterol] \uparrow	1992	ref. 308
GUV (DOPC/DOPG) + proteins	integral membrane proteins (0.5–4 nm)	FCS	$\tau_{1/2} \approx 2$ ms	$D \downarrow$ for [protein] \uparrow , max. 2-fold suppression, subdiffusion: $\alpha \gtrsim 0.88$	2009	ref. 309
SLB (SOPC) + avidin	DPPE-anchored avidin protein	FCS	t_{lag} : 0.3–300 ms, $w \approx 0.17 \mu\text{m}$	development of subdiffusion, α : 1 \rightarrow 0.68 for [avidin] \uparrow , spatial heterogeneity, no ageing	2010	ref. 191
SLB (SOPC) + neutravidin	lipid, DOPE-anchored neutravidin protein	FRAP	$\tau_{1/2} \approx 3$ s	normal diffusion, D_{protein} up to 7-fold suppressed, D_{lipid} almost unchanged as [neutravidin] \uparrow	2009	ref. 310

Table VI. Overview of *in vitro* experiments on model membranes as guide to the discussion in Section 5.2.2. Empty fields repeat the entry above, up/down arrows indicate increase/decrease of some quantity. Abbreviations: SLB... supported lipid bilayer, GUV... giant unilamellar vesicle, [X]... concentration of X.

histograms at this time scale correspond to normal diffusion and become increasingly anomalous for larger concentrations. The apparent diffusion constant $\langle \Delta \mathbf{R}^2 \rangle / 4t_{\text{lag}}$ is linearly suppressed with increasing obstacle concentration and vanishes near 40 mol%. The scenario is consistently described by random walks on two-dimensional lattice percolation clusters, see Refs. [50, 107] and Section 3.3. Similar results were obtained for the transport of diluted bacteriorhodopsin inclusions mimicking membrane proteins. The work demonstrates the great potential of model systems systematically bridging between physics and biology.

The influence of cholesterol content on the transport in planar DOPC bilayers supported by an atomically flat mica substrate was studied by FCS of rhodamine-labelled DHPE tracers [305]. The diffusion constant of DHPE reduces from 4.2 to 0.5 $\mu\text{m}^2/\text{s}$ as up to 60% of DOPC is replaced by cholesterol. Deviations from normal diffusion arise for a cholesterol content of 30% and more. While the data are fitted by the model with two normally diffusing components, the diffusion constant of the fast component is much larger than without cholesterol. Thus, the two-component model may not be suitable for DOPC/cholesterol bilayers.

Aiming at the reduction of coupling effects with the sub-

strate, Hac *et al.* [306] studied multilamellar model membranes consisting of stacks of about 50 layers. The bilayers are composed of a mixture of DMPC and DSPC lipids, which exhibits phase separation and a fluid–gel transition in each component. The motion of fluorescent TRITC-DPPE tracer lipids was followed by FCS at different compositions and temperatures covering the full region of fluid–gel coexistence in the phase diagram. While transport is normal in the fluid regimes, complex transport emerges in the phase-separated regime with its heterogeneous structure. The FCS correlations can be fitted by a two-component model, but again, the obtained diffusion times deviate from the ones in the pure fluid and gel phases. Instead of relying on a phenomenological fit model, the authors performed extensive Monte-Carlo simulations which quantitatively describe the experimental FCS curves; a detailed discussion of the simulations will be given in Section 5.2.3.

In a recent FCS experiment using the same DMPC/DSPC mixture [307], spatio-temporal information on the lipid motion was collected by variation of the detection area. FCS correlation functions were fitted by the model for normal diffusion yielding the half-value times as function of the area, which were analysed in terms of the so-called FCS diffusion law, i.e., $\tau_{1/2}(w) = t_0 + w^2/4D_{\text{eff}}$. In the fluid phase of the mixture, the dependence on w^2 is linear ($t_0 = 0$) as expected for simple dif-

fusion. Extrapolating to zero area, a negative offset, $t_0 < 0$, develops as the fluid–gel coexistence is traversed by lowering the temperature. Such a negative offset typically arises for motion in a meshwork of permeable barriers [194], but there, transport is not subdiffusive in the time domain. For motion in a phase-separating lipid mixture, Monte-Carlo simulations show that the area $4D_{\text{eff}}t_0$ correlates with the typical domain size of the spatially heterogeneous environment, demonstrating that a domain size may be extracted from FCS experiments [307]. The connection between the half-value times of the FCS correlation and the detection area may alternatively be described by a power law (see supplement of Ref. 307), $\tau_{1/2}(w) \sim w^{2/\alpha}$, yielding exponents α between 0.5 and 1; the smallest values are realised for temperatures close to the phase boundaries.

The lateral diffusion of a phospholipid probe was measured with FRAP in multi-bilayers of DMPC/cholesterol mixtures, exploring a large part of the phase diagram in the composition–temperature plane [308]. In all cases, the fluorescence recovery was complete and the uniform disc model for free diffusion, Eq. (114), fitted the data. A 2-fold reduction of the diffusion constant was observed as cholesterol content was increased from 0% to 50%, and the diffusivity increased up to 8-fold as the temperature was changed from 24 °C to 58 °C.

The lateral mobility of fluorescently labelled integral membrane proteins reconstituted in giant unilamellar vesicles (GUVs) of a DOPC/DOPG mixture was measured using FCS [309]. The hydrodynamic radius of the investigated proteins ranged between 0.5 and 4 nm. Consistent with the Saffman–Delbrück model, the diffusion coefficient at low protein content displays a weak, i.e., logarithmic, dependence on the radius. The diffusion coefficient of proteins and lipids decreases linearly with increasing the protein concentration in the membrane up to 3000 proteins per μm^2 . Such a concentration is an order of magnitude smaller than in biological membranes and induces only small crowding effects. Hence, the observed reduction of mobility did not exceed about 20% for the lipids and was at most 2-fold for the proteins; deviations from simple diffusion were only moderate with the exponent of subdiffusion α not falling below 0.88.

Crowding by peripheral membrane proteins was addressed by a study of avidin proteins irreversibly bound to biotinylated DPPE lipid anchors in a supported single SOPC lipid bilayer [191, 311]. The content of lipid anchors in the bilayer directly controls its protein coverage. X-ray reflectivity experiments showed that the protein layer is separated from the lipids by a distinct water layer, and continuous bleaching experiments indicated that the fluidity of the lipid bilayer is retained even at high protein coverage [311]. Upon increasing the protein coverage, FCS measurements on dilute labelled avidin proteins revealed a systematic development of anomalous transport [191]. Converting the FCS correlation to the mean-square displacement via Eq. (91b), subdiffusive mo-

tion was observed over a time window spanning from 0.3 to 300 ms. The exponent α decreases gradually from 1 to 0.68 in the most crowded regime with an excess of biotin anchors. The onset of anomalous transport occurs already at an anchor concentration of 0.1 mol% or an area coverage of 3–5%. This transition regime is characterised by a pronounced and long-lived spatial heterogeneity: different exponents α were reproducibly obtained at different spots of the sample. The distribution of exponents becomes bimodal as crowding is increased; some spots exhibit simple diffusion of the proteins, while an increasing fraction displays subdiffusion. On the time scale of hours, ageing effects could not be detected.

FRAP measurements on similar SOPC bilayers crowded with neutravidin [310] corroborate normal diffusion of the lipids with slightly reduced diffusion constants by up to 25% at the highest protein coverage, a fraction of about 10% of the lipids was detected to be immobile. Covering the bilayer with fluorescently labelled neutravidin, the fluorescent signal from the proteins did not recover on the time scales of the experiment, which was attributed to proteins being arrested in a kind of gel phase. Measuring protein transport by means of continuous bleaching, a 7-fold slowing down was observed at the highest protein coverage, which may be compatible with the findings in Ref. 191 taking the different time and length scales of the experiments into consideration.

5.2.3. Computer simulations (in silico)

Obstructed motion

In his seminal works, Saxton [87, 312] introduced a minimalist model for transport in cellular membranes. The positions of lipids and proteins are restricted to a two-dimensional lattice for computational efficiency; tracer molecules perform a random walk which is hindered by randomly distributed obstacles occupying a single lattice site each. In the limiting case of immobile obstacles, the obtained diffusion constants are almost linearly suppressed with increasing obstacle area and vanish at the percolation threshold [312]. While the sharp localisation transition disappears if the obstacles themselves are allowed to diffuse slowly, the systematic reduction of tracer mobility with increasing obstacle concentration is conserved. For immobile obstacles [87], the MSD displays subdiffusive motion over a growing time window and a crossover to normal diffusion at large time scales. The apparent exponents α obtained from the intermediate subdiffusive regime depend on the obstacle concentration and approach their universal value only at the percolation threshold. The concentration-dependence of the exponent was reconciled with the dynamic scaling hypothesis only recently by including the leading corrections to scaling, which are again universal [116]; see Section 3.3.4 for a detailed discussion.

The spatial discreteness of lattice models is overcome by continuum models, where the obstacles are usually imple-

space	crowded medium	tracer	interactions	observation	year	reference
square lattice	point obstacles (mobile, but slow)	point	excluded volume	$D \downarrow$ for [obstacle] \uparrow	1987	ref. 312
	point obstacles (fixed, random)			subdiffusion on growing time window, $D \downarrow$ linearly and $\alpha \downarrow$ for [obstacle] \uparrow , at percolation transition: $D = 0$, $\alpha \approx 0.68$	1994	ref. 87
				dynamic scaling for cluster-resolved MSDs, universality of exponents	2008	ref. 116
2D continuum	random disc obstacles	discs	hard core repulsion	transient subdiffusion, $\alpha \downarrow$ for [obstacle] \uparrow , highly fragmented void space	2006, 2008	refs. 83, 84
	random disc obstacles (overlapping)	point	hard core repulsion	universal scaling of localisation phenomenology, subdiffusion over 6 decades in time, $\alpha: 1 \rightarrow 0.659 \rightarrow 0$	2010	ref. 22
square lattice	extended obstacles from AFM images	point	excluded volume	subdiffusion, $\alpha: 1 \rightarrow 0.59$ as excluded area \uparrow , agreement with experiments	2011	ref. 313
	mobile “rafts”, point and line obstacles (“fences”)	point	excluded volume, low mobility inside rafts	subdiffusion ($\alpha \approx 0.7$) only for immobile rafts and raft-excluded tracers	2007	ref. 314
	regular network of line obstacles (“fences”)	point	potential barrier	high and dense barriers reduce $D(t)$ by several orders of magnitude	2008	ref. 315
triangular lattice	DMPC/DSPC monolayer model (2 sites per lipid)	lipid	nearest neighbour, slow and fast hopping, fluid/gel state flips	FCS correlation: subdiffusion ($\alpha \geq 0.63$), agreement with experiment	2005	ref. 306
				subdiffusion ($\alpha: 1-0.6$) from first passage times, structural heterogeneity	2005	ref. 316
				FCS with variable beam waist: $\tau_{1/2}(w) \sim w^{2/\alpha}$, $\alpha: 1-0.5$	2011	ref. 307
square lattice	DMPC/DSPC monolayer model (1 site per lipid)	point		transient subdiffusion, $\alpha \approx 0.85$ close to critical point	2011	ref. 317
			+ heterogeneous sticky network	transient subdiffusion ($\alpha \approx 0.5$), D_0/D up to 10	2011	ref. 318
3D continuum	atomistic DOPC bilayer (288 fully hydrated lipids)	lipid	molecular force fields	lipid transport at 1 ps is correlated over distances of 2.5 nm	2009	ref. 319

Table VII. Overview of computer simulations on crowded membranes as guide to the discussion in Section 5.2.3. Empty fields repeat the entry above, up/down arrows indicate increase/decrease of some quantity.

mented by a simple geometric shape. Sung and Yethiraj [83, 84] investigated the motion of tracer discs in a frozen obstacle matrix of randomly placed, non-overlapping, impenetrable discs; the limit of dilute tracers is known as non-overlapping Lorentz model in the literature [320]. Similarly as for the lattice model, transport slows down with increasing obstacle concentration and subdiffusive motion emerges in an intermediate time window. A Voronoi map of the continuous space accessible to the tracer particles reveals that the free space is highly fragmented into voids of different sizes, which are connected by significantly correlated channels. Thus at high obstacle concentration, the primary mode of transport resembles a hopping motion between neighbouring voids; similar observations were reported from particle tracking experiments [285]. Transport on large scales, however, is the result of a large number of hopping events, and subdiffusive motion relies on the presence of a spacious and self-similar network of connected channels meandering the membrane.

The full dynamic scaling picture of anomalous transport

due to a localisation transition was established only recently for two-dimensional continuum models [22]. Extensive simulations for a Brownian tracer between uncorrelated and overlapping circular obstacles confirmed the universal values of the dynamic exponents at leading and next-to-leading order, e.g., for the exponent of subdiffusion $\alpha = 2/z \approx 0.659$ if also tracers in isolated regions (“finite clusters”) are included. The subdiffusive motion was followed over six decades in time, and the crossover to normal diffusion away from the localisation transition was found to extend over several decades as well. Further, the transport dynamics was rationalised in terms of crossover time and length scales, which diverge at the transition. Appropriate rescaling of the time-dependent diffusion constants for different obstacle concentrations yielded data collapse onto a universal scaling function that describes the crossover from subdiffusion to normal diffusion. The transition to continuum models is a step towards a more realistic modelling, the universal phenomenology of the localisation transition, however, is preserved as expected at sufficiently

large scales. This is in contrast to obstructed transport in three dimensions, where lattice and continuum models belong to different (dynamic) universality classes with different transport exponents [114, 115, 117].

An uncorrelated distribution of obstacles, generated by a random process, is certainly a simplification. Realistic configurations of the excluded area were obtained from atomic force microscopy (AFM) imaging of phase-separating lipid bilayers [313]. For mixtures of DSPC/DOPC lipids, the gel-like DSPC-rich phase effectively provides an excluded area to the motion of DMPE tracer lipids. The rastered AFM images then yield “obstacles” of irregular shape that extend over many lattice sites, and Monte-Carlo simulations can be used to investigate the transport of the tracer lipids performing a random walk in the remaining space. This approach is somewhere in between the original lattice models and the continuum models, and if it is justified that the macroscopic transport is not affected by the imaging resolution (cf. Ref. 315) it can provide a quantitative bridge to the experiments.

Apart from excluded volume, transport of membrane proteins may be hindered by other sources. Nicolau *et al.* [314] studied random walks of proteins on two-dimensional lattice models, where the proteins are hindered by either a regular lattice of cytoskeletal fence posts or by mobile lipid rafts that are either impenetrable for proteins or reduce their mobility. Appreciable subdiffusion similarly as for randomly distributed, fixed obstacles was only observed if the protein motion is hindered by almost immobile, impenetrable rafts. Depending on the raft mobility, subdiffusive motion was characterised by exponents α between 0.65 and 0.75. The simulations indicated further that collisions with fence lines alone (without binding) do not explain the experimentally reported degrees of anomalous transport. Fences that impose very high barriers, however, can reduce protein diffusion at long times by several orders of magnitude [315], which was demonstrated by Monte-Carlo simulations on a lattice compartmentalised by a regular network of fences. It appears that here a plateau in the MSDs rather than a subdiffusive power-law growth is the manifestation of slow transport. Since only a single length scale characterises the regular super-lattice of fences, the plateau can be understood as a reflection of the mesh size.

Mixtures of DMPC/DSPC lipids

Experiments on lipid transport in artificial lipid bilayers have shown that anomalous transport emerges as function of the lipid composition. Often binary mixtures of lipids like DMPC/DSPC or DOPC/cholesterol were used, which can phase separate into fluid- and gel-like domains. Sugár *et al.* [321] developed a model for DMPC/DSPC mixtures on a triangular lattice, where each of the two acyl chains of a lipid occupy two adjacent sites and each site is in either the gel or the fluid state. The thermodynamics of the model is governed by a Hamiltonian with 10 relevant parameters, which were either

directly inferred from calorimetric measurements or estimated by means of Monte Carlo simulations to reproduce the correct phase diagram.

Relying on this model, Hac *et al.* [306] investigated FCS correlation functions of the lipids using Monte-Carlo simulations with a coarse-grained dynamics. Each lattice update allowed for the possibility of flipping the gel/fluid state of a lipid chain (Glauber dynamics) and of exchanging adjacent molecules mimicking diffusion (Kawasaki dynamics). The dynamics is controlled by a rate for the state flips and two hopping rates for fluid- and gel-like environment; the latter two were matched to the experimental diffusion constants for pure fluid or gel phases. The numerically obtained FCS curves show quantitative agreement with the experimental results if the flip rate is chosen close to the hopping rate in the fluid. In the regime of gel–fluid coexistence, the FCS curves deviate from normal diffusion and are fitted by the gaussian subdiffusion model. The exponent α depends on the flip rate, and its smallest value of 0.63 was reported for pure Kawasaki dynamics, i.e., in the absence of artificial state flips. Parameters for the hopping rates may be obtained by free volume theory, and correlating the structure and distribution of gel clusters with the lipid dynamics provides evidence that the anomalous transport arises from molecules exploring a heterogeneous environment [316]. The model was further employed to address spatial aspects of the lipid transport by simulating FCS correlations for a wide range of beam waists, which allowed for the extraction of the mean domain size [307]; a discussion was already given in Section 5.2.2.

The above lattice model for a lipid membrane of Refs. 321 and 306 was further simplified by Ehrig *et al.* [317, 318]. They used a square lattice with each site representing a lipid molecule; the coarse-grained dynamics still comprises state flips of a single lipid and diffusion by exchange of two adjacent sites. Together with advances in computer hardware, this permitted the investigation of comparably large systems with a membrane area of $(0.48 \mu\text{m})^2$ or 600^2 lattice points and processes on time scales of up to 1 s. The simulations demonstrate that close to the upper critical point of fluid–gel coexistence, the lipid motion exhibits anomalous transport over several decades in time. A double-crossover scenario is observed from simple diffusion at microscopically short time scales to transient subdiffusion and finally back to normal diffusion. The time window of subdiffusion increases as the critical point is approached, the local exponent $\alpha(t)$ of the MSD, however, does not yet display a plateau and its smallest reported value is around 0.85 being still relatively close to 1. In consequence, only a 3-fold suppression of the macroscopic diffusion constant is observed compared to its microscopic value. The introduction of a frozen, spatial heterogeneity in form of a sticky network [317] renders the lipid transport significantly more anomalous in a limited time window and induces an up to 10-fold reduction of mobility and minimal values of the local ex-

ponent $\alpha(t)$ down to 0.5.

Let us raise the question whether an asymptotic, universal value for the subdiffusion exponent exists in a mixture as the critical point is approached further. The analytical work by Kawasaki [322], employing a local-equilibrium approximation, suggests that the self-diffusion constant is only mildly affected by the critical fluctuations; in particular, it is not singular at leading order and does not vanish. Similarly, recent microcanonical molecular dynamics simulations for a three-dimensional symmetric binary mixture near its consolute point revealed almost negligible anomalies in the single-particle transport [323, 324]. It appears that in two dimensions, the single-particle transport is coupled more strongly to the critical fluctuations. But it is unlikely that subdiffusion can exist over an arbitrarily large time window, which would imply a vanishing diffusion constant.

With constantly growing computational resources, atomistic molecular dynamics simulations may come into reach as an alternative source for the parameters of coarse-grained models. A detailed view of the structure of a DMPC/DSPC bilayer was provided by a hybrid simulation technique, where an atomistic molecular dynamics simulation was supplemented by a semi-grandcanonical Monte-Carlo step converting a DMPC lipid into DSPC and *vice versa* [325]. Using 128 lipid molecules and 3200 explicit point charge water molecules, it was possible to generate system trajectories covering 50 ns in time, or two million integration steps. By means of a pure molecular dynamics simulation for a bilayer of 288 atomistically modelled DOPC lipids, the experimental values of the short-time diffusion constants of the lipids could be quantitatively reproduced by a simulation [319]. The study further showed that the motion of the lipids is correlated over distances of about 2.5 nm at the time scale of 1 ps, which is a useful piece of information for the refinement of lattice models: it suggests that a single lattice site should represent a correlated area of several lipids rather than a single lipid molecule or chain. Molecular dynamics simulations of lipid transport over large distances seem not yet feasible as it would be hampered by the small diffusion constant of the lipids in the gel state ($D_{\text{gel}} \approx 0.05 \text{ nm}^2/\mu\text{s}$ [306]). This emphasises the need of controlled coarse-graining and multiscale approaches for the study of slow, complex relaxation dynamics at the micro- and millisecond scale.

5.3. Reaction kinetics

So far, we have discussed the anomalous transport of individual macromolecules in their crowded cellular environments. Physiological processes, however, are determined to a large extent by biochemical reactions. Adding to the complexity of anomalous transport, the reaction rates as well as the availability of reactants are significantly modified by molecular crowding. The systematic investigation of this topic is relatively young, and we will only sketch some of the recent findings.

Minton *et al.* [227, 326] considered the consequences of macromolecular crowding on the equilibrium rates of biochemical reactions from a thermodynamics point of view, focusing on changes of the excluded volume. They found a non-specific enhancement of reaction rates if the total excluded volume is reduced; examples for such reactions are the formation of macromolecular complexes in solution, binding of macromolecules to surface sites, formation of insoluble aggregates, and compaction or folding of proteins. For protein association reactions, crowding is generally expected to increase the rate of slow, transition-state-limited reactions and to decrease the rate of fast, diffusion-limited ones. In the context of polymer systems, it was predicted that the subdiffusion exponent controls the crossover between reaction- and diffusion-limited kinetic regimes [327]. A variation of the association rates under crowding conditions by an order of magnitude was reported in the experimental literature reviewed until 2008 in Refs. 227 and 326. Melo and Martins [328] reviewed the kinetics of bimolecular reactions in model bilayers and biological membranes from an experimental perspective until 2006; their conclusion “When going to crowded or phase-separated systems ... the absence of experimental studies is almost complete.” emphasises the need for systematic investigation of the reaction kinetics in crowded membranes.

The kinetics of the reaction $A + B \rightarrow \text{products}$ on a percolating, two-dimensional lattice was studied using Monte-Carlo simulations [329]. Subdiffusive motion slows down the initial encounter of reactants, but concomitantly hinders them from escaping due to the increased return probability. The simulations showed that obstructions can slightly increase the reaction rate if the reaction probability on a single encounter is small. On the other hand, the reaction rate is reduced for high reaction probability, and taken together, subdiffusion of the reactants narrows the range of reaction rates. The bimolecular reaction is similar to that of the reaction of a random walker with an immobile target. Realising anomalous transport of the walker by a hierarchy of non-reactive binding sites, Saxton [330] found from simulations that trapping may contribute significantly to the noise in reaction rates and further that the subdiffusive motion yields a power-law distribution of capture times. Schmit *et al.* [331] identified the concentration of reactants and the crowdedness of the medium as two antagonistic parameters for the rates of diffusion-limited bimolecular reactions. They showed that there is an optimal reaction rate (for a fixed ratio of the concentrations of reacting and inert particles) if the reactants are not too diluted and if the medium is not too crowded, i.e., diffusion of the reactants is not too slow. Continuum models for the reaction of ligands with an immobile receptor realised the crowded environment by a dense hard-sphere fluid [332, 333]. Again, a non-monotonic dependence of the effective reaction rate on the volume fraction of the fluid particles was found for sufficiently small receptors.

For a diffusion-limited dimerisation reaction in a computer

model for the *E. coli* cytosol [334], it was observed that the reaction coefficients become time-dependent in the presence of anomalous transport; the obtained reaction rate was suppressed by two orders of magnitude and obeyed an approximate power law over 4 decades in time. Hellmann *et al.* [335] found such a fractal reaction kinetics with a time-dependent, power-law reaction rate also in two-dimensional, off-lattice simulations for the reaction $A + B \rightarrow \emptyset$ with subdiffusive motion of the reactants. Specifically, fractional Brownian motion was implemented by means of an overdamped Langevin equation with a power-law-correlated noise. Key findings were that *i*) independently of the reaction probability the diffusion-limited formation of new reactant pairs dominantly determines the reaction rate and *ii*) subdiffusive motion enhances the segregation of reactants. Extending this approach to describe a multi-step enzymatic reaction, the double-phosphorylation of mitogen-activated protein kinase (MAPK), an increased performance due to anomalous diffusion was found when dissociation rates of the intermediate enzyme-substrate complexes are high while the irreversible catalytic step is slow [336].

Froemberg and Sokolov [337] set up a continuum description in form of a reaction-subdiffusion equation for the reaction $A + B \rightarrow \emptyset$ with subdiffusive reactant motion governed by a CTRW. Supplying reactants of both types from both sides of the medium, stationary profiles of reactant concentrations and of reaction zones develop. These profiles exhibit accumulation and depletion zones close to the boundaries, and the reaction intensity was found to depend non-monotonically on the reactant concentration at the boundaries. A different approach was taken by Boon *et al.* [338] for the n^{th} -order annihilation reaction, $A + A + \dots + A \rightarrow \emptyset$, who derived a *nonlinear* reaction-diffusion equation assuming concentration-dependent diffusion and reaction coefficients and imposing a scaling form of the solution, i.e., demanding the concentration to satisfy $c(r, t) = t^{-\alpha/2} C(rt^{-\alpha/2})$. Thereby, subdiffusive motion of the reactant is incorporated, cf. Eqs. (3), (36), (71) and (75). Then, the resulting steady-state profiles exhibit a long-range, power-law decay and fit experimental data for the Wg morphogen gradient in *Drosophila* wing disc.

6. Conclusion

The advancements of biophysical experimental tools in the past two decades have revolutionised the investigation of intracellular transport of proteins, nucleic acids, and artificial tracers as well as the motion of membrane receptors and lipids. The new methods allowed for a detailed view of the plethora of dynamic processes *in vivo* directly at the cellular level. Numerous new phenomena and features of the transport have been discovered as more and more data of ever increasing quality have been collected. Living cells, by nature, consist of many differently sized and shaped constituents, each with their own physiological function, leading to densely packed, highly het-

erogeneous structures at the nanoscale—commonly referred to as *macromolecular crowding*. A widespread observation is that transport in living cells behaves rather different from the standard picture of Brownian motion, where the erratic trajectories are described by a probabilistic law as dictated by the central-limit theorem. Instead, the mean-square displacement, being the simplest quantitative measure of single-particle transport, displays complex and often also subdiffusive behaviour. Here, we have focused on anomalous transport, characterised by power-law increases on time windows covering several orders of magnitude. A unified physical picture of this spectacular anomaly remains one of the grand challenges of biophysics.

From a theoretical perspective, a fundamental issue is to identify mechanisms that lead to a violation of the central-limit theorem on macroscopic time scales. To this end, several theoretical models have been established that achieved this goal and yield a subdiffusive increase of the mean-square displacement. Here, we have summarised three of the most commonly used approaches based on different microscopic processes.

Fractional Brownian motion as a representative of spatially gaussian models is distinguished by a strictly self-similar increase of the mean-square displacement. Its most prominent feature is a power-law correlated, gaussian random noise. As a consequence, the stochastic process is stationary, but not Markovian. The transport propagator, i.e., the probability distribution of the displacements after a given lag time, displays a scaling property similar to simple Brownian motion.

Second, continuous-time random walk models describe a microscopic hopping process, which asymptotically generates subdiffusive motion in the case of waiting-time distributions with sufficiently broad power-law tails. It contains a fractional Fokker-Planck description as limiting case where the propagator exhibits scaling for all time and length scales. The scaling function depends on the subdiffusion exponent α and is markedly different from the gaussian case. In particular, the non-gaussian parameter does not vanish even for long times and approaches a characteristic value depending only on α . By the very construction, the process is non-stationary if the mean-waiting time is literally infinite, which implies ageing phenomena and weak ergodicity breaking.

The third class consists of Lorentz models, focusing on obstructed motion in strongly heterogeneous landscapes. Crowding agents lead to ramified structures delimiting the space accessible to the tracer, and anomalous transport emerges generically from the meandering motion of the tracer in such labyrinth-like structures. Subdiffusive motion occurs on larger and larger time windows as a localisation transition is approached, until long-range transport would eventually cease. In the vicinity of the transition, scaling behaviour develops and can be rationalised in terms of a dynamic critical phenomenon. The properties upon approaching anomalous transport are controlled by three independent, universal exponents

governing the mean-square displacement, the crossover time scale, and the fractal spatial structure. The averaged dynamics is stationary, exhibits heterogeneous diffusion, and marked non-gaussian spatial transport.

All three models are indistinguishable on the level of the mean-square displacement being subdiffusive. However, the predictions differ drastically if transport is considered on different length scales, for example by analysing spatio-temporal information as encoded in the propagator. Then, the shape of the scaling functions serves, in principle, as a fingerprint to discriminate the various theories. Since the full scaling function is often more difficult to measure than derived characteristics, we have exemplified the properties of the non-gaussian parameter as a potential clue in the quest for the microscopic origin of anomalous transport.

For this endeavour, researchers have matured the experimental techniques that are suited to uncover the transport properties of biophysical samples at mesoscopic scales. Single-particle tracking, fluorescence correlation spectroscopy, fluorescence recovery after photobleaching, among others, have widely been applied and yield complementary aspects of complex transport. Single-particle tracking provides access to the detailed particle trajectories and thereby to a complete statistical characterisation, in particular to the full propagator. Implementations based on video microscopy are typically restricted to limited temporal windows at a resolution of the order of 10 ms. Fluorescence correlation spectroscopy, on the other hand, probes shorter time scales and yields correlation functions over many decades in time. The shape of the correlation function serves as indicator for anomalous transport at the spatial scale of the illumination region. In recent developments, the beam waist has been made adjustable to probe the dynamics on a range of length scales, which then in principle allows for the discrimination of different propagators. Modern setups for fluorescence recovery after photobleaching are apt to detect slow transport on the time scale of several seconds and the length scale imposed by the bleaching spot; noteworthy, the method is sensitive to immobile particles as well. It monitors collective rather than single-particle transport, and anomalous transport becomes manifest in the recovery curve at long times. We see a need to evaluate the current theoretical approaches for measurable quantities of each of the above techniques. On the other hand, the interpretation of experimental data in the context of anomalous transport requires careful reconsideration of the underlying assumptions, e.g., spatially gaussian behaviour. Similarly, if the underlying process is (weakly) non-ergodic as is the case in CTRW or Lorentz models, time and ensemble averages generally do not coincide and caution is advised. Single molecule experiments are a promising tool to resolve these issues in the future.

Experiments inside the cyto- and nucleoplasm of various eukaryotic cells and bacteria have provided ample evidence for subdiffusive motion *in vivo* over several decades in time.

The overall investigated time scales covered the window from 100 μ s to 10 s, and the exponent α mostly ranged between 0.7 and 0.85 depending on the specific experiment, but also on the size of the tracer; an even smaller exponent of 0.53 was reported for 5-nm gold beads in many different cell types. These findings are supported by *in vitro* measurements on crowded model solutions, yielding systematically decreasing subdiffusion exponents α for increasingly crowded solution. The smallest values for α were obtained in dextran solution and reached down to 0.6 for dextran tracers and to 0.7 and 0.74 for globular proteins. A criticism on dextran as crowding agent is a possible interference of the tracer motion with the internal dynamics of polymeric dextran branches; for example, anomalous transport was regularly found to be less pronounced in solutions of globular proteins.

Computer simulations have corroborated the experimental findings at least qualitatively. Simplified model systems focusing on the excluded volume describe a rich phenomenology of anomalous transport including the gradual emergence of subdiffusive motion, spatially non-gaussian transport, heterogeneous diffusion with strongly suppressed diffusion constants, and a fraction of (on large scales) immobile particles. These phenomena have been related to a localisation transition, and simulation data have been rationalised in terms of dynamic scaling. Subdiffusive motion over many decades in time appears already for a small tracer in a slowly rearranging matrix of equally sized particles with apparent exponents less than 0.5; it persists for infinitely long times for randomly distributed obstacles at a critical value of the excluded volume, e.g., a universal value of the exponent $\alpha \approx 0.32$ was reported from simulations following the subdiffusive transport over 6 decades in time. More specific models for the cytoplasm of HeLa cells and *E. coli* use a distribution of particle sizes close to physiological conditions, yielding subdiffusive motion over several decades in time with exponents varying between 1 and 0.55 as function of the tracer size.

A number of experiments *in vivo* and *in vitro*, however, display simple, albeit slow diffusion with diffusion constants reduced by 1 to 3 orders of magnitude. For some experiments, data fitting required two normally diffusing components, ideally motivated by a physical picture like compound formation between tracer and crowding agent. For model solutions with adjustable degree of crowding, the reduction of diffusivity is explained to some extent by an increased macroscopic viscosity. On the other hand, it has been observed that the Stokes–Einstein relation is violated for proteins as probe and that the visco-elastic response on the nanoscale strongly deviates from the macroscopic rheological behaviour. Eventually, transport was found to be less anomalous in simulations if hydrodynamic interactions between the particles are taken into account; further, hydrodynamic interactions can already result in an up to 10-fold reduction of the *short-time* diffusion constant, in agreement with theory and recent scattering experi-

ments probing the nanosecond scale.

Summarising, anomalous transport has ubiquitously been observed in experiments *in vivo* and can be recreated in crowded model solutions and in computer simulations, but not in all instances. The picture is not thus simple and the appearance of anomalous transport in experiments is far from being understood. At least, one can say for model systems *in vitro* and *in silico* that transport is slowed down upon increasing the concentration of crowding agent or increasing the size of the tracer. An unsolved problem is the importance of the different contributions slowing down the motion, examples are excluded volume, polymer effects, compound formation, and hydrodynamic interactions.

The situation seems even more controversial for the motion of membrane proteins or phospholipids in cellular membranes. A central goal of such *in vivo* measurements is the elucidation of the membrane structure from the transport behaviour by indirect evidence; such biophysical conclusions are beyond the scope of this work, and we kindly refer the reader to Refs. 19, 157, and 228 for pertinent reviews. In cellular membranes, essentially all kinds of transport have been reported ranging from normal diffusion with reduced diffusion constants over subdiffusion to confined motion and immobile tracers. Former measurements of membrane proteins displayed a heterogeneous dynamics in the sense that different tracers of the same type showed qualitatively different motion. During the past decade, advances in the experimental techniques have given access to the transport behaviour over large time windows. For example, high-speed tracking of phospholipids with 25 μs resolution probed the mean-square displacement over five decades in time and have provided evidence for a double-crossover scenario including a regime of subdiffusive motion with exponent $\alpha \approx 0.53$. Similar time scales can be covered by fluorescence correlation spectroscopy, but crossovers between different regimes have not been observed so far; the experimental data were typically compatible with either gaussian subdiffusion or normal diffusion of a fast and a slow component. For several membrane proteins, subdiffusion was reported at the millisecond scale with exponents typically between 0.5 and 0.8, while other experiments found normal, but very slow diffusion at the scale of seconds. Spatial aspects of transport have been addressed by FCS experiments with variable illumination area, revealing anomalous transport in the form of length-scale-dependent diffusion coefficients below about 100 nm. Thus, the diffusion coefficient may depend both on the time and length scale under investigation, and both should cover a sufficiently large window for a comprehensive description of macromolecular transport in membranes.

As for cytoplasmic transport, the investigation of model systems is of paramount importance for a firm understanding of transport in membranes. *In vitro* studies of supported lipid bilayers or giant unilamellar vesicles agree that the lipid diffusion slows down in the presence of phase separation, which

may be induced by increasing, e.g., the cholesterol content of the lipid bilayer. It was found that gel-like regions effectively serve as a ramified, excluded area rendering the lipid motion anomalous. The experimental evidence has been corroborated by computer simulations for two-dimensional models of lipid mixtures close to fluid-gel coexistence, yielding subdiffusive motion for molecules exploring a heterogeneous structure. Pronounced subdiffusion over three decades in time was detected for the motion of proteins anchored to a lipid bilayer, with the exponent α developing from 1 to 0.68 as the bilayer was increasingly crowded by like proteins. Further, the transport of membrane proteins can become anomalous if a fraction of the membrane lipids is immobilised, e.g., by tethering to the substrate. This resembles obstacle models with a percolation threshold, where a ramified, heterogeneous landscape of excluded area appears generically. As in three dimensions, anomalous transport emerges in a finite temporal window upon approaching the percolation threshold, and subdiffusive motion with a universal exponent $\alpha \approx 0.66$ could be followed in simulations over 6 decades in time at the localisation transition.

As elaborated in this review, significant progress both on the experimental side as well as in theoretical modelling has been achieved in the puzzle of anomalous transport in crowded biological media. A lot of insight has been obtained, in particular, to establish the phenomenon itself and to identify implications of crowding on macromolecular transport. Yet, the knowledge acquired also raises a series of new questions challenging the frontier of biophysical research. Let us conclude this review by pointing at open problems and possible directions of future work.

So far, the interpretation of experimental data was mostly restricted to the mean-square displacement or the FCS correlation function assuming spatially gaussian transport. Only few studies discuss other statistical measures like distributions of displacements or of apparent exponents or even two-particle correlations. We have emphasised that the characterisation of anomalous transport depends on the time and length scales probed, highlighting the importance of collecting spatio-temporal information. To this end, testable theoretical predictions need to be elaborated and experimental methods to be perfected; a first step would be to focus on the non-gaussian behaviour, for which detailed predictions exist. Beyond that, multiple-time correlation functions contain information on the stochastic process underlying the transport, which would quantify the non-Markovian behaviour in particular. Here, a comparison between the different theoretical approaches remains to be done.

While basic models have been established, they need to be refined to capture specific experimental conditions. For example, fractional Brownian motion should be generalised to account for crossover phenomena to normal diffusion, both at microscopically short and macroscopically long time

scales. Similarly, several experimental groups have excluded the continuous-time random walk model as a candidate for anomalous transport since ageing scenarios intrinsic to the model have not been observed. This apparent deficiency can be avoided by considering large, but finite mean-waiting times, thus allowing for a graceful exit to normal diffusion at long times. The Lorentz models dealing with obstructions should be extended to account for correlated, differently sized obstacles and slowly rearranging disordered environments. Furthermore, the idealisation of a hard repulsive interaction should be relaxed, thus introducing barriers of finite rather than infinite height. Eventually, a significant ingredient to anomalous transport in the subcellular world are boundaries as imposed by (intra-)cellular membranes; the role of a finite space has been studied especially for the fractional Fokker–Planck equation.

Well-controlled experimental model systems offer a great potential to systematically investigate anomalous transport by examining adjustable crowding parameters over wide ranges. They provide the largely unexplored opportunity to address the same system by complementary techniques, allowing for a comprehensive description of the motion in crowded media. Further, they form a bridge from *in vivo* experiments to reductionist systems amenable to theory. Importantly, scaling behaviour could be tested here to discriminate between apparent subdiffusion as a mere phenomenological description of data in contrast to genuine anomalous transport over many orders of magnitude. As a central result of pushing experiments and theory further, it should become possible to predict the transport properties, at least qualitatively, from the outset of an experiment. On the other hand, it would be desirable to develop an experimental standard for subdiffusive transport, ideally covering sufficiently large windows in space and time, that is able to crosscalibrate the different experimental techniques [339]. Let us remark that the connection beyond the biophysical world, e.g., to transport phenomena in gels, porous media, and random heterogeneous materials, has so far remained largely elusive from an experimental point of view.

In the broader context of cell biology, single-particle transport is only one aspect of macromolecular transport and one anticipates also fascinating collective phenomena associated with crowded environments. Similarly, living cells comprise an abundance of active, non-equilibrium processes, and their connection to anomalous transport needs to be unravelled in the future. The grand challenge, of course, is to clarify the physiological implications of anomalous transport, most importantly: does it constitute merely a peculiarity or has it a biological benefit? For example, suggested scenarios on the acceleration of target search processes and bimolecular reactions need to be substantiated experimentally. More generally, important ingredients for systems biology like the kinetics of biochemical reactions, the dynamics of protein folding and unfolding, and intracellular signalling pathways may be strongly

affected by macromolecular crowding. The development of a unified picture of anomalous transport and its physiological consequences will entail an immense effort of interdisciplinary research during the next decade at least. Or let us phrase it with Ellis and Minton [226]: “Join the crowd!”

Acknowledgments

We thank C. Bräuchle, C. Fradin, E. Frey, I. Goychuk, P. Hänggi, D. Heinrich, J. Horbach, S. Jeney, J. Kärgler, D. C. Lamb, R. Metzler, J. O. Rädler, M. Saxton, F. Schreiber, I. M. Sokolov, A. Yethiraj, and M. Weiss for valuable scientific discussions and N. Destainville for correspondence. Financial support from the Deutsche Forschungsgemeinschaft (DFG) under contract no. FR 850/6-1 is gratefully acknowledged.

References

- [1] A. Einstein, *On the motion of small particles suspended in liquids at rest required by the molecular-kinetic theory of heat*, *Ann. Phys.* **17**, 549 (1905).
- [2] M. von Smoluchowski, *Zur kinetischen Theorie der Brownschen Molekularbewegung und der Suspensionen*, *Ann. Phys.* **326**, 756 (1906).
- [3] P. Langevin, *Sur la théorie de mouvement brownien*, *C. R. Hebd. Seances Acad. Sci.* **146**, 530 (1908).
- [4] D. S. Lemons and A. Gythiel, *Paul Langevin’s 1908 paper “on the theory of Brownian motion”* [*“Sur la théorie du mouvement brownien,” C. R. Acad. Sci. (Paris)* **146**, 530–533 (1908)], *Am. J. Phys.* **65**, 1079 (1997).
- [5] L. S. Ornstein, *On the Brownian motion*, *Proc. Royal Acad. Amsterdam* **21**, 96 (1917).
- [6] J. B. Perrin, *Mouvement brownien et réalité moléculaire*, *Ann. Chim. Phys.* **19**, 5 (1909).
- [7] P. Hänggi and F. Marchesoni, *Introduction: 100 years of Brownian motion*, *Chaos* **15**, 026101 (2005).
- [8] E. Frey and K. Kroy, *Brownian motion: a paradigm of soft matter and biological physics*, *Ann. Phys. (Leipzig)* **14**, 20 (2005).
- [9] I. M. Sokolov and J. Klafter, *From diffusion to anomalous diffusion: A century after Einstein’s Brownian motion*, *Chaos* **15**, 026103 (2005).
- [10] J. Renn, *Einstein’s invention of Brownian motion*, *Ann. Phys.* **14**, 23 (2005).
- [11] J.-P. Hansen and I. McDonald, *Theory of Simple Liquids*, 3rd ed. (Academic Press, Amsterdam, 2006).
- [12] J. P. Boon and S. Yip, *Molecular Hydrodynamics* (Dover Publications, Inc., New York, 1991) reprint.
- [13] S. W. Lovesey, *Theory of neutron scattering from condensed matter*, Vol. 1 (Clarendon Press, 1984).
- [14] B. J. Berne and R. Pecora, *Dynamic light scattering* (Wiley, New York, 1976) chapter 6.6.
- [15] R. Kubo, M. Toda, and N. Hashitsume, *Statistical Physics II: Nonequilibrium Statistical Mechanics* (Springer, 2008).

- [16] N. V. Kampen, *Stochastic Processes in Physics and Chemistry*, 3rd ed. (North Holland, 2007).
- [17] B. Øksendal, *Stochastic Differential Equations: An Introduction with Applications* (Springer, 2002).
- [18] M. J. Saxton, *A biological interpretation of transient anomalous subdiffusion. I. Qualitative model*, *Biophys. J.* **92**, 1178 (2007).
- [19] A. Kusumi, C. Nakada, K. Ritchie, K. Murase, K. Suzuki, H. Murakoshi, R. S. Kasai, J. Kondo, and T. Fujiwara, *Paradigm shift of the plasma membrane concept from the two-dimensional continuum fluid to the partitioned fluid: High-speed single-molecule tracking of membrane molecules*, *Annu. Rev. Biophys. Biomol. Struct.* **34**, 351 (2005).
- [20] D. Forster, *Hydrodynamic Fluctuations, Broken Symmetry, and Correlation Functions*, new ed. (Perseus Books, Jackson, TN, 2010).
- [21] W. Götzke, *Complex Dynamics of Glass-Forming Liquids: A Mode-Coupling Theory*, International Series of Monographs on Physics (Oxford University Press, Oxford, 2009).
- [22] T. Bauer, F. Höfling, T. Munk, E. Frey, and T. Franosch, *The localization transition of the two-dimensional Lorentz model*, *Eur. Phys. J. Special Topics* **189**, 103 (2010).
- [23] F. Höfling, K.-U. Bamberger, and T. Franosch, *Anomalous transport resolved in space and time by fluorescence correlation spectroscopy*, *Soft Matter* **7**, 1358 (2011).
- [24] B. B. Mandelbrot and J. W. V. Ness, *Fractional Brownian motions, fractional noises and applications*, *SIAM Review* **10**, 422 (1968).
- [25] S. C. Kou and X. S. Xie, *Generalized langevin equation with fractional gaussian noise: Subdiffusion within a single protein molecule*, *Phys. Rev. Lett.* **93**, 180603 (2004).
- [26] I. Goychuk, *Anomalous relaxation and dielectric response*, *Phys. Rev. E* **76**, 040102 (2007).
- [27] I. Goychuk, *Viscoelastic subdiffusion: From anomalous to normal*, *Phys. Rev. E* **80**, 046125 (2009).
- [28] A. H. Zemanian, *Distribution Theory and Transform Analysis* (Dover, 1987).
- [29] W. Deng and E. Barkai, *Ergodic properties of fractional brownian-langevin motion*, *Phys. Rev. E* **79**, 011112 (2009).
- [30] T. G. Mason and D. A. Weitz, *Optical measurements of frequency-dependent linear viscoelastic moduli of complex fluids*, *Phys. Rev. Lett.* **74**, 1250 (1995).
- [31] M. Grimm, S. Jeney, and T. Franosch, *Brownian motion in a Maxwell fluid*, *Soft Matter* **7**, 2076 (2011).
- [32] P. Sollich, F. Lequeux, P. Hébraud, and M. E. Cates, *Rheology of soft glassy materials*, *Phys. Rev. Lett.* **78**, 2020 (1997).
- [33] F. Amblard, A. C. Maggs, B. Yurke, A. N. Pargellis, and S. Leibler, *Subdiffusion and anomalous local viscoelasticity in actin networks*, *Phys. Rev. Lett.* **77**, 4470 (1996).
- [34] F. Gittes, B. Schnurr, P. D. Olmsted, F. C. MacKintosh, and C. F. Schmidt, *Microscopic viscoelasticity: Shear moduli of soft materials determined from thermal fluctuations*, *Phys. Rev. Lett.* **79**, 3286 (1997).
- [35] F. Gittes and F. C. MacKintosh, *Dynamic shear modulus of a semiflexible polymer network*, *Phys. Rev. E* **58**, R1241 (1998).
- [36] G. H. Koenderink, M. Atakhorrami, F. C. MacKintosh, and C. F. Schmidt, *High-frequency stress relaxation in semiflexible polymer solutions and networks*, *Phys. Rev. Lett.* **96**, 138307 (2006).
- [37] A. Taloni, A. Chechkin, and J. Klafter, *Generalized elastic model yields a fractional Langevin equation description*, *Phys. Rev. Lett.* **104**, 160602 (2010).
- [38] A. Taloni, A. Chechkin, and J. Klafter, *Correlations in a generalized elastic model: Fractional Langevin equation approach*, *Phys. Rev. E* **82**, 061104 (2010).
- [39] G. G. Stokes, *On the effect of the internal friction of fluids on the motion of a pendulum*, *Trans. Cambridge Philos. Soc.* **9**, 8 (1851).
- [40] T. Franosch, M. Grimm, M. Belushkin, F. M. Mor, G. Foffi, L. Forró, and S. Jeney, *Resonances arising from hydrodynamic memory in brownian motion*, *Nature* **478**, 85 (2011).
- [41] E. Hinch, *Application of the langevin equation to fluid suspensions*, *J. Fluid Mech.* **72**, 499 (1975).
- [42] B. J. Alder and T. E. Wainwright, *Velocity autocorrelations for hard spheres*, *Phys. Rev. Lett.* **18**, 988 (1967).
- [43] B. J. Alder and T. E. Wainwright, *Decay of the velocity autocorrelation function*, *Phys. Rev. A* **1**, 18 (1970).
- [44] B. Lukić, S. Jeney, C. Tischer, A. J. Kulik, L. Forró, and E.-L. Florin, *Direct observation of nondiffusive motion of a Brownian particle*, *Phys. Rev. Lett.* **95**, 160601 (2005).
- [45] M. Atakhorrami, G. H. Koenderink, C. F. Schmidt, and F. C. MacKintosh, *Short-time inertial response of viscoelastic fluids: Observation of vortex propagation*, *Phys. Rev. Lett.* **95**, 208302 (2005).
- [46] S. Jeney, B. Lukic, J. A. Kraus, T. Franosch, and L. Forro, *Anisotropic memory effects in confined colloidal diffusion*, *Phys. Rev. Lett.* **100**, 240604 (2008).
- [47] T. Franosch and S. Jeney, *Persistent correlation of constrained colloidal motion*, *Phys. Rev. E* **79**, 031402 (2009).
- [48] R. Metzler and J. Klafter, *The random walk's guide to anomalous diffusion: a fractional dynamics approach*, *Phys. Rep.* **339**, 1 (2000).
- [49] J.-P. Bouchaud and A. Georges, *Anomalous diffusion in disordered media: Statistical mechanisms, models and physical applications*, *Phys. Rep.* **195**, 127 (1990).
- [50] D. ben Avraham and S. Havlin, *Diffusion and Reactions in Fractals and Disordered Systems* (Cambridge University Press, Cambridge, 2000).
- [51] B. D. Hughes, *Random Walks and Random Environments*, Vol. 1: Random Walks (Oxford, Clarendon Press, 1995).
- [52] E. W. Montroll and G. H. Weiss, *Random walks on lattices. II*, *J. Math. Phys.* **6**, 167 (1965).
- [53] W. Feller, *An Introduction to Probability Theory and Its Applications*, 3rd ed., Vol. 2 (Wiley, 1968).
- [54] E. Scalas, R. Gorenflo, and F. Mainardi, *Uncoupled continuous-time random walks: Solution and limiting behavior of the master equation*, *Phys. Rev. E* **69**, 011107 (2004).
- [55] R. Gorenflo and F. Mainardi, *Continuous time random walk, Mittag-Leffler waiting time and fractional diffusion: mathematical aspects*, in *Anomalous Transport: Foundations and Applications*, edited by R. Klages, G. Radons, and I. M. Sokolov (Wiley-VCH, Weinheim, Germany, 2008) Chap. 4, pp. 93–127.
- [56] G. H. Weiss, *Aspects and Applications of Random Walks* (North-Holland, 1994).
- [57] G. H. Weiss and R. J. Rubin, *Random walks: Theory and se-*

- lected applications, in *Adv. Chem. Phys.*, Vol. 52, edited by I. Prigogine and S. A. Rice (Wiley, 1983) Chap. 5, pp. 363–505.
- [58] J. Klafter, A. Blumen, and M. F. Shlesinger, *Stochastic pathway to anomalous diffusion*, *Phys. Rev. A* **35**, 3081 (1987).
- [59] J. Karamata, *Neuer Beweis und Verallgemeinerung der Tauberschen Sätze, welche die Laplacesche und Stieltjessche Transformation betreffen*, *J. reine angew. Math.* **164**, 27 (1931).
- [60] R. Hilfer and L. Anton, *Fractional master equations and fractal time random walks*, *Phys. Rev. E* **51**, R848 (1995).
- [61] H. Weissman, G. H. Weiss, and S. Havlin, *Transport properties of the continuous-time random walk with a long-tailed waiting-time density*, *J. Stat. Phys.* **57**, 301 (1989).
- [62] E. Barkai and I. M. Sokolov, *Multi-point distribution function for the continuous time random walk*, *J. Stat. Mech.* **2007**, P08001 (2007).
- [63] M. Niemann and H. Kantz, *Joint probability distributions and multipoint correlations of the continuous-time random walk*, *Phys. Rev. E* **78**, 051104 (2008).
- [64] M. M. Meerschaert, D. A. Benson, H.-P. Scheffler, and B. Baeumer, *Stochastic solution of space-time fractional diffusion equations*, *Phys. Rev. E* **65**, 041103 (2002).
- [65] M. Magdziarz, A. Weron, K. Burnecki, and J. Klafter, *Fractional Brownian motion versus the continuous-time random walk: A simple test for subdiffusive dynamics*, *Phys. Rev. Lett.* **103**, 180602 (2009).
- [66] S. Condamin, V. Tejedor, R. Voituriez, O. Bénichou, and J. Klafter, *Probing microscopic origins of confined subdiffusion by first-passage observables*, *Proc. Natl. Acad. Sci. U. S. A.* **105**, 5675 (2008).
- [67] D. Ernst, M. Hellmann, J. Kohler, and M. Weiss, *Fractional Brownian motion in crowded fluids*, *Soft Matter* **8**, 4886 (2012).
- [68] G. Bel and E. Barkai, *Weak ergodicity breaking in the continuous-time random walk*, *Phys. Rev. Lett.* **94**, 240602 (2005).
- [69] S. Burov, R. Metzler, and E. Barkai, *Aging and nonergodicity beyond the Khinchin theorem*, *Proc. Nat. Acad. Sci. U. S. A.* **107**, 13228 (2010).
- [70] I. M. Sokolov, *Models of anomalous diffusion in crowded environments*, *Soft Matter* **8**, 9043 (2012).
- [71] J. P. Bouchaud, *Weak ergodicity breaking and aging in disordered systems*, *J. Phys. I France* **2**, 1705 (1992).
- [72] Y. He, S. Burov, R. Metzler, and E. Barkai, *Random time-scale invariant diffusion and transport coefficients*, *Phys. Rev. Lett.* **101**, 058101 (2008).
- [73] A. Lubelski, I. M. Sokolov, and J. Klafter, *Nonergodicity mimics inhomogeneity in single particle tracking*, *Phys. Rev. Lett.* **100**, 250602 (2008).
- [74] A. Rebenshtok and E. Barkai, *Weakly non-ergodic statistical physics*, *J. Stat. Phys.* **133**, 565 (2008).
- [75] I. M. Sokolov, *Statistics and the single molecule*, *Physics* **1**, 8 (2008).
- [76] I. M. Sokolov, E. Heinsalu, P. Hänggi, and I. Goychuk, *Universal fluctuations in subdiffusive transport*, *Europhys. Lett.* **86**, 30009 (2009).
- [77] H. A. Lorentz, *Le mouvement des électrons dans les métaux*, *Arch. Néerl. Sci. Exact Natur.* **10**, 336 (1905).
- [78] I. C. Kim and S. Torquato, *Diffusion of finite-sized Brownian particles in porous media*, *J. Chem. Phys.* **96**, 1498 (1992).
- [79] F. Höfling, T. Munk, E. Frey, and T. Franosch, *Critical dynamics of ballistic and Brownian particles in a heterogeneous environment*, *J. Chem. Phys.* **128**, 164517 (2008).
- [80] T. Franosch, F. Höfling, T. Bauer, and E. Frey, *Persistent memory for a random walker in a random array of obstacles*, *Chem. Phys.* **375**, 540 (2010).
- [81] C. P. James and G. T. Evans, *Diffusion in the two-dimensional nonoverlapping Lorentz gas*, *J. Chem. Phys.* **87**, 4056 (1987).
- [82] I.-A. Park and J. M. D. Macelroy, *Simulation of a hard-sphere fluid in bicontinuous random media*, *Mol. Simul.* **2**, 105 (1989).
- [83] B. J. Sung and A. Yethiraj, *Lateral diffusion and percolation in membranes*, *Phys. Rev. Lett.* **96**, 228103 (2006).
- [84] B. J. Sung and A. Yethiraj, *Lateral diffusion of proteins in the plasma membrane: Spatial tessellation and percolation theory*, *J. Phys. Chem. B* **112**, 143 (2008).
- [85] A. B. Adib, *Random-walk approach to the d-dimensional disordered Lorentz gas*, *Phys. Rev. E* **77**, 021118 (2008).
- [86] M. Spanner, *Transport in the correlated Lorentz model*, Master's thesis, Friedrich-Alexander-Universität Erlangen-Nürnberg (2010).
- [87] M. J. Saxton, *Anomalous diffusion due to obstacles: a Monte Carlo study*, *Biophys. J.* **66**, 394 (1994).
- [88] J. M. J. van Leeuwen and A. Weijland, *Non-analytic density behaviour of the diffusion coefficient of a Lorentz gas I*, *Physica (Amsterdam)* **36**, 457 (1967).
- [89] A. Weijland and J. M. J. van Leeuwen, *Non-analytic density behaviour of the diffusion coefficient of a Lorentz gas II*, *Physica (Amsterdam)* **38**, 35 (1968).
- [90] C. Bruin, *Logarithmic terms in the diffusion coefficient for the Lorentz gas*, *Phys. Rev. Lett.* **29**, 1670 (1972).
- [91] C. Bruin, *A computer experiment on diffusion in the Lorentz gas*, *Physica* **72**, 261 (1974).
- [92] W. Götze, E. Leutheusser, and S. Yip, *Dynamical theory of diffusion and localization in a random, static field*, *Phys. Rev. A* **23**, 2634 (1981).
- [93] W. Götze, E. Leutheusser, and S. Yip, *Correlation functions of the hard-sphere Lorentz model*, *Phys. Rev. A* **24**, 1008 (1981).
- [94] W. Götze, E. Leutheusser, and S. Yip, *Diffusion and localization in the two-dimensional Lorentz model*, *Phys. Rev. A* **25**, 533 (1982).
- [95] A. Masters and T. Keyes, *Diffusion, percolation, and trapping in the Lorentz gas via variational kinetic theory*, *Phys. Rev. A* **26**, 2129 (1982).
- [96] V. Krakoviack, *Liquid-glass transition of a fluid confined in a disordered porous matrix: A mode-coupling theory*, *Phys. Rev. Lett.* **94**, 065703 (2005).
- [97] V. Krakoviack, *Mode-coupling theory for the slow collective dynamics of fluids adsorbed in disordered porous media*, *Phys. Rev. E* **75**, 031503 (2007).
- [98] V. Krakoviack, *Tagged-particle dynamics in a fluid adsorbed in a disordered porous solid: Interplay between the diffusion-localization and liquid-glass transitions*, *Phys. Rev. E* **79**, 061501 (2009).
- [99] Th. Voigtmann, *Multiple glasses in asymmetric binary hard*

- spheres, *Europhys. Lett.* **96**, 36006 (2011).
- [100] J. Kurzidim, D. Coslovich, and G. Kahl, *Single-particle and collective slow dynamics of colloids in porous confinement*, *Phys. Rev. Lett.* **103**, 138303 (2009).
- [101] J. Kurzidim, D. Coslovich, and G. Kahl, *Dynamic arrest of colloids in porous environments: disentangling crowding and confinement*, *J. Phys.: Condens. Matter* **23**, 234122 (2011).
- [102] K. Kim, K. Miyazaki, and S. Saito, *Slow dynamics in random media: Crossover from glass to localization transition*, *Europhys. Lett.* **88**, 36002 (2009).
- [103] K. Kim, K. Miyazaki, and S. Saito, *Molecular dynamics studies of slow dynamics in random media: Type A-B and reentrant transitions*, *Eur. Phys. J. Special Topics* **189**, 135 (2010).
- [104] S. K. Schnyder, F. Höfling, T. Franosch, and Th. Voigtmann, *Long-wavelength anomalies in the asymptotic behavior of mode-coupling theory*, *J. Phys.: Condens. Matter* **23**, 234121 (2011).
- [105] A. R. Kerstein, *Equivalence of the void percolation problem for overlapping spheres and a network problem*, *J. Phys. A* **16**, 3071 (1983).
- [106] W. T. Elam, A. R. Kerstein, and J. J. Rehr, *Critical properties of the void percolation problem for spheres*, *Phys. Rev. Lett.* **52**, 1516 (1984).
- [107] D. Stauffer and A. Aharony, *Introduction to Percolation Theory*, 2nd ed. (Taylor & Francis, London, 1994).
- [108] J. Cardy, *Scaling and Renormalization in Statistical Physics* (Cambridge University Press, 1996).
- [109] P. Grassberger, *Conductivity exponent and backbone dimension in 2-d percolation*, *Physica A* **262**, 251 (1999).
- [110] J. Asikainen, A. Aharony, B. Mandelbrot, E. Rausch, and J.-P. Hovi, *Fractal geometry of critical Potts clusters*, *Eur. Phys. J. B* **34**, 479 (2003).
- [111] R. M. Ziff, *Correction-to-scaling exponent for two-dimensional percolation*, *Phys. Rev. E* **83**, 020107(R) (2011).
- [112] N. Jan and D. Stauffer, *Random site percolation in three dimensions*, *Int. J. Mod. Phys. C* **9**, 341 (1998).
- [113] C. D. Lorenz and R. M. Ziff, *Precise determination of the bond percolation thresholds and finite-size scaling corrections for the sc, fcc, and bcc lattices*, *Phys. Rev. E* **57**, 230 (1998).
- [114] J. Machta and S. M. Moore, *Diffusion and long-time tails in the overlapping Lorentz gas*, *Phys. Rev. A* **32**, 3164 (1985).
- [115] F. Höfling, T. Franosch, and E. Frey, *Localization transition of the three-dimensional Lorentz model and continuum percolation*, *Phys. Rev. Lett.* **96**, 165901 (2006).
- [116] A. Kammerer, F. Höfling, and T. Franosch, *Cluster-resolved dynamic scaling theory and universal corrections for transport on percolating systems*, *Europhys. Lett.* **84**, 66002 (2008).
- [117] B. I. Halperin, S. Feng, and P. N. Sen, *Differences between lattice and continuum percolation transport exponents*, *Phys. Rev. Lett.* **54**, 2391 (1985).
- [118] F. Höfling and T. Franosch, *Crossover in the slow decay of dynamic correlations in the Lorentz model*, *Phys. Rev. Lett.* **98**, 140601 (2007).
- [119] J. P. Straley, *Non-universal threshold behaviour of random resistor networks with anomalous distributions of conductances*, *J. Phys. C* **15**, 2343 (1982).
- [120] J. Machta, R. A. Guyer, and S. M. Moore, *Conductivity in percolation networks with broad distributions of resistances*, *Phys. Rev. B* **33**, 4818 (1986).
- [121] O. Stenull and H. Janssen, *Conductivity of continuum percolating systems*, *Phys. Rev. E* **64**, 56105 (2001).
- [122] M. D. Rintoul, *Precise determination of the void percolation threshold for two distributions of overlapping spheres*, *Phys. Rev. E* **62**, 68 (2000).
- [123] S. C. van der Marck, *Network approach to void percolation in a pack of unequal spheres*, *Phys. Rev. Lett.* **77**, 1785 (1996).
- [124] J. A. Quintanilla and R. M. Ziff, *Asymmetry in the percolation thresholds of fully penetrable disks with two different radii*, *Phys. Rev. E* **76**, 051115 (2007).
- [125] J. Quintanilla, S. Torquato, and R. M. Ziff, *Efficient measurement of the percolation threshold for fully penetrable discs*, *J. Phys. A* **33**, L399 (2000).
- [126] T. Franosch, M. Spanner, T. Bauer, G. E. Schröder-Turk, and F. Höfling, *Space-resolved dynamics of a tracer in a disordered solid*, *J. Non-Cryst. Solids* **357**, 472 (2011).
- [127] M. Spanner, F. Höfling, G. E. Schröder-Turk, K. Mecke, and T. Franosch, *Anomalous transport of a tracer on percolating clusters*, *J. Phys.: Condens. Matter* **23**, 234120 (2011).
- [128] M. J. Saxton, *Two-dimensional continuum percolation threshold for diffusing particles of nonzero radius*, *Biophys. J.* **99**, 1490 (2010).
- [129] P. G. de Gennes, *La percolation: un concept unificateur*, *La Recherche* **7**, 919 (1976).
- [130] C. Mitescu and J. Roussenoq, *Ant in a labyrinth - diffusion in a percolation system*, *C. R. Acad. Sci. Paris* **283**, A 999 (1976).
- [131] J. P. Straley, *The ant in the labyrinth: diffusion in random networks near the percolation threshold*, *J. Phys. C: Solid State Phys.* **13**, 2991 (1980).
- [132] Y. Gefen, A. Aharony, and S. Alexander, *Anomalous diffusion on percolating clusters*, *Phys. Rev. Lett.* **50**, 77 (1983).
- [133] R. B. Pandey, D. Stauffer, A. Margolina, and J. G. Zabolitzky, *Diffusion on random systems above, below, and at their percolation threshold in two and three dimensions*, *J. Stat. Phys.* **34**, 427 (1984).
- [134] P. C. Hohenberg and B. I. Halperin, *Theory of dynamic critical phenomena*, *Rev. Mod. Phys.* **49**, 435 (1977).
- [135] J. Kertész and J. Metzger, *Properties of the density relaxation function in classical diffusion models with percolation transition*, *J. Phys. A* **16**, L735 (1983).
- [136] M. Spanner, S. K. Schnyder, F. Höfling, T. Voigtmann, and T. Franosch, *Dynamic arrest in model porous media—intermediate scattering functions*, *Soft Matter* **9**, 1604 (2013).
- [137] F. Höfling, *Dynamics of Rod-Like Macromolecules in Heterogeneous Materials*, Ph.D. thesis, Ludwig-Maximilians-Universität München (2006), ISBN 978-3-86582-426-4.
- [138] M. H. Ernst and A. Weijland, *Long time behaviour of the velocity auto-correlation function in a Lorentz gas*, *Phys. Lett. A* **34**, 39 (1971).
- [139] H. van Beijeren, *Transport properties of stochastic Lorentz models*, *Rev. Mod. Phys.* **54**, 195 (1982).
- [140] B. J. Ackerson and L. Fleishman, *Correlations for dilute hard core suspensions*, *J. Chem. Phys.* **76**, 2675 (1982).
- [141] D. Frenkel, F. van Luijn, and P.-M. Binder, *Evidence for universal asymptotic decay of velocity fluctuations in Lorentz gases*, *Europhys. Lett.* **20**, 7 (1992).

- [142] S. R. Williams, G. Bryant, I. K. Snook, and W. van Meegen, *Velocity autocorrelation functions of hard-sphere fluids: Long-time tails upon undercooling*, *Phys. Rev. Lett.* **96**, 087801 (2006).
- [143] S. R. Williams, P. McGlynn, G. Bryant, I. K. Snook, and W. van Meegen, *Dynamical signatures of freezing: Stable fluids, metastable fluids, and crystals*, *Phys. Rev. E* **74**, 031204 (2006).
- [144] F. Höfling and P. H. Colberg, *Power-law decay of velocity autocorrelations in the supercooled Kob–Andersen mixture*, (2012), in preparation.
- [145] M. Fuchs and K. Kroy, *Statistical mechanics derivation of hydrodynamic boundary conditions: the diffusion equation*, *J. Phys.: Condens. Matter* **14**, 9223 (2002).
- [146] J. Machta, *Anomalous long time tails due to trapping*, *J. Stat. Phys.* **42**, 941 (1986).
- [147] Q.-H. Wei, C. Bechinger, and P. Leiderer, *Single-file diffusion of colloids in one-dimensional channels*, *Science New Series*, **287**, 625 (2000).
- [148] C. Lutz, M. Kollmann, and C. Bechinger, *Single-file diffusion of colloids in one-dimensional channels*, *Phys. Rev. Lett.* **93**, 026001 (2004).
- [149] L. Lizana, T. Ambjörnsson, A. Taloni, E. Barkai, and M. A. Lomholt, *Foundation of fractional Langevin equation: Harmonization of a many-body problem*, *Phys. Rev. E* **81**, 051118 (2010).
- [150] M. Doi and S. F. Edwards, *The Theory of Polymer Dynamics* (Oxford University Press, New York, 1986).
- [151] T. C. B. McLeish, *Tube theory of entangled polymer dynamics*, *Adv. Phys.* **51**, 1379 (2002).
- [152] R. Kimmich and N. Fatkullin, *Polymer chain dynamics and NMR*, in *NMR – 3D Analysis – Photopolymerization*, *Adv. Polym. Sci.*, Vol. 170 (Springer Berlin Heidelberg, 2004) pp. 1–113.
- [153] D. Richter, M. Monkenbusch, A. Arbe, and J. Colmenero, *Neutron spin echo in polymer systems*, in *Neutron Spin Echo in Polymer Systems*, *Adv. Polym. Sci.*, Vol. 174 (Springer Berlin Heidelberg, 2005) pp. 1–221.
- [154] A. Ochab-Marcinek and R. Holyst, *Scale-dependent diffusion of spheres in solutions of flexible and rigid polymers: mean square displacement and autocorrelation function for FCS and DLS measurements*, *Soft Matter* **7**, 7366 (2011).
- [155] A. Ochab-Marcinek, S. A. Wieczorek, N. Ziębacz, and R. Holyst, *The effect of depletion layer on diffusion of nanoparticles in solutions of flexible and polydisperse polymers*, *Soft Matter* **8**, 11173 (2012).
- [156] W. J. Greenleaf, M. T. Woodside, and S. M. Block, *High-resolution, single-molecule measurements of biomolecular motion*, *Annu. Rev. Biophys. Biomol. Struct.* **36**, 171 (2007).
- [157] M. J. Saxton and K. Jacobson, *Single-particle tracking: Applications to membrane dynamics*, *Annu. Rev. Biophys. Biomol. Struct.* **26**, 373 (1997).
- [158] J. A. Dix and A. Verkman, *Crowding effects on diffusion in solutions and cells*, *Ann. Rev. Biophys.* **37**, 247 (2008).
- [159] M. B. Smith, E. Karatekin, A. Gohlke, H. Mizuno, N. Watanabe, and D. Vavylonis, *Interactive, computer-assisted tracking of speckle trajectories in fluorescence microscopy: Application to actin polymerization and membrane fusion*, *Biophys. J.* **101**, 1794 (2011).
- [160] D. Wirtz, *Particle-tracking microrheology of living cells: Principles and applications*, *Annu. Rev. Biophys.* **38**, 301 (2009).
- [161] A. Yao, M. Tassieri, M. Padgett, and J. Cooper, *Microrheology with optical tweezers*, *Lab Chip* **9**, 2568 (2009).
- [162] T. M. Squires and T. G. Mason, *Fluid mechanics of microrheology*, *Annu. Rev. Fluid Mech.* **42**, 413 (2010).
- [163] V. Levi, Q. Ruan, and E. Gratton, *3-D particle tracking in a two-photon microscope: Application to the study of molecular dynamics in cells*, *Biophys. J.* **88**, 2919 (2005).
- [164] Y. Katayama, O. Burkacky, M. Meyer, C. Bräuchle, E. Gratton, and D. C. Lamb, *Real-time nanomicroscopy via three-dimensional single-particle tracking*, *ChemPhysChem* **10**, 2458 (2009).
- [165] M. Speidel, A. Jonáš, and E.-L. Florin, *Three-dimensional tracking of fluorescent nanoparticles with subnanometer precision by use of off-focus imaging*, *Opt. Lett.* **28**, 69 (2003).
- [166] R. Huang, I. Chavez, K. M. Taute, B. Lukic, S. Jeney, M. G. Raizen, and E.-L. Florin, *Direct observation of the full transition from ballistic to diffusive brownian motion in a liquid*, *Nat Phys* **7**, 576 (2011).
- [167] W. Feller, *An Introduction to Probability Theory and Its Applications*, 3rd ed., Vol. 1 (Wiley, 1968).
- [168] P. H. Colberg and F. Höfling, *Highly accelerated simulations of glassy dynamics using GPUs: Caveats on limited floating-point precision*, *Comp. Phys. Comm.* **182**, 1120 (2011).
- [169] G. J. Schütz, H. Schindler, and T. Schmidt, *Single-molecule microscopy on model membranes reveals anomalous diffusion*, *Biophys. J.* **73**, 1073 (1997).
- [170] M. A. Deverall, E. Gindl, E. K. Sinner, H. Besir, J. Ruehe, M. J. Saxton, and C. A. Naumann, *Membrane lateral mobility obstructed by polymer-tethered lipids studied at the single molecule level*, *Biophys. J.* **88**, 1875 (2005).
- [171] A. V. Weigel, B. Simon, M. M. Tamkun, and D. Krapf, *Ergodic and nonergodic processes coexist in the plasma membrane as observed by single-molecule tracking*, *Proc. Natl. Acad. Sci. U. S. A.* **108**, 6438 (2011).
- [172] B. Wang, S. M. Anthony, S. C. Bae, and S. Granick, *Anomalous yet Brownian*, *Proc. Nat. Acad. Sci. U. S. A.* **106**, 15160 (2009).
- [173] F. Feil, S. Naumov, J. Michaelis, R. Valiullin, D. Enke, J. Kärger, and C. Bräuchle, *Single-particle and ensemble diffusivities—test of ergodicity*, *Angew. Chem. Int. Ed.* **51**, 1152 (2012).
- [174] J. Kirstein, B. Platschek, C. Jung, R. Brown, T. Bein, and C. Bräuchle, *Exploration of nanostructured channel systems with single-molecule probes*, *Nat. Mater.* **6**, 303 (2007).
- [175] R. Rigler and E. S. Elson, eds., *Fluorescence Correlation Spectroscopy* (Springer, Berlin, 2001).
- [176] O. Krichevsky and G. Bonnet, *Fluorescence correlation spectroscopy: the technique and its applications*, *Rep. Prog. Phys.* **65**, 251 (2002).
- [177] S. T. Hess, S. Huang, A. A. Heikal, and W. W. Webb, *Biological and chemical applications of fluorescence correlation spectroscopy: A review*, *Biochemistry* **41**, 697 (2002).
- [178] E. P. Petrov and P. Schwille, *State of the art and novel trends in fluorescence correlation spectroscopy*, in *Standardization and Quality Assurance in Fluorescence Measurements II*, Springer

- Series on Fluorescence, Vol. 6 (Springer, 2008) Chap. 21, pp. 145–197.
- [179] R. Macháň and M. Hof, *Lipid diffusion in planar membranes investigated by fluorescence correlation spectroscopy*, *Biochim. Biophys. Acta – Biomembr.* **1798**, 1377 (2010).
- [180] A. Masuda, K. Ushida, and T. Okamoto, *New fluorescence correlation spectroscopy enabling direct observation of spatiotemporal dependence of diffusion constants as an evidence of anomalous transport in extracellular matrices*, *Biophys. J.* **88**, 3584 (2005).
- [181] L. Wawrezynieck, H. Rigneault, D. Marguet, and P. F. Lenne, *Fluorescence correlation spectroscopy diffusion laws to probe the submicron cell membrane organization*, *Biophys. J.* **89**, 4029 (2005).
- [182] J. Humpolíčková, E. Gielen, A. Benda, V. Fagulova, J. Vercammen, M. van de Ven, M. Hof, M. Ameloot, and Y. Engelborghs, *Probing diffusion laws within cellular membranes by z-scan fluorescence correlation spectroscopy*, *Biophys. J.* **91**, L23 (2006).
- [183] E. Gielen, M. van de Ven, A. Margineanu, P. Dedecker, M. V. der Auweraer, Y. Engelborghs, J. Hofkens, and M. Ameloot, *On the use of z-scan fluorescence correlation experiments on giant unilamellar vesicles*, *Chem. Phys. Lett.* **469**, 110 (2009).
- [184] H. Rigneault, J. Capoulade, J. Dintinger, J. Wenger, N. Bonod, E. Popov, T. W. Ebbesen, and P.-F. Lenne, *Enhancement of single-molecule fluorescence detection in subwavelength apertures*, *Phys. Rev. Lett.* **95**, 117401 (2005).
- [185] J. Wenger, F. Conchonaud, J. Dintinger, L. Wawrezynieck, T. W. Ebbesen, H. Rigneault, D. Marguet, and P.-F. Lenne, *Diffusion analysis within single nanometric apertures reveals the ultrafine cell membrane organization*, *Biophys. J.* **92**, 913 (2007).
- [186] D. Vobornik, D. S. Banks, Z. Lu, C. Fradin, R. Taylor, and L. J. Johnston, *Fluorescence correlation spectroscopy with sub-diffraction-limited resolution using near-field optical probes*, *Appl. Phys. Lett.* **93**, 163904 (2008).
- [187] L. Kastrop, H. Blom, C. Eggeling, and S. W. Hell, *Fluorescence fluctuation spectroscopy in subdiffraction focal volumes*, *Phys. Rev. Lett.* **94**, 178104 (2005).
- [188] S. W. Hell, *Far-field optical nanoscopy*, *Science* **316**, 1153 (2007).
- [189] C. Eggeling, C. Ringemann, R. Medda, G. Schwarzmann, K. Sandhoff, S. Polyakova, V. N. Belov, B. Hein, C. von Middendorff, A. Schönle, and S. W. Hell, *Direct observation of the nanoscale dynamics of membrane lipids in a living cell*, *Nature* **457**, 1159 (2009).
- [190] R. Shusterman, S. Alon, T. Gavrinov, and O. Krichevsky, *Monomer dynamics in double- and single-stranded DNA polymers*, *Phys. Rev. Lett.* **92**, 048303 (2004).
- [191] M. R. Horton, F. Höfling, J. O. Rädler, and T. Franosch, *Development of anomalous diffusion among crowding proteins*, *Soft Matter* **6**, 2648 (2010).
- [192] R. Shusterman, T. Gavrinov, and O. Krichevsky, *Internal dynamics of superhelical DNA*, *Phys. Rev. Lett.* **100**, 098102 (2008).
- [193] R. G. Winkler, S. Keller, and J. O. Rädler, *Intramolecular dynamics of linear macromolecules by fluorescence correlation spectroscopy*, *Phys. Rev. E* **73**, 041919 (2006).
- [194] N. Destainville, *Theory of fluorescence correlation spectroscopy at variable observation area for two-dimensional diffusion on a meshgrid*, *Soft Matter* **4**, 1288 (2008).
- [195] M. J. Saxton, *Fluorescence correlation spectroscopy*, *Biophys. J.* **89**, 3678 (2005).
- [196] T. Franosch and W. Götze, *Relaxation rate distributions for supercooled liquids*, *J. Phys. Chem. B* **103**, 4011 (1999).
- [197] C. L. Epstein and J. Schotland, *The bad truth about Laplace's transform*, *SIAM Review* **50**, 504 (2008).
- [198] P. Sengupta, K. Garai, J. Balaji, N. Periasamy, and S. Maiti, *Measuring size distribution in highly heterogeneous systems with fluorescence correlation spectroscopy*, *Biophys. J.* **84**, 1977 (2003).
- [199] D. S. Banks and C. Fradin, *Anomalous diffusion of proteins due to molecular crowding*, *Biophys. J.* **89**, 2960 (2005).
- [200] H. Sanabria, Y. Kubota, and M. N. Waxham, *Multiple diffusion mechanisms due to nanostructuring in crowded environments*, *Biophys. J.* **92**, 313 (2007).
- [201] N. Malchus and M. Weiss, *Elucidating anomalous protein diffusion in living cells with fluorescence correlation spectroscopy—facts and pitfalls*, *J. Fluoresc.* **20**, 19 (2010).
- [202] C. Fradin, A. Abu-Arish, R. Granek, and M. Elbaum, *Fluorescence correlation spectroscopy close to a fluctuating membrane*, *Biophys. J.* **84**, 2005 (2003).
- [203] J. Enderlein, I. Gregor, D. Patra, and J. Fitter, *Art and artefacts of fluorescence correlation spectroscopy*, *Curr. Pharm. Biotechnol.* **5**, 155 (2004).
- [204] K. Bacia, S. A. Kim, and P. Schwille, *Fluorescence cross-correlation spectroscopy in living cells*, *Nat. Methods* **3**, 83 (2006).
- [205] R. Peters, J. Peters, K. H. Tews, and W. Bähr, *A microfluorimetric study of translational diffusion in erythrocyte membranes*, *Biochim. Biophys. Acta – Biomembr.* **367**, 282 (1974).
- [206] D. Axelrod, D. Koppel, J. Schlessinger, E. Elson, and W. Webb, *Mobility measurement by analysis of fluorescence photobleaching recovery kinetics*, *Biophys. J.* **16**, 1055 (1976).
- [207] D. Axelrod, P. Ravdin, D. E. Koppel, J. Schlessinger, W. W. Webb, E. L. Elson, and T. R. Podleski, *Lateral motion of fluorescently labeled acetylcholine receptors in membranes of developing muscle fibers*, *Proc. Natl. Acad. Sci. U. S. A.* **73**, 4594 (1976).
- [208] M. Edidin, Y. Zagyansky, and T. Lardner, *Measurement of membrane protein lateral diffusion in single cells*, *Science* **191**, 466 (1976).
- [209] K. Jacobson, Z. Derzko, E.-S. Wu, Y. Hou, and G. Poste, *Measurement of the lateral mobility of cell surface components in single living cells by fluorescence recovery after photobleaching*, *J. Supramol. Struct.* **5**, 565 (1976).
- [210] E. L. Elson, *Fluorescence correlation spectroscopy and photobleaching recovery*, *Annu. Rev. Phys. Chem.* **36**, 379 (1985).
- [211] T. Meyvis, S. De Smedt, P. Van Oostveldt, and J. Demeester, *Fluorescence recovery after photobleaching: A versatile tool for mobility and interaction measurements in pharmaceutical research*, *Pharm. Res.* **16**, 1153 (1999).
- [212] J. Lippincott-Schwartz, E. Snapp, and A. Kenworthy, *Studying protein dynamics in living cells*, *Nat. Rev. Mol. Cell Biol.* **2**,

- 444 (2001).
- [213] E. A. J. Reits and J. J. Neeffjes, *From fixed to FRAP: measuring protein mobility and activity in living cells*, *Nat. Cell Biol.* **3**, E145 (2001).
- [214] A. S. Verkman, *Diffusion in cells measured by fluorescence recovery after photobleaching*, in *Biophotonics, Part A*, Methods in Enzymology, Vol. 360, edited by G. Marriott and I. Parker (Academic Press, 2003) Chap. 28, pp. 635 – 648.
- [215] D. M. Soumpasis, *Theoretical analysis of fluorescence photobleaching recovery experiments*, *Biophys. J.* **41**, 95 (1983).
- [216] B. A. Smith and H. M. McConnell, *Determination of molecular motion in membranes using periodic pattern photobleaching*, *Proc. Nat. Acad. Sci. U. S. A.* **75**, 2759 (1978).
- [217] J. Davoust, P. F. Devaux, and L. Leger, *Fringe pattern photobleaching, a new method for the measurement of transport coefficients of biological macromolecules*, *EMBO J.* **1**, 1233–1238 (1982).
- [218] T. E. Starr and N. L. Thompson, *Fluorescence pattern photobleaching recovery for samples with multi-component diffusion*, *Biophys. Chem.* **97**, 29 (2002).
- [219] Y. Gambin, R. Lopez-Esparza, M. Reffay, E. Sierrecki, N. S. Gov, M. Genest, R. S. Hodges, and W. Urbach, *Lateral mobility of proteins in liquid membranes revisited*, *Proc. Natl. Acad. Sci. U. S. A.* **103**, 2098 (2006).
- [220] P. Wedekind, U. Kubitscheck, O. Heinrich, and R. Peters, *Line-scanning microphotolysis for diffraction-limited measurements of lateral diffusion*, *Biophys. J.* **71**, 1621 (1996).
- [221] N. Smisdom, K. Braeckmans, H. Deschout, M. van de Ven, J.-M. Rigo, S. C. D. Smedt, and M. Ameloot, *Fluorescence recovery after photobleaching on the confocal laser-scanning microscope: generalized model without restriction on the size of the photobleached disk*, *J. Biomed. Optics* **16**, 046021 (2011).
- [222] L. Salomé, J.-L. Cazeils, A. Lopez, and J.-F. Tocanne, *Characterization of membrane domains by FRAP experiments at variable observation areas*, *Eur. Biophys. J.* **27**, 391 (1998).
- [223] T. Feder, I. Brust-Mascher, J. Slattery, B. Baird, and W. Webb, *Constrained diffusion or immobile fraction on cell surfaces: a new interpretation*, *Biophys. J.* **70**, 2767 (1996).
- [224] R. J. Ellis, *Macromolecular crowding: obvious but underappreciated*, *Trends Biochem. Sci.* **26**, 597 (2001).
- [225] R. J. Ellis, *Macromolecular crowding: an important but neglected aspect of the intracellular environment*, *Curr. Opin. Struct. Biol.* **11**, 114 (2001).
- [226] R. J. Ellis and A. P. Minton, *Cell biology: Join the crowd*, *Nature* **425**, 27 (2003).
- [227] D. Hall and A. P. Minton, *Macromolecular crowding: qualitative and semiquantitative successes, quantitative challenges*, *Biochim. Biophys. Acta – Proteins Proteom.* **1649**, 127 (2003).
- [228] S. Chiantia, J. Ries, and P. Schwille, *Fluorescence correlation spectroscopy in membrane structure elucidation*, *Biochim. Biophys. Acta – Biomembr.* **1788**, 225 (2009).
- [229] A. H. Elcock, *Models of macromolecular crowding effects and the need for quantitative comparisons with experiment*, *Curr. Opin. Struct. Biol.* **20**, 196 (2010).
- [230] I. M. Tolić-Nørrelykke, E.-L. Munteanu, G. Thon, L. Oddershede, and K. Berg-Sørensen, *Anomalous diffusion in living yeast cells*, *Phys. Rev. Lett.* **93**, 078102 (2004).
- [231] C. Selhuber-Unkel, P. Yde, K. Berg-Sørensen, and L. B. Oddershede, *Variety in intracellular diffusion during the cell cycle*, *Phys. Biol.* **6**, 025015 (2009).
- [232] V. Tejedor, O. Benichou, R. Voituriez, R. Jungmann, F. Simmel, C. Selhuber-Unkel, L. B. Oddershede, and R. Metzler, *Quantitative analysis of single particle trajectories: Mean maximal excursion method*, *Biophys. J.* **98**, 1364 (2010).
- [233] J.-H. Jeon, V. Tejedor, S. Burov, E. Barkai, C. Selhuber-Unkel, K. Berg-Sørensen, L. Oddershede, and R. Metzler, *In vivo anomalous diffusion and weak ergodicity breaking of lipid granules*, *Phys. Rev. Lett.* **106**, 048103 (2011).
- [234] I. Golding and E. C. Cox, *Physical nature of bacterial cytoplasm*, *Phys. Rev. Lett.* **96**, 098102 (2006).
- [235] S. C. Weber, A. J. Spakowitz, and J. A. Theriot, *Bacterial chromosomal loci move subdiffusively through a viscoelastic cytoplasm*, *Phys. Rev. Lett.* **104**, 238102 (2010).
- [236] I. Bronstein, Y. Israel, E. Kepten, S. Mai, Y. Shav-Tal, E. Barkai, and Y. Garini, *Transient anomalous diffusion of telomeres in the nucleus of mammalian cells*, *Phys. Rev. Lett.* **103**, 018102 (2009).
- [237] A. Caspi, R. Granek, and M. Elbaum, *Diffusion and directed motion in cellular transport*, *Phys. Rev. E* **66**, 011916 (2002).
- [238] P. Schwille, U. Haupts, S. Maiti, and W. W. Webb, *Molecular dynamics in living cells observed by fluorescence correlation spectroscopy with one- and two-photon excitation*, *Biophys. J.* **77**, 2251 (1999).
- [239] M. Wachsmuth, W. Waldeck, and J. Langowski, *Anomalous diffusion of fluorescent probes inside living cell nuclei investigated by spatially-resolved fluorescence correlation spectroscopy*, *J. Mol. Biol.* **298**, 677 (2000).
- [240] M. Weiss, M. Elsner, F. Kartberg, and T. Nilsson, *Anomalous subdiffusion is a measure for cytoplasmic crowding in living cells*, *Biophys. J.* **87**, 3518 (2004).
- [241] G. Guigas, C. Kalla, and M. Weiss, *Probing the nanoscale viscoelasticity of intracellular fluids in living cells*, *Biophys. J.* **93**, 316 (2007).
- [242] G. Guigas, C. Kalla, and M. Weiss, *The degree of macromolecular crowding in the cytoplasm and nucleoplasm of mammalian cells is conserved*, *FEBS Lett.* **581**, 5094 (2007).
- [243] E. Dauty and A. S. Verkman, *Actin cytoskeleton as the principal determinant of size-dependent DNA mobility in cytoplasm*, *J. Biol. Chem.* **280**, 7823 (2005).
- [244] H. Engelke, D. Heinrich, and J. O. Rädler, *Probing GFP-actin diffusion in living cells using fluorescence correlation spectroscopy*, *Phys. Biol.* **7**, 046014 (2010).
- [245] K. Luby-Phelps, D. Taylor, and F. Lanni, *Probing the structure of cytoplasm*, *J. Cell Biol.* **102**, 2015 (1986).
- [246] K. Luby-Phelps, P. E. Castle, D. L. Taylor, and F. Lanni, *Hindered diffusion of inert tracer particles in the cytoplasm of mouse 3T3 cells*, *Proc. Natl. Acad. Sci. U. S. A.* **84**, 4910 (1987).
- [247] O. Seksek, J. Biwersi, and A. Verkman, *Translational diffusion of macromolecule-sized solutes in cytoplasm and nucleus*, *J. Cell Biol.* **138**, 131 (1997).
- [248] M. Arrio-Dupont, G. Foucault, M. Vacher, P. F. Devaux, and S. Cribier, *Translational diffusion of globular proteins in the cytoplasm of cultured muscle cells*, *Biophys. J.* **78**, 901 (2000).
- [249] M. Arrio-Dupont, S. Cribier, G. Foucault, P. Devaux, and

- A. d'Albis, *Diffusion of fluorescently labeled macromolecules in cultured muscle cells*, *Biophys. J.* **70**, 2327 (1996).
- [250] M. B. Elowitz, M. G. Surette, P.-E. Wolf, J. B. Stock, and S. Leibler, *Protein mobility in the cytoplasm of Escherichia coli*, *J. Bacteriol.* **181**, 197 (1999).
- [251] D. Arcizet, B. Meier, E. Sackmann, J. O. Rädler, and D. Heinrich, *Temporal analysis of active and passive transport in living cells*, *Phys. Rev. Lett.* **101**, 248103 (2008).
- [252] K. Keren, P. T. Yam, A. Kinkhabwala, A. Mogilner, and J. A. Theriot, *Intracellular fluid flow in rapidly moving cells*, *Nat. Cell. Biol.* **11**, 1219 (2009).
- [253] M. Otten, A. Nandi, D. Arcizet, M. Gorelashvili, B. Lindner, and D. Heinrich, *Local motion analysis reveals impact of the dynamic cytoskeleton on intracellular subdiffusion*, *Biophys. J.* **102**, 758 (2012).
- [254] K. de Bruin, N. Ruthardt, K. von Gersdorff, R. Bausinger, E. Wagner, M. Ogris, and C. Bräuchle, *Cellular dynamics of EGF receptor-targeted synthetic viruses*, *Mol. Ther.* **15**, 1297 (2007).
- [255] N. Ruthardt and C. Bräuchle, *Visualizing uptake and intracellular trafficking of gene carriers by single-particle tracking*, in *Nucleic Acid Transfection*, Topics in Current Chemistry, Vol. 296, edited by W. Bielke and C. Erbacher (Springer, Berlin, 2010) pp. 283–304.
- [256] A. W. Lifland, C. Zurla, J. Yu, and P. J. Santangelo, *Dynamics of native β -actin mRNA transport in the cytoplasm*, *Traffic* **12**, 1000 (2011).
- [257] S. C. Weber, J. A. Theriot, and A. J. Spakowitz, *Subdiffusive motion of a polymer composed of subdiffusive monomers*, *Phys. Rev. E* **82**, 011913 (2010).
- [258] I. Y. Wong, M. L. Gardel, D. R. Reichman, E. R. Weeks, M. T. Valentine, A. R. Bausch, and D. A. Weitz, *Anomalous diffusion probes microstructure dynamics of entangled F-actin networks*, *Phys. Rev. Lett.* **92**, 178101 (2004).
- [259] A. Palmer, T. G. Mason, J. Xu, S. C. Kuo, and D. Wirtz, *Diffracting wave spectroscopy microrheology of actin filament networks*, *Biophys. J.* **76**, 1063 (1999).
- [260] K. Kang, J. Gapiński, M. P. Lettinga, J. Buitenhuis, G. Meier, M. Ratajczyk, J. K. G. Dhont, and A. Patkowski, *Diffusion of spheres in crowded suspensions of rods*, *J. Chem. Phys.* **122**, 044905 (2005).
- [261] J. Szymański and M. Weiss, *Elucidating the origin of anomalous diffusion in crowded fluids*, *Phys. Rev. Lett.* **103**, 038102 (2009).
- [262] E. Dauty and A. S. Verkman, *Molecular crowding reduces to a similar extent the diffusion of small solutes and macromolecules: measurement by fluorescence correlation spectroscopy*, *J. Mol. Recognit.* **17**, 441 (2004).
- [263] J. Szymański, A. Patkowski, J. Gapiński, A. Wilk, and R. Holyst, *Movement of proteins in an environment crowded by surfactant micelles: Anomalous versus normal diffusion*, *J. Phys. Chem. B* **110**, 7367 (2006).
- [264] J. Szymański, A. Patkowski, A. Wilk, P. Garstecki, and R. Holyst, *Diffusion and viscosity in a crowded environment: from nano- to macroscale*, *J. Phys. Chem. B* **110**, 25593 (2006).
- [265] S. P. Zustiak, R. Nossal, and D. L. Sackett, *Hindered diffusion in polymeric solutions studied by fluorescence correlation spectroscopy*, *Biophys. J.* **101**, 255 (2011).
- [266] F. Roosen-Runge, M. Hennig, F. Zhang, R. M. J. Jacobs, M. Sztucki, H. Schober, T. Seydel, and F. Schreiber, *Protein self-diffusion in crowded solutions*, *Proc. Natl. Acad. Sci. U. S. A.* **108**, 11815 (2011).
- [267] F. Roosen-Runge, M. Hennig, T. Seydel, F. Zhang, M. W. Skoda, S. Zorn, R. M. Jacobs, M. Maccarini, P. Fouquet, and F. Schreiber, *Protein diffusion in crowded electrolyte solutions*, *Biochim. Biophys. Acta – Proteins Proteom.* **1804**, 68 (2010).
- [268] Y. Wang, C. Li, and G. J. Pielak, *Effects of proteins on protein diffusion*, *J. Am. Chem. Soc.* **132**, 9392 (2010).
- [269] M. Tokuyama and I. Oppenheim, *Dynamics of hard-sphere suspensions*, *Phys. Rev. E* **50**, R16 (1994).
- [270] A. J. Banchio and G. Nägele, *Short-time transport properties in dense suspensions: From neutral to charge-stabilized colloidal spheres*, *J. Chem. Phys.* **128**, 104903 (2008).
- [271] T. Ando and J. Skolnick, *Crowding and hydrodynamic interactions likely dominate in vivo macromolecular motion*, *Proc. Nat. Acad. Sci. U. S. A.* **107**, 18457 (2010).
- [272] A. J. Moreno and J. Colmenero, *Relaxation scenarios in a mixture of large and small spheres: Dependence on the size disparity*, *J. Chem. Phys.* **125**, 164507 (2006).
- [273] Th. Voigtmann and J. Horbach, *Double transition scenario for anomalous diffusion in glass-forming mixtures*, *Phys. Rev. Lett.* **103**, 205901 (2009).
- [274] S. R. McGuffee and A. H. Elcock, *Diffusion, crowding & protein stability in a dynamic molecular model of the bacterial cytoplasm*, *PLoS Comput Biol.* **6**, e1000694 (2010).
- [275] C. Echeverria and R. Kapral, *Macromolecular dynamics in crowded environments*, *J. Chem. Phys.* **132**, 104902 (2010).
- [276] F. Tabatabaei, O. Lenz, and C. Holm, *Simulational study of anomalous tracer diffusion in hydrogels*, *Colloid Polym. Sci.* **289**, 523 (2011).
- [277] J. Horbach, Th. Voigtmann, F. Höfling, and T. Franosch, *Localization phenomena in models of ion-conducting glass formers*, *Eur. Phys. J. Special Topics* **189**, 141 (2010).
- [278] A. Baumgärtner and M. Muthukumar, *A trapped polymer chain in random porous media*, *J. Chem. Phys.* **87**, 3082 (1987).
- [279] G. W. Slater and S. Yan Wu, *Reptation, entropic trapping, percolation, and rouse dynamics of polymers in “random” environments*, *Phys. Rev. Lett.* **75**, 164 (1995).
- [280] G. I. Nixon and G. W. Slater, *Relaxation length of a polymer chain in a quenched disordered medium*, *Phys. Rev. E* **60**, 3170 (1999).
- [281] A. Kusumi, Y. Sako, and M. Yamamoto, *Confined lateral diffusion of membrane receptors as studied by single particle tracking (nanovid microscopy). effects of calcium-induced differentiation in cultured epithelial cells*, *Biophys. J.* **65**, 2021 (1993).
- [282] E. D. Sheets, G. M. Lee, R. Simson, and K. Jacobson, *Transient confinement of a glycosylphosphatidylinositol-anchored protein in the plasma membrane*, *Biochemistry* **36**, 12449 (1997).
- [283] M. Tomishige, Y. Sako, and A. Kusumi, *Regulation mechanism of the lateral diffusion of band 3 in erythrocyte membranes by the membrane skeleton*, *J. Cell Biol.* **142**, 989 (1998).

- [284] T. Fujiwara, K. Ritchie, H. Murakoshi, K. Jacobson, and A. Kusumi, *Phospholipids undergo hop diffusion in compartmentalized cell membrane*, *J. Cell Biol.* **157**, 1071 (2002).
- [285] K. Murase, T. Fujiwara, Y. Umemura, K. Suzuki, R. Iino, H. Yamashita, M. Saito, H. Murakoshi, K. Ritchie, and A. Kusumi, *Ultrafine membrane compartments for molecular diffusion as revealed by single molecule techniques*, *Biophys. J.* **86**, 4075 (2004).
- [286] P. R. Smith, I. E. Morrison, K. M. Wilson, N. Fernández, and R. J. Cherry, *Anomalous diffusion of major histocompatibility complex class I molecules on HeLa cells determined by single particle tracking*, *Biophys. J.* **76**, 3331 (1999).
- [287] M. Vrljic, S. Y. Nishimura, S. Brasselet, W. Moerner, and H. M. McConnell, *Translational diffusion of individual class II MHC membrane proteins in cells*, *Biophys. J.* **83**, 2681 (2002).
- [288] J. Deich, E. M. Judd, H. H. McAdams, and W. E. Moerner, *Visualization of the movement of single histidine kinase molecules in live *Caulobacter* cells*, *Proc. Natl. Acad. Sci. U. S. A.* **101**, 15921 (2004).
- [289] J. M. Crane and A. Verkman, *Long-range nonanomalous diffusion of quantum dot-labeled aquaporin-1 water channels in the cell plasma membrane*, *Biophys. J.* **94**, 702 (2008).
- [290] P. Schwille, J. Korfach, and W. W. Webb, *Fluorescence correlation spectroscopy with single-molecule sensitivity on cell and model membranes*, *Cytometry* **36**, 176 (1999).
- [291] E. Gielen, J. Vercaemmen, J. Sýkora, J. Humpolíčková, M. van de Ven, A. Benda, N. Hellings, M. Hof, Y. Engelborghs, P. Steels, and M. Ameloot, *Diffusion of sphingomyelin and myelin oligodendrocyte glycoprotein in the membrane of OLN-93 oligodendroglial cells studied by fluorescence correlation spectroscopy*, *C. R. Biologies* **328**, 1057 (2005).
- [292] M. Weiss, H. Hashimoto, and T. Nilsson, *Anomalous protein diffusion in living cells as seen by fluorescence correlation spectroscopy*, *Biophys. J.* **84**, 4043 (2003).
- [293] J. Ries and P. Schwille, *Studying slow membrane dynamics with continuous wave scanning fluorescence correlation spectroscopy*, *Biophys. J.* **91**, 1915 (2006).
- [294] P.-F. Lenne, L. Wawrezynieck, F. Conchonaud, O. Wurtz, A. Boned, X.-J. Guo, H. Rigneault, H.-T. He, and D. Marguet, *Dynamic molecular confinement in the plasma membrane by microdomains and the cytoskeleton meshwork*, *EMBO J.* **25**, 3245 (2006).
- [295] A. Ishihara, Y. Hou, and K. Jacobson, *The Thy-1 antigen exhibits rapid lateral diffusion in the plasma membrane of rodent lymphoid cells and fibroblasts*, *Proc. Natl. Acad. Sci. U. S. A.* **84**, 1290 (1987).
- [296] A. K. Kenworthy, B. J. Nichols, C. L. Remmert, G. M. Hendrix, M. Kumar, J. Zimmerberg, and J. Lippincott-Schwartz, *Dynamics of putative raft-associated proteins at the cell surface*, *J. Cell Biol.* **165**, 735 (2004).
- [297] M. Frick, K. Schmidt, and B. J. Nichols, *Modulation of lateral diffusion in the plasma membrane by protein density*, *Curr. Biol.* **17**, 462 (2007).
- [298] A.-M. Baker, A. Saulière, G. Gaibelet, B. Lagane, S. Mazères, M. Fourage, F. Bachelierie, L. Salomé, A. Lopez, and F. Dumas, *CD4 interacts constitutively with multiple CCR5 at the plasma membrane of living cells*, *J. Biol. Chem.* **282**, 35163 (2007).
- [299] S. J. Singer and G. L. Nicolson, *The fluid mosaic model of the structure of cell membranes*, *Science* **175**, 720 (1972).
- [300] G. Vereb, J. Szöllösi, J. Matkó, P. Nagy, T. Farkas, L. Vigh, L. Mátyus, T. A. Waldmann, and S. Damjanovich, *Dynamic, yet structured: The cell membrane three decades after the singer-nicolson model*, *Proc. Nat. Acad. Sci. U. S. A.* **100**, 8053 (2003).
- [301] D. M. Engelman, *Membranes are more mosaic than fluid*, *Nature* **438**, 578 (2005).
- [302] A. Kusumi, H. Ike, C. Nakada, K. Murase, and T. Fujiwara, *Single-molecule tracking of membrane molecules: plasma membrane compartmentalization and dynamic assembly of raft-philic signaling molecules*, *Semin. Immunol.* **17**, 3 (2005), Spatial Organization in Immune Cell Signaling.
- [303] A. V. Weigel, S. Ragi, M. L. Reid, E. K. P. Chong, M. M. Tamkun, and D. Krapf, *Obstructed diffusion propagator analysis for single-particle tracking*, *Phys. Rev. E* **85**, 041924 (2012).
- [304] Q. Ruan, M. A. Cheng, M. Levi, E. Gratton, and W. W. Mantulin, *Spatial-temporal studies of membrane dynamics: Scanning fluorescence correlation spectroscopy (SFCS)*, *Biophys. J.* **87**, 1260 (2004).
- [305] A. Benda, M. Benes, V. Mareček, A. Lhotsky, W. T. Hermens, and M. Hof, *How to determine diffusion coefficients in planar phospholipid systems by confocal fluorescence correlation spectroscopy*, *Langmuir* **19**, 4120 (2003).
- [306] A. E. Hac, H. M. Seeger, M. Fidorra, and T. Heimburg, *Diffusion in two-component lipid membranes—a fluorescence correlation spectroscopy and Monte Carlo simulation study*, *Biophys. J.* **88**, 317 (2005).
- [307] C. Favard, J. Wenger, P.-F. Lenne, and H. Rigneault, *FCS diffusion laws in two-phase lipid membranes: Determination of domain mean size by experiments and Monte Carlo simulations*, *Biophys. J.* **100**, 1242 (2011).
- [308] P. F. F. Almeida, W. L. C. Vaz, and T. E. Thompson, *Lateral diffusion in the liquid phases of dimyristoylphosphatidylcholine/cholesterol lipid bilayers: a free volume analysis*, *Biochemistry* **31**, 6739 (1992).
- [309] S. Ramadurai, A. Holt, V. Krasnikov, G. van den Bogaart, J. A. Killian, and B. Poolman, *Lateral diffusion of membrane proteins*, *J. Am. Chem. Soc.* **131**, 12650 (2009).
- [310] S. F. Fenz, R. Merkel, and K. Sengupta, *Diffusion and intermembrane distance: Case study of avidin and E-cadherin mediated adhesion*, *Langmuir* **25**, 1074 (2009).
- [311] M. R. Horton, C. Reich, A. P. Gast, J. O. Rädler, and B. Nickel, *Structure and dynamics of crystalline protein layers bound to supported lipid bilayers*, *Langmuir* **23**, 6263 (2007).
- [312] M. J. Saxton, *Lateral diffusion in an archipelago. The effect of mobile obstacles*, *Biophys. J.* **52**, 989 (1987).
- [313] M. J. Skaug, R. Faller, and M. L. Longo, *Correlating anomalous diffusion with lipid bilayer membrane structure using single molecule tracking and atomic force microscopy*, *J. Chem. Phys.* **134**, 215101 (2011).
- [314] D. V. Nicolau, Jr., J. F. Hancock, and K. Burrage, *Sources of anomalous diffusion on cell membranes: A Monte Carlo study*, *Biophys. J.* **92**, 1975 (2007).
- [315] A. M. S. Niehaus, D. G. Vlachos, J. S. Edwards, P. Plechac, and R. Tribe, *Microscopic simulation of membrane molecule*

- diffusion on corrallated membrane surfaces, *Biophys. J.* **94**, 1551 (2008).
- [316] I. P. Sugár and R. L. Biltonen, *Lateral diffusion of molecules in two-component lipid bilayer: A Monte Carlo simulation study*, *J. Phys. Chem. B* **109**, 7373 (2005).
- [317] J. Ehrig, E. P. Petrov, and P. Schwille, *Near-critical fluctuations and cytoskeleton-assisted phase separation lead to subdiffusion in cell membranes*, *Biophys. J.* **100**, 80 (2011).
- [318] J. Ehrig, E. P. Petrov, and P. Schwille, *Phase separation and near-critical fluctuations in two-component lipid membranes: Monte Carlo simulations on experimentally relevant scales*, *New J. Phys.* **13**, 045019 (2011).
- [319] M. Roark and S. E. Feller, *Molecular dynamics simulation study of correlated motions in phospholipid bilayer membranes*, *J. Phys. Chem. B* **113**, 13229 (2009).
- [320] J. Machta, M. H. Ernst, H. van Beijeren, and J. R. Dorfman, *Long time tails in stationary random media II: Applications*, *J. Stat. Phys.* **35**, 413 (1984).
- [321] I. P. Sugár, T. E. Thompson, and R. L. Biltonen, *Monte carlo simulation of two-component bilayers: DMPC/DSPC mixtures*, *Biophys. J.* **76**, 2099 (1999).
- [322] K. Kawasaki, *Diffusion constants near the critical point for time-dependent ising models. III. self-diffusion constant*, *Phys. Rev.* **150**, 285 (1966).
- [323] S. K. Das, M. E. Fisher, J. V. Sengers, J. Horbach, and K. Binder, *Critical dynamics in a binary fluid: Simulations and finite-size scaling*, *Phys. Rev. Lett.* **97**, 025702 (2006).
- [324] S. K. Das, J. Horbach, K. Binder, M. E. Fisher, and J. V. Sengers, *Static and dynamic critical behavior of a symmetrical binary fluid: A computer simulation*, *J. Chem. Phys.* **125**, 024506 (2006).
- [325] P. S. Coppock and J. T. Kindt, *Atomistic simulations of mixed-lipid bilayers in gel and fluid phases*, *Langmuir* **25**, 352 (2009).
- [326] H.-X. Zhou, G. Rivas, and A. P. Minton, *Macromolecular crowding and confinement: Biochemical, biophysical, and potential physiological consequences*, *Ann. Rev. Biophys.* **37**, 375 (2008).
- [327] B. O'Shaughnessy and D. Vavylonis, *Kinetic regimes and cross-over times in many-particle reacting systems*, *EPL (Europhys. Lett.)* **45**, 653 (1999).
- [328] E. Melo and J. Martins, *Kinetics of bimolecular reactions in model bilayers and biological membranes. A critical review*, *Biophys. Chem.* **123**, 77 (2006).
- [329] M. J. Saxton, *Chemically limited reactions on a percolation cluster*, *J. Chem. Phys.* **116**, 203 (2002).
- [330] M. J. Saxton, *A biological interpretation of transient anomalous subdiffusion. II. Reaction kinetics*, *Biophys. J.* **94**, 760 (2008).
- [331] J. D. Schmit, E. Kamber, and J. Kondev, *Lattice model of diffusion-limited bimolecular chemical reactions in confined environments*, *Phys. Rev. Lett.* **102**, 218302 (2009).
- [332] N. Dorsaz, C. De Michele, F. Piazza, P. De Los Rios, and G. Foffi, *Diffusion-limited reactions in crowded environments*, *Phys. Rev. Lett.* **105**, 120601 (2010).
- [333] J. S. Kim and A. Yethiraj, *Crowding effects on association reactions at membranes*, *Biophys. J.* **98**, 951 (2010).
- [334] D. Ridgway, G. Broderick, A. Lopez-Campistrous, M. Ru'a'ini, P. Winter, M. Hamilton, P. Boulanger, A. Kovalenko, and M. J. Ellison, *Coarse-grained molecular simulation of diffusion and reaction kinetics in a crowded virtual cytoplasm*, *Biophys. J.* **94**, 3748 (2008).
- [335] M. Hellmann, D. W. Heermann, and M. Weiss, *Anomalous reaction kinetics and domain formation on crowded membranes*, *Europhys. Lett.* **94**, 18002 (2011).
- [336] M. Hellmann, D. W. Heermann, and M. Weiss, *Enhancing phosphorylation cascades by anomalous diffusion*, *Europhys. Lett.* **97**, 58004 (2012).
- [337] D. Froemberg and I. M. Sokolov, *Stationary fronts in an $A + B \rightarrow \emptyset$ reaction under subdiffusion*, *Phys. Rev. Lett.* **100**, 108304 (2008).
- [338] J. P. Boon, J. F. Lutsko, and C. Lutsko, *Microscopic approach to nonlinear reaction-diffusion: The case of morphogen gradient formation*, *Phys. Rev. E* **85**, 021126 (2012).
- [339] M. J. Saxton, *Wanted: A positive control for anomalous subdiffusion*, *Biophys. J.* **103**, 2411 (2012).